

# MASSIVE BLACK HOLE DYNAMICS IN UNEQUAL MASS GALAXY MERGERS

by

Sandor Van Wassenhove

A dissertation submitted in partial fulfillment  
of the requirements for the degree of  
Doctor of Philosophy  
(Astronomy and Astrophysics)  
in the University of Michigan  
2013

Doctoral Committee:

Associate Professor Jon M. Miller, Chair

Professor August Evrard

Professor Lee W. Hartmann

Professor Douglas O. Richstone

Directeur de Recherche Marta Volonteri, Institut Astrophysique de Paris

# CONTENTS

|                              |      |
|------------------------------|------|
| LIST OF FIGURES . . . . .    | v    |
| LIST OF TABLES . . . . .     | vii  |
| LIST OF APPENDICES . . . . . | viii |
| ABSTRACT . . . . .           | ix   |

## CHAPTER

|   |           |
|---|-----------|
| <b>1 Introduction . . . . .</b>                                   | <b>1</b>  |
| 1.1 History of Black Hole Detections . . . . .                    | 2         |
| 1.2 Black Hole Formation Mechanism . . . . .                      | 4         |
| 1.3 Black Hole Growth: Accretion and Black Hole Mergers . . . . . | 5         |
| 1.4 Galaxy Mergers . . . . .                                      | 7         |
| 1.5 Outline . . . . .   | 10        |
| <b>2 Numerical Methods . . . . .</b>                              | <b>13</b> |
| 2.1 GASOLINE . . . . .  | 14        |
| 2.2 Resolution . . . . .  | 16        |
| 2.3 Galaxy Models . . . . .                                       | 17        |
| 2.3.1 Spiral Galaxies . . . . .                                   | 17        |
| 2.3.2 Gas Poor Galaxies . . . . .                                 | 18        |
| 2.4 Orbital Parameters . . . . .                                  | 18        |
| 2.5 Conclusions . . . . .   | 19        |
| <b>3 Nuclear Coups in Unequal Mass Galaxy Mergers . . . . .</b>   | <b>21</b> |
| 3.1 Introduction . . . . .  | 21        |
| 3.2 Dynamical Evolution . . . . .                                 | 23        |
| 3.2.1 Tidal Torques . . . . .                                     | 23        |

|          |   |           |
|----------|---|-----------|
| 3.2.2    | Ram Pressure . . . . .  | 24        |
| 3.2.3    | Star Formation Driven by Angular Momentum Loss . . .                                | 26        |
| 3.2.4    | Tidal Stripping . . . . .   | 31        |
| 3.2.5    | Tidal Heating . . . . .   | 32        |
| 3.2.6    | Dynamical Friction . . . . .  | 34        |
| 3.3      | Results . . . . .   | 36        |
| 3.3.1    | Impact of Mass Ratio . . . . .  | 36        |
| 3.3.2    | Impact of Orbital Parameters . . . . .  | 43        |
| 3.4      | Discussion . . . . .  | 48        |
| 3.4.1    | BH Pairing and Binary Evolution . . . . .   | 54        |
| 3.4.2    | Influence of Resolution . . . . .   | 55        |
| 3.5      | Conclusions . . . . .   | 55        |
| <b>4</b> | <b>Merger Driven Black Hole Accretion and Dual Active Galactic Nuclei</b> . . . . . | <b>57</b> |
| 4.1      | Introduction . . . . .  | 57        |
| 4.2      | Merger Driven Active Galactic Nuclei . . . . .                                      | 59        |
| 4.2.1    | Accretion Driven by Gaseous Inflows . . . . .                                       | 62        |
| 4.2.2    | Evolution of the Black Hole Mass Ratio . . . . .                                    | 69        |
| 4.2.3    | Correlation between Star Formation and BH Accretion .                               | 71        |
| 4.3      | Dual Active Galactic Nuclei . . . . .   | 73        |
| 4.3.1    | Impact of Observational Constraints . . . . .                                       | 75        |
| 4.3.2    | Gas Poor Primary Galaxies . . . . .   | 79        |
| 4.4      | Discussion . . . . .  | 80        |
| 4.5      | Conclusions . . . . .   | 83        |
| <b>5</b> | <b>Massive Black Holes in Milky Way Satellites</b> . . . . .                        | <b>85</b> |
| 5.1      | Introduction . . . . .  | 85        |
| 5.2      | Massive black hole formation and dynamical evolution . . . . .                      | 86        |
| 5.2.1    | Massive black hole formation models . . . . .                                       | 87        |
| 5.2.2    | Massive black hole and galaxy evolution . . . . .                                   | 90        |
| 5.2.3    | Dynamical evolution of satellites and massive black holes                           | 93        |

|       |   |     |
|-------|---|-----|
| 5.3   | Black hole occupation fraction and mass scaling . . . . . | 97  |
| 5.4   | Observational Prospects . . . . .                         | 100 |
| 5.4.1 | Dynamical measurements . . . . .                          | 100 |
| 5.4.2 | Gravitational waves . . . . .                             | 103 |
| 5.5   | Conclusions . . . . .                                     | 105 |
| 6     | <b>Conclusions</b> . . . . .                              | 108 |
| 6.1   | Summary . . . . .   | 108 |
| 6.2   | Improvements in Sub-Grid Models . . . . .                 | 110 |
| 6.3   | Future Work . . . . .                                     | 112 |
|       | APPENDIX . . . . .  | 114 |
|       | BIBLIOGRAPHY . . . . .                                    | 130 |

# LIST OF FIGURES

## Figure

|      |   |    |
|------|---|----|
| 1.1  | M- $\sigma$ Relation . . . . .  | 3  |
| 3.1  | 1:4 Prograde Coplanar Diagnostics . . . . .                                 | 27 |
| 3.2  | 1:4 Prograde Coplanar Second Pericenter Gas Density . . . . .               | 29 |
| 3.3  | 1:4 Prograde Coplanar Central Densities . . . . .                           | 30 |
| 3.4  | 1:2 Prograde Coplanar Diagnostics . . . . .                                 | 37 |
| 3.5  | 1:6 Prograde Coplanar Diagnostics . . . . .                                 | 38 |
| 3.6  | 1:10 Prograde Coplanar Diagnostics . . . . .                                | 39 |
| 3.7  | Cumulative Star Formation Mass . . . . .                                    | 41 |
| 3.8  | 1:2 Inclined Diagnostics . . . . .  | 45 |
| 3.9  | 1:4 Inclined Diagnostics . . . . .  | 46 |
| 3.10 | 1:2 Retrograde (Primary) Diagnostics . . . . .                              | 49 |
| 3.11 | 1:2 Retrograde (Secondary) Diagnostics . . . . .                            | 50 |
| 3.12 | 1:2 Retrograde (Secondary) Coplanar Second Pericenter Gas Density . . . . . | 51 |
| 4.1  | 1:2 Prograde Coplanar BH Accretion . . . . .                                | 63 |
| 4.2  | 1:6 Prograde Coplanar BH Accretion . . . . .                                | 64 |
| 4.3  | 1:2 Inclined BH Accretion . . . . .   | 66 |
| 4.4  | 1:2 Retrograde (Primary) BH Accretion . . . . .                             | 67 |
| 4.5  | 1:2 Retrograde (Secondary) BH Accretion . . . . .                           | 68 |
| 4.6  | BH Mass Ratio Evolution . . . . .   | 70 |
| 4.7  | 1:2 Prograde Coplanar Dual AGN with Observational Constraints . . . . .     | 76 |
| 4.8  | 1:2 Retrograde (Primary) Dual AGN with Observational Constraints . . . . .  | 77 |
| 4.9  | 1:6 Prograde Coplanar Dual AGN with Observational Constraints . . . . .     | 78 |

|     |  |     |
|-----|--|-----|
| 5.1 | Satellite Population Diagnostics . . . . .                               | 94  |
| 5.2 | BH Occupation Fraction and Mass Distribution . . . . .                   | 99  |
| 5.3 | Dwarf Galaxy BH Observational Prospects . . . . .                        | 101 |
| A.1 | Star Formation Comparison to a Schmidt Law . . . . .                     | 119 |
| B.1 | 1:2 Inclined Dual AGN with Observational Constraints . . . . .           | 125 |
| B.2 | 1:2 Retrograde (Secondary) Dual AGN with Observational Constraints .     | 125 |
| B.3 | 1:4 Prograde Coplanar Dual AGN with Observational Constraints . . . .    | 126 |
| B.4 | 1:4 Inclined Dual AGN with Observational Constraints . . . . .           | 126 |
| B.5 | 1:10 Prograde Coplanar Dual AGN with Observational Constraints . . .     | 127 |
| B.6 | 1:2 Elliptical-Spiral Dual AGN with Observational Constraints . . . . .  | 127 |
| B.7 | 1:2 Elliptical-Spiral (with gas) Dual AGN with Observational Constraints | 129 |

# LIST OF TABLES

## Table

|     |   |     |
|-----|---|-----|
| 2.1 | Simulation Parameters . . . . .                               | 19  |
| 3.1 | Nuclear Disruption Results and BH Binary Timescales . . . . . | 36  |
| 4.1 | Dual AGN Timescales . . . . .                                 | 74  |
| 4.2 | Dual Fractions . . . . .                                      | 79  |
| B.1 | Remaining Dual Fractions for Spiral-Spiral Mergers . . . . .  | 128 |
| B.2 | Dual Fraction for Elliptical-Spiral Mergers . . . . .         | 128 |

# LIST OF APPENDICES

## Appendix

|   |     |
|---|-----|
| A GASOLINE: Details of the N-body SPH Code . . . . .                  | 115 |
| B Supplementary Material: Dual AGN Observability Timescales . . . . . | 124 |



# ABSTRACT

Observed scaling relations suggest an evolutionary link between massive black holes (BHs) and their host galaxies. We investigate the coevolution of BH and host in galaxy mergers, which drive active galactic nuclei (AGN) activity, produce BH mergers, and lead to starbursts and morphological transitions in galaxies. Furthermore, we focus on the most cosmologically relevant galaxy mergers: unequal mass mergers at high redshift ( $z = 3$ ). Using high resolution N-body SPH simulations, we track star formation, BH accretion, and associated feedback as the BHs move from separations of tens of kiloparsecs to tens of parsecs. We focus on the role of merger triggered gaseous inflows in driving both central starbursts and efficient BH accretion. We find that the efficiency of BH pairing depends sensitively on the strength of central star formation in the secondary galaxy. Strong gas inflows build up a central stellar cusp that is denser than the primary galaxy, leading the secondary's nucleus to disrupt the nucleus of the larger primary galaxy and resulting in a short timescale (10-20 Myr) for the formation of a BH binary. If the secondary instead experiences weak inflows and strong ram pressure from the primary's disk, the secondary's nucleus is disrupted due to tidal shocks and binary formation is delayed. We also consider simultaneous accretion onto both BHs, testing when and for how long accretion is triggered at a number of observability thresholds. We find that strong dual AGN activity occurs in the late stages of the mergers, at small separations of a few kiloparsecs. Most of the BH accretion is not simultaneous, limiting the observable dual AGN fraction. Finally, we consider the evolution of BHs in low mass systems with quiet merger histories, probing the distribution of BHs on the low mass end of the observed scaling relations. We evolve a population of seed BHs in a Milky Way halo and find that the BH population in dwarf galaxies has not grown much since forma-

tion, providing an indicator of the original BH seed formation mechanism. We derive the BH occupation fraction and mass distribution for a range of dwarf galaxies.

# CHAPTER 1

## Introduction

In the past several decades, our knowledge of black holes (BHs) has evolved significantly. Supermassive BHs with masses ranging from  $10^5 - 10^{10} M_{\odot}$  are now thought to reside at the centers of most galaxies (Richstone et al., 1998; Ferrarese & Ford, 2005). This includes the Milky Way, which hosts a BH with a mass of  $4 \times 10^6 M_{\odot}$ , whose gravitational influence has been directly observed on stars in the Galactic center (e.g. Ghez et al., 2008; Gillessen et al., 2009). In other galaxies, dynamical mass measurements depend instead on modeling the integrated stellar dynamics or following the motion of ionized gas near the center, since individual stars cannot be resolved (Kormendy & Richstone, 1995). Uncertainties in modeling the galaxies (mass to light ratios, triaxiality, and the impact of the dark matter halo) contribute to an overall factor of two uncertainty in these mass estimates. Water megamaser detections (e.g. Nakai et al., 1993; Moran et al., 1999), which probe Keplerian motion around the central BH, yield tighter mass measurements, but are difficult to detect and require a specific line of sight (edge-on disks). In active galaxies where broad emission lines can be observed, the time delay in the emission lines responding to variability in the continuum provides a mass indicator (Peterson et al., 2004). This technique, called reverberation mapping, suffers from uncertainties in geometrical factors and is generally normalized to agree with stellar dynamical measurements. The tightest mass constraints come from water masers and the proper motion of stars in our own Galactic center, whereas other techniques yield a mass estimate with a factor of a few uncertainty.

Intriguingly, the masses of supermassive BHs are seen to correlate with the properties of their hosts galaxies, including the mass and luminosity of the galaxy spheroid

and the central velocity dispersion (Magorrian et al., 1998; Ferrarese & Merritt, 2000; Gebhardt et al., 2000; Marconi & Hunt, 2003; Häring & Rix, 2004; Gültekin et al., 2009). The observed relationships suggests an evolutionary link between supermassive BHs and their hosts. Figure 1.1 shows the  $M_{BH}-\sigma$  relation from Gültekin et al. (2009) for galaxies with dynamical BH mass estimates. The correlation between BH and host spans several orders of magnitude in BH mass and across galaxies with different morphologies that contain a significant spheroidal component (i.e. a bulge).

BHs are generally unimportant in the total mass budget of galaxies, having masses of order 1/1000 the mass of the host bulge. However, the observed scaling relations suggest that the BH may be important to the overall evolution of the galaxy, perhaps even regulating the growth of the galaxy. As a BH accretes, it produces feedback on the surrounding environment. For a supermassive BH and high accretion rates, the outflows may prevent further accretion and shut down star formation in the host (Silk & Rees, 1998; Fabian, 1999; Wyithe & Loeb, 2003; Di Matteo et al., 2005). In this scenario, the BH regulates the growth of the host, enforcing the observed scaling relations. Actively accreting BHs are extremely efficient engines for extracting energy from infalling gas. At high accretion rates, the luminosity of a BH can rival that of the entire host galaxy. In another scenario, the galaxy instead controls the flow of gas down to the BH, with the BH growing through the same processes that build up the bulge of the host. Indeed, a cosmological link between star formation and BH growth is seen (Merloni et al., 2004). While the details of the connection between BHs and their hosts are not well understood, they suggest that a complete picture of galaxy formation and evolution must include an understanding of their central BHs, their formation, growth, and impact on their hosts.

## 1.1 History of Black Hole Detections

John Michell and Pierre-Simon Laplace first speculated about massive objects that even light could not escape in the late 18<sup>th</sup> century. It was not until after the formulation of general relativity by Albert Einstein in 1915 that the theory of BHs received much attention. In the 1960s and 1970s, BHs were proposed as potential engines for

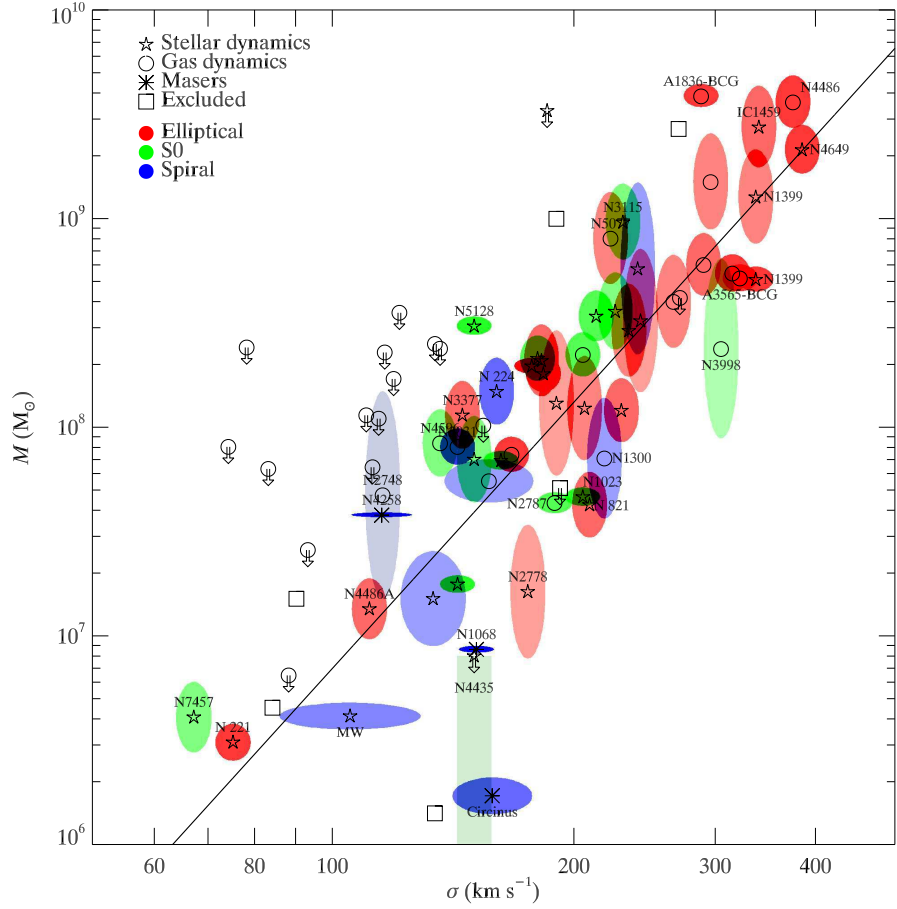


**Figure 1.1.** Relationship between BH mass and  $\sigma$  for galaxies with dynamical BH mass measurements. This figure is reproduced from Gültekin et al. (2009). The color of each error ellipse indicates the Hubble type of the galaxy. The line gives the best fit relation:  $M_{BH} = 10^{8.12} M_{\odot} (\sigma / 200 \text{ km s}^{-1})^{4.24}$ .

quasars and active galactic nuclei (AGN; Salpeter, 1964; Lynden-Bell, 1969; Rees, 1984). The first dynamical evidence for supermassive BHs came from the detection of a rising central velocity dispersion in the giant elliptical galaxy M87, suggesting the presence of a dark central mass of  $5 \times 10^9 M_{\odot}$  (Sargent et al., 1978).

Strong dynamical evidence for a central BH now exists in some 72 nearby galaxies (McConnell & Ma, 2013), with quasars and active galactic nuclei providing evidence for many more. Supermassive BHs appear to be limited to one per galaxy. Some models predict that a population of additional, non-central supermassive BHs may exist, remnants of tidally stripped satellite galaxies, but they would be difficult to detect due to low accretion luminosities (Bellovary et al., 2010). An additional population of intermediate mass BHs, bridging the gap between stellar mass and supermassive BHs, has also been proposed, but there are few strong detections (see HLX-1 and M82 X-1; Farrell et al., 2009; Strohmer & Mushotzky, 2003). The smallest BH yet discovered is in the dwarf galaxy 4395 with a suspected mass of  $3.6 \times 10^5 M_{\odot}$  (Peterson et al., 2005), whereas the largest BHs have masses  $> 10^{10} M_{\odot}$  (van den Bosch et al., 2012).

## 1.2 Black Hole Formation Mechanism

Several scenarios have been proposed for the formation of BHs in high redshift galaxies. The first galaxies that form at high redshift are much smaller than typical galaxies today, and grow hierarchically through mergers. The first BHs form as ‘seeds’ in these galaxies, then grow to form the supermassive BHs observed by astronomers today.

One possible scenario for BH seeding is a top heavy initial stellar mass function in high redshift galaxies (Madau & Rees, 2001). The pristine (metal free) gas in the first galaxies may have formed stars more massive than are commonly seen today, with masses up to several hundred  $M_{\odot}$  (Abel et al., 2000). These first stars, population III stars, would have left behind BHs with masses of  $\simeq 100 M_{\odot}$ . To produce viable BH seeds, the first BHs must be massive enough to grow into the observed high redshift quasars, which have masses of billions of  $M_{\odot}$  at  $z \simeq 6$  (Willott et al., 2003; Barth et al., 2003; Willott et al., 2005). If the first population of stars is not massive enough,

then the BH seeds will likely be too small to grow into the first quasars by the time they are observed.

Another possibility for BH seed formation results from gravitational instabilities in the disks of early galaxies. Local instabilities in very metal poor gas can lead to the formation of a dense star cluster at the center of the galaxy (Devecchi & Volonteri, 2009). Runaway collisions between stars then form a very massive star that leaves behind a  $\simeq 1000 M_{\odot}$  BH upon its death. If the gravitational instabilities are instead global and the inflowing gas does not fragment, an extremely massive ( $M \simeq 10^6 M_{\odot}$ ) star may form at the center of the galaxy. The core of the star collapses to form a small BH that then accretes efficiently from the remaining envelope of the star (Begelman et al., 2006). The BH may then grow up to  $10^4 - 10^6 M_{\odot}$  before the gaseous envelope is disrupted.

The first BHs are thought to form at high redshift,  $z \simeq 10 - 20$ , so the formation mechanism is not directly observable. We do know that the most rapidly growing BHs have reached a few billion  $M_{\odot}$  by  $z = 6 - 7$ , when they are observed as quasars. As the BHs grow through gas accretion and BH-BH mergers, the original seed mass of the BH is overwritten, so observations of supermassive BHs today do not inform us of how they first formed. If a population of seed BHs exists in the present day universe, however, and it has not grown appreciably, it would provide a mechanism for distinguishing among the BH formation mechanisms. Dwarf galaxies have relatively quiet merger histories compared to more massive galaxies and may provide such a population of pristine BH seeds (van Wassenhove et al., 2010). We consider the BH occupation fraction and mass range expected to exist in dwarf galaxies around the Milky Way in Chapter 5.

### **1.3 Black Hole Growth: Accretion and Black Hole Mergers**

Once the BH seeds have formed, they grow through two mechanisms: gas accretion and BH-BH mergers. Their host galaxies grow hierarchically through mergers in the  $\Lambda$ CDM cosmology (White & Rees, 1978), largely in unequal mass mergers and through accretion of dark matter and gas from cosmological filaments.

BH-BH mergers proceed following mergers of galaxies containing central BHs. If the merging galaxies are not too dissimilar in mass (mass ratio  $q \geq 1:10$ ) and are gas rich, the merger is likely to lead to the formation of a BH pair on  $\simeq 100$  pc scales (Kazantzidis et al., 2005; Callegari et al., 2009). The BHs then sink further through dynamical friction (Yu, 2002), forming a BH binary on pc scales. If the binary is able to sink further by ejecting stars through three body interactions (Begelman et al., 1980; Milosavljević & Merritt, 2001) or via gas dynamical processes (Escala et al., 2005), it will coalesce on sub-pc scales via the emission of gravitational waves. BH binaries are expected to exist and one case has been confirmed, a 7 pc binary in the radio galaxy 0402+379 (Rodriguez et al., 2006), but candidate BH binaries remain rare and difficult to confirm. In the future, evidence for BH-BH binaries and mergers may instead come directly from detections of gravitational waves from the mergers themselves (Haehnelt, 1994). The most massive BHs reside in gas poor systems and are expected to grow preferentially through BH-BH mergers resulting from dry (i.e. gas poor) galaxy mergers (Malbon et al., 2007).

BHs accrete gas on sub-pc scales, where the angular momentum of inflowing gas forms an accretion disk. In radiatively efficient, optically thick accretion disks, viscosity transports angular momentum outward and drives accretion onto the BH (Shakura & Sunyaev, 1973). On larger scales, the accretion disk is fed by gravitational torques and instabilities that drive gas inflows toward the BH (Shlosman et al., 1990; Hopkins & Quataert, 2010).

To estimate the overall importance of accretion in the the mass budget of supermassive BHs, the local BH mass density is often compared to the the quasar luminosity function, which provides evidence of past growth via accretion (the Soltan argument, Soltan, 1982). Yu & Tremaine (2002) calculate the local BH mass density via velocity dispersion measurements of galaxies in the Sloan Digital Sky Survey, using the  $M_{\text{BH}} - \sigma$  relation to produce corresponding BH masses expected by scaling relations. Yu & Tremaine compare this density to the quasar luminosity function from the 2dF QSO Redshift Survey and find a similar density, concluding that that supermassive BHs have grown predominantly through accretion in luminous quasar



phases. The quasar luminosity function was updated by Hopkins et al. (2007), using observations in a number of wavelength bands to probe it out to  $z = 6$ . They find that the total quasar luminosity density peaks at  $z \simeq 2.15$ , near the peaks in the cosmic star formation density and galaxy merger rates. Accounting for Compton-thick (obscured) quasars, Hopkins et al. find that the integrated quasar luminosity function is consistent with local estimates of the BH mass density (Marconi et al., 2004; Shankar et al., 2004), in agreement with the results of Yu & Tremaine (2002).

Since observations indicate that the majority of the local BH mass has been built up via gas accretion, we now investigate the most important drivers of active galactic nuclei and quasar activity. Gaseous inflows that feed the central BH can be caused by external processes (i.e. mergers) or internal processes, such as secular bars or mass loss from stars (Ciotti & Ostriker, 2007). Simulations of interacting galaxies suggest that mergers between equal mass galaxies drive strong gaseous inflows that result in starbursts and high BH accretion rates (e.g. Di Matteo et al., 2005). Cisternas et al. (2011) studied the morphologies of galaxies hosting AGN, concluding that most were not involved in a merger. Koss et al. (2010) and Ellison et al. (2011) instead find evidence for enhanced AGN activity in interacting galaxies. We conclude that galaxy interactions are not the sole drivers of AGN activity, but do provide an important mechanism. Given the hierarchical growth of galaxies and scaling relations between BH mass and host properties, galaxy mergers provide an environment for studying the co-evolution of BH and host, through both AGN triggering, feedback, and BH-BH mergers.

## 1.4 Galaxy Mergers

Major mergers occur between galaxies with similar masses (commonly defined as mass ratios of 1:3 or more). These mergers are thought to drive the morphological evolution of galaxies, converting gas rich spiral galaxies into gas poor elliptical galaxies (Toomre & Toomre, 1972; Toomre, 1977; Barnes & Hernquist, 1992). The gas in the galaxies is consumed via star formation and BH accretion or expelled from the resulting galaxy through outflows caused by feedback. Major mergers have been observed to trigger

starbursts, or temporary enhancements in the star formation rate, in systems such as the Antennae Galaxies (NGC 4038/4039) where the star formation rate is estimated to be  $20 M_{\odot} \text{ yr}^{-1}$  (Zhang et al., 2001). Luminous infrared galaxies are thought to be the result of gas rich major mergers leading to star formation rates of  $100 M_{\odot} \text{ yr}^{-1}$  or more as well as obscured quasar activity (Sanders et al., 1988).

Minor mergers occur when one galaxy is significantly larger than the other. In these mergers, the primary (larger) galaxy is relatively unperturbed dynamically. The secondary (smaller) galaxy, on the other hand, is strongly affected by the tidal field of the primary galaxy. Minor mergers are more common than major mergers and proceed more slowly, generally lasting many billions of years (Taffoni et al., 2003). The Milky Way is thought to be currently undergoing minor mergers with the Large and Small Magellanic Clouds, each about two orders of magnitude less massive than the Milky Way.

Studying collisions between galaxies is a complex problem that is generally treated computationally. In N-body simulations, each galaxy is broken up into many particles that interact gravitationally. Ideally, each particle would represent an individual star. However, simulating a system such as the Milky Way would require  $\simeq 10^{11}$  particles for the stellar component alone, which is prohibitively expensive in computational cost. Instead, individual particles represent hundreds of stars or more depending on the resolution of the simulation. The first computational simulations of galaxy interactions contained only hundreds of particles and probed the tidal response of disks to passing companions (Toomre & Toomre, 1972). Since then, developments and improvements have included implementations of hydrodynamics via smoothed particle hydrodynamics (Monaghan, 1992), star formation (e.g. Katz, 1992), radiative cooling (Katz et al., 1996), and BH accretion and feedback (Springel et al., 2005). Additionally, computational resources have greatly improved, allowing simulations to be run with more than  $10^7 - 10^8$  particles.

Following the dynamics of BHs accurately is particularly difficult given the range of scales involved in simulating galaxy interactions. The dark matter halo of each galaxy on scales of hundreds of kpc contains most of the mass and determines the

orbit of the interaction. On scales of tens of kpc, the gaseous disk of each galaxy (in simulations of spiral galaxies) responds to the merger, driving gaseous inflows down to scales of hundreds of parsecs (Mihos & Hernquist, 1996). On still smaller scales of less than a parsec, infalling gas forms an accretion disk around the central BH. It is generally not possible to resolve the small scale processes involving BHs such as accretion and BH binary evolution in simulations that also resolve the host galaxy. Instead, sub-grid models are used in an attempt to model unresolved physics, including BH accretion and feedback, star formation, and supernova feedback. These models include free parameters that can be tuned to match observations, but can only match observations in a time averaged or spatially averaged sense. For example, star formation models are generally tuned to globally reproduce a Kennicutt-Schmidt star formation law (Kennicutt, 1998), but cannot resolve star formation in individual molecular clouds.

Numerous simulations have considered the triggering of BH accretion through equal mass galaxy mergers (Springel et al., 2005; Di Matteo et al., 2005; Robertson et al., 2006; Hopkins et al., 2006; Johansson et al., 2009). Several studies have also considered gas dynamics in minor mergers both with (Younger et al., 2008) and without (Cox et al., 2008) BHs. These studies have generally resolved scales of  $\simeq 100$  pc and focused on BH accretion and the evolution of galaxies along observed scaling relations, but not the dynamics of BH pairing and binary formation. Instead, it is assumed that BHs merge efficiently upon reaching the resolution limit of the simulation (Springel et al., 2005). Additional mechanisms have been introduced in some studies to ensure efficient BH merging, including repositioning of BHs to the local potential minimum (Johansson et al., 2009) or the inclusion of a drag force acting on the BHs (Younger et al., 2008). Mayer et al. (2007) studied the formation of BH binaries in equal mass mergers and found that in gas rich merger remnants, BHs can sink and form a pc-scale binary on timescales of Myr. Kazantzidis et al. (2005) and Callegari et al. (2009) instead focused on the dynamics of BH pairing in minor mergers. However, these studies of BH pairing and binary formation have ignored the effects of accretion onto the BHs.

On smaller scales, the evolution of BH binaries in circumnuclear disks has been studied using idealized initial conditions (Escala et al., 2005; Dotti et al., 2007, 2009; Cuadra et al., 2009). These simulations show that BH pairs can rapidly sink and form BH binaries in a gas rich environment, but they sacrifice their link with the large scale dynamics of the host galaxy in order to focus on the nuclear region with high (pc-scale) resolution.

We present simulations that bridge the gap between large scale, low resolution simulations of galaxy mergers and the small scale, high resolution simulations of BH binary evolution. Our simulations resolve  $<20$  pc scales in order to accurately track the motion of the nuclei of the merging galaxies and study the efficiency of BH pairing on  $< 100$  pc scales, providing a more realistic environment for the evolution of a BH binary. We consider mergers meant to represent the most common mergers in the  $\Lambda$ CDM cosmology rather than relatively rare equal mass mergers at  $z = 0$ . We focus, therefore, on unequal mass mergers with mass ratios of 1:2, 1:4, 1:6, and 1:10. Our simulations begin at  $z = 3$ , near the peak of the cosmic merger rate, when galaxy mergers were more common than at low redshift.

## 1.5 Outline

In Chapter 2, we discuss the numerical setup of our galaxy merger simulations, including the specifics of the sub-grid models and how the galaxies and mergers are initialized. Orbital parameters are chosen to agree with the results of cosmological galaxy formation simulations. We also discuss the N-body smoothed particle hydrodynamics (SPH) code GASOLINE which is used to produce our results.

In Chapter 3, we focus on the dynamical evolution of the BHs in our galaxy mergers and the prospects for efficient BH pairing and binary formation. We find that the secondary galaxy generally experiences stronger tidal forces than the primary galaxy in unequal mass mergers, driving higher central star formation rates. The secondary galaxy develops a dense stellar cusp that helps it survive the tidal interaction with the more massive primary galaxy, leading to the successful formation of a BH pair with a short timescale for the formation of a binary. In some cases, the secondary

galaxy becomes denser on small scales and disrupts the primary galaxy’s nucleus late in the merger.

In Chapter 4, we focus on the triggering of BH accretion in our merger simulations. We discuss the timing of AGN activity, the correlation with the central star formation that drives BH pairing, and the evolution of the mass ratio of the two BHs. We also consider the triggering of dual AGN, or merging systems where the central BHs in both galaxies are actively accreting simultaneously. Our results show that strong accretion is triggered late in each merger, following close passages between the galaxies. Strong inflows in the secondary galaxy drive higher relative accretion rates than in the primary galaxy, increasing the mass ratio of the BHs from the initial ratio. We consider the effects of observational limitations in detecting our simulated dual AGN activity and find good agreement with low redshift observations of dual AGN. We find that major mergers produce the strongest correlated accretion onto both BHs and therefore the longest dual AGN timescales. The results of Chapter 4 are an extension of Van Wassenhove et al. (2012).

In Chapter 5, we consider the properties of BHs in low mass systems, where BH masses may deviate from observed scaling relations. We focus on possible BHs in dwarf galaxies which may not have grown significantly since their formation at high redshift. To examine the properties of the BH population, we evolve several BH seed populations within a Milky Way halo from high redshift to today. We consider massive but rare BH seeds produced by gas-dynamical instabilities and more common but smaller BHs produced as remnants of Population III star formation. We follow the dynamical evolution of the dwarf galaxies with the host halo to produce a realistic dwarf population. We find that the BH population in dwarf galaxies has not grown much since formation, providing a clue to the formation process. However, our massive seeds that are large enough to be detected are very rare, whereas the more common Pop III seeds are too small to be reliably detected. Chapter 5 is reproduced from van Wassenhove et al. (2010).

We include additional material in two appendices. Appendix A contains a thorough discussion of the N-body SPH code GASOLINE, detailing the recipes for ra-

diative cooling, star formation, supernova feedback, BH accretion and BH feedback. We describe the structure of the code, including the design of the particle tree used to improve the code's runtime scaling. Appendix B contains supplementary material from Chapter 4.

## CHAPTER 2

# Numerical Methods

In this chapter, we describe the numerical setup of our simulations, motivating the parameter space that we study as well as our parameter choices in initializing our galaxies and orbits. We also provide a description of the N-body smoothed particle hydrodynamics (SPH) code GASOLINE, including a brief description of the sub-grid models for star formation, BH accretion, and feedback. Additional information on GASOLINE can be found in Appendix A.

Our goal is to study the coevolution of BH and host galaxy under cosmologically relevant conditions. While previous works have predominantly studied low redshift mergers between equal mass galaxies, we choose instead to focus on unequal mass mergers, which are expected to be the most common in the  $\Lambda$ CDM cosmology (Blumenthal et al., 1984; Lacey & Cole, 1993). Our simulation suite includes mass ratios of 1:2, 1:4, 1:6, and 1:10 set at  $z = 3$ , corresponding to the peak of the cosmic merger rate. We choose orbital parameters that match those of the most common halo mergers in cosmological simulations of galaxy formation, placing them on near parabolic orbits (Benson, 2005).

In order to follow the dynamics of the BHs as accurately as possible, we choose a very high resolution ( $<20$  pc) for the baryonic component of our galaxies. Relevant scales for the BHs are the radius where a BH binary is formed (separations of  $\simeq 1 - 10$  pc) and the Bondi radius ( $R_B = 2GM_{\text{BH}}/c_s^2$ , similar to the scale for binary formation), which is the scale where the BH accretion rate is determined under spherical Bondi accretion. Ideally, we would resolve these scales as well as smaller scales to follow the evolution of the BH binary, but this resolution would be prohibitively expensive if we also include the entirety of the host galaxy on larger scales. Our choice of resolution

allows us to accurately track BH accretion and the formation of a BH pair on  $<100$  pc scales, a limitation in previous simulations, while also considering a wide parameter space including many mergers. Additionally, our resolution combined with the sub-grid models in GASOLINE produce a dynamic, multi-phase interstellar medium. During episodes of strong star formation, we resolve the formation of massive star clusters ( $M = 10^5 - 10^8 M_\odot$ ). Our realistic interstellar medium allows us to accurately trace gas inflows from kpc-scales down to pc-scales where the gas accretes onto the central BH and contributes to the formation of a dense stellar cusp.

## 2.1 GASOLINE

We use the N-body SPH code GASOLINE (Wadsley et al., 2004) to perform our simulations. GASOLINE is an extension of the pure gravity tree code pkdgrav (Stadel, 2001). GASOLINE has been used in a cosmological context to produce realistic galaxies following the mass-metallicity relation (Brooks et al., 2007) and Tully-Fisher relation (Governato et al., 2009). The addition of a physically motivated supernova prescription has led to the formation of bulgeless dwarf galaxies with shallow dark matter density profiles (Governato et al., 2010). Appendix A contains more details on the code and the included sub-grid models. The most important features are briefly summarized here.

GASOLINE includes explicit line cooling for atomic hydrogen and helium as well as metals. Gas particles range in temperature from 10 K to  $10^9 K$ . Cold, dense ( $T < 6000$  K,  $\rho > 100 \text{ amu cm}^{-3}$ ) gas can form stars, creating new collisionless star particles. Young star particles impact their environment through stellar winds and type II supernovae (Stinson et al., 2006). Supernova feedback mimics the expansion of a blastwave (Chevalier, 1974; McKee & Ostriker, 1977), turning off cooling in nearby gas particles to ensure that the thermal energy is effective in regulating star formation. Star formation rates scale with the local gas density as  $\rho^{1.5}$  and are normalized to match a Kennicutt-Schmidt star formation law (Kennicutt, 1998). The normalization parameter,  $c^*$ , is set to 0.015 and represents the fraction of the local gas density converted into stars in a free fall time.



Black holes are implemented as sink particles that accrete from nearby gas particles according to the Bondi-Hoyle-Lyttleton formula, based on locally averaged gas properties (Bondi, 1952):

$$\dot{M}_{\text{BH}} = \frac{4\pi G^2 M_{\text{BH}}^2 \rho_g}{(c_s^2 + v^2)^{3/2}}. \quad (2.1)$$

Here  $M_{\text{BH}}$  is the mass of the BH,  $\rho_g$  is the local gas density,  $c_s$  is the local sound speed, and  $v$  is the velocity of the BH relative to the surrounding medium. The overall accretion rate in any timestep is limited by the Eddington accretion rate, assuming spherical accretion from Hydrogen gas:

$$\dot{M}_{\text{Edd}} = \frac{L_{\text{Edd}}}{\epsilon_r c^2} = \frac{4\pi G M_{\text{BH}} m_p}{\sigma_T \epsilon_r c}, \quad (2.2)$$

where  $\epsilon_r$  is the radiative efficiency, set to 10 percent,  $m_p$  is the proton mass, and  $\sigma_T$  is the Thomson cross section for an electron. Black hole accretion injects thermal energy into the nearest gas particle according to:

$$\dot{E} = \epsilon_r \epsilon_f \dot{M}_{\text{BH}} c^2. \quad (2.3)$$

The feedback efficiency was set such that black hole growth during a merger matches local scaling relations, yielding a value of  $\epsilon_f = 0.001$  (see Appendix A for more details). As with supernova feedback, cooling is disabled for affected gas particles to prevent them from immediately radiating the energy away. This feedback model enables the black hole to effectively regulate its accretion rate.

GASOLINE is a very portable code, using a compact machine dependent layer for architecture dependent calls such as memory sharing between processors. The use of hierarchical timesteps allows particles with short dynamical timescales to be updated more often than other particles, achieving the force accuracy necessary for accurate integration and allowing the code to simulate problems involving a large range of densities. The timestepping scheme and tree structure used for force calculations and SPH neighbor searches cause GASOLINE to scale very well with many processors.

The simulations presented here were run on NASA’s Pleiades and Teragrid’s

Kraken clusters. High resolution production runs were performed on 128 to 256 processors with a complete simulation generally requiring three to four weeks of computational time. Simulations with the most unequal mass ratios (1:6, 1:10) were the most expensive, requiring more particles to achieve the required resolution and lasting longer than the 1:2 and 1:4 mergers. Low resolution test simulations were performed on the local Galaxy cluster in the University of Michigan Astronomy department.

## 2.2 Resolution

We normalize the particle masses across both galaxies in all simulations because we are interested in following the interaction between the galaxies and there will be a significant exchange of particles. We choose our particle masses to achieve the resolution necessary to resolve a dynamic, multiphase interstellar medium and to follow the dynamics of our BHs. Where possible, the resolution is also normalized between simulations. The softening length for star particles was set to 10 pc with an individual particle mass of  $3.3 \times 10^3 M_{\odot}$ . The gas particle softening length (defined as the distance to the 32<sup>nd</sup> closest gas particle) was set to match the peak value of the smoothing length distribution for all gas particles in a high resolution test simulation, yielding a value of 20 pc for a particle mass of  $4.6 \times 10^3 M_{\odot}$ . These particle masses have the added advantage of keeping the masses of newly formed star particles, which form with half the mass of a gas particle, close to the mass of existing star particles. The BH softening length was set to 5 pc in all runs.

The dark matter particle mass was chosen to limit excursions of black holes from the center of each galaxy. The maximum dark matter particle mass was set to 1/7 of the smallest black hole mass. For the 1:2 and 1:4 simulations, the mass was set to  $1.01 \times 10^5 M_{\odot}$ , yielding a softening length of 30 pc. For the 1:6 and 1:10 simulations, the particle mass was lowered to reflect the low mass of the black hole in the secondary galaxy. The 1:6 simulation used a dark matter particle mass of  $7.56 \times 10^4 M_{\odot}$  and softening length of 27 pc. The 1:10 simulation used a particle mass of  $3.9 \times 10^4 M_{\odot}$  and softening length 24 pc. The particle masses listed above yield total particle numbers of six to twelve million, depending on the mass ratio of the merger.

## 2.3 Galaxy Models

### 2.3.1 Spiral Galaxies

Each galaxy is composed of a dark matter halo, a mixed stellar and gaseous disk, and a stellar bulge. The dark matter halo is represented by a spherical Navarro-Frenk-White profile (Navarro et al., 1996) with spin parameter  $\lambda = 0.04$ . The dark matter halo concentration parameter is initialized to  $c = 12$  according to the redshift scaling found in Bullock et al. (2001). The disk has an exponential density profile with total mass  $0.04M_{\text{vir}}$ . The gas in the disk has a mass fraction of  $f_{\text{gas}} = 0.3$ . Observations of high redshift galaxies that are actively forming stars suggest that they may have higher gas fractions (Tacconi et al., 2010). The value used here was chosen for consistency with the previous work of Callegari et al. (2009) and Callegari et al. (2011) that we used for comparison. The stellar bulge has a spherical Hernquist (1990) density profile with total mass  $0.008M_{\text{vir}}$ .

Following the model of Mo et al. (1998), the disk and bulge scale lengths are chosen to place the galaxies on the Tully-Fisher relation. To transform the  $z = 0$  galaxies to the merger redshift of  $z = 3$ , the masses, positions, and softening lengths are scaled down by a factor of  $H(z = 3)/H_0$  while keeping  $V_{\text{vir}}$  constant. The primary galaxy in each simulation has  $V_{\text{vir}} = 145 \text{ km s}^{-1}$ , a  $z = 0$  virial mass of  $10^{12} M_{\odot}$ , and a  $z = 3$  virial mass of  $2.24 \times 10^{11} M_{\odot}$ . The mass of the secondary in each run scales according to the mass ratio.

We place a single BH at the center of each galaxy after the galaxy has been initialized. Its mass is set according to the  $M_{\text{BH}}\text{-}M_{\text{bulge}}$  relation (Marconi & Hunt, 2003). The black hole in the primary galaxy in each simulation is initially set to  $3 \times 10^6 M_{\odot}$ . The black hole in the secondary galaxy has a mass proportional to the mass ratio between the galaxies, producing a minimum initial mass of  $3 \times 10^5 M_{\odot}$  in the 1:10 merger.

For simplicity, each galaxy is initialized with solar metallicity and a uniform stellar population with an age of 2 Gyr to reflect the young age of the universe at  $z = 3$ . Without any existing feedback to heat the gas, much of the gas initially cools and

vigorously forms stars. To avoid an unphysical burst of supernovae at the beginning of our mergers, we evolve the galaxies in isolation over 100 Myr. During this time, the star formation efficiency  $c^*$  is increased from 0.005 to the normal value of 0.015, increasing by 0.005 every 50 Myr. At the end of this period, we reset the BH mass to its initial value.

### 2.3.2 Gas Poor Galaxies

We also consider mergers between gas poor primary galaxies and gas rich spiral secondary galaxies. We model our gas poor galaxies after low redshift ellipticals. These galaxies consist of a dark matter halo and a stellar component, each represented by a spherical Hernquist (1990) profile. The dark matter halo has a spin parameter  $\lambda = 0.04$  and scale length 22 kpc, chosen to resemble a Navarro-Frenk-White profile following the method in Springel et al. (2005). The stellar component has a total mass of  $0.05M_{\text{vir}}$ , no rotation, and a scale length of 0.5 kpc, chosen based on the scale length of early type galaxies from the Sloan Digital Sky Survey (Shen et al., 2003). The  $z = 0$  virial mass of the elliptical galaxies we consider is  $2 \times 10^{12} M_{\odot}$ , yielding a  $z = 3$  virial mass of  $4.48 \times 10^{11} M_{\odot}$ . Particle masses are chosen to match those of the spiral galaxy in each merger. Given the large mass of the spheroidal component in these galaxies, the BH mass is significantly larger than in the spiral galaxies. The BH particle mass is initially  $4 \times 10^7 M_{\odot}$ . In one merger, we also consider a galaxy with a low mass hot gaseous halo. The gaseous halo has a total mass of 5 percent of the stellar mass and the same spatial distribution. The temperature of the halo is set to place it initially in hydrostatic equilibrium. In this case, the gas halo cools, turning the galaxy into an Sa type galaxy.

## 2.4 Orbital Parameters

We choose orbital parameters common to halo mergers in cosmological simulations of galaxy formation (Benson, 2005), where typical orbits have an eccentricity near  $e = 1$  and half of all mergers have an eccentricity between 0.9 and 1.1. Khochfar & Burkert (2006) find that 85 percent of merging halo orbits have initial pericenter

| Mass Ratio        | $\theta_1$ | $\theta_2$ | $e$  | $R_{\text{peri}}$ | $R_{\text{initial}}$ |
|-------------------|------------|------------|------|-------------------|----------------------|
| Spiral-Spiral     |            |            |      |                   |                      |
| 1:2               | 0          | 0          | 1.02 | 0.3               | 1.05                 |
| 1:2               | $\pi/4$    | 0          | 1.02 | 0.225             | 1.05                 |
| 1:2               | $\pi$      | 0          | 1.02 | 0.225             | 1.05                 |
| 1:2               | 0          | $\pi$      | 1.02 | 0.225             | 1.05                 |
| 1:4               | 0          | 0          | 1.03 | 0.228             | 1.05                 |
| 1:4               | $\pi/4$    | 0          | 1.03 | 0.228             | 1.05                 |
| 1:6               | 0          | 0          | 1.03 | 0.228             | 1.05                 |
| 1:10              | 0          | 0          | 1.03 | 0.228             | 1.05                 |
| Elliptical-Spiral |            |            |      |                   |                      |
| 1:2 (no gas)      | 0          | 0          | 1.04 | 0.245             | 1.03                 |
| 1:2 (5% gas)      | 0          | 0          | 1.05 | 0.264             | 1.03                 |

**Table 2.1.** Orbital parameters for our simulations.  $\theta_1$  and  $\theta_2$  are the angles between the spin axis and the orbital angular momentum axis for each galaxy.  $e$  is the eccentricity of the orbit.  $R_{\text{peri}}$  is the initial pericenter distance as a fraction of the virial radius of the larger galaxy.  $R_{\text{initial}}$  is the initial separation divided by the sum of the virial radii of the merging galaxies. For the elliptical-spiral mergers, the additional label next to the mass ratio applies to the primary galaxy only.

passages in excess of  $0.1R_{\text{vir},1}$ , the virial radius of the larger galaxy. Most simulations of galaxy mergers consider smaller pericenter passages instead, to save computational time, producing more direct collisions. We set the initial pericenter distance near 20 percent of  $R_{\text{vir},1}$ . The initial separation between the galaxies is set near the sum of the virial radii. We summarize the orbital parameters for each simulation in Table 2.1.

We vary the angle between each galaxy’s angular momentum axis and the overall orbital angular momentum vector, given by  $\theta$  in Table 2.1. We consider prograde coplanar mergers, in which  $\theta_1$  and  $\theta_2$ , the angles for the primary and secondary, are both 0. In our inclined mergers, we set  $\theta_1$  to  $\pi/4$ . Lastly, we consider retrograde coplanar mergers in which one of the galaxies is anti-aligned with the orbital angular momentum axis.

## 2.5 Conclusions

We present simulations of galaxy mergers that focus on the mergers most relevant to the cosmological growth of galaxies: unequal mass mergers at high redshift ( $z = 3$ ). Our high resolution ( $< 20$  pc) simulations include radiative cooling, star formation,

supernova feedback, and BH accretion and feedback. The balance between supernova feedback and cooling produces an inhomogeneous, multi-phase interstellar medium. We follow the coevolution of our galaxies and their central massive BHs. Chapters 3 and 4 focus on the results of these simulations.

In Chapter 3, we follow the triggering of central star formation in our galaxies by gaseous inflows. We focus on the build up of a dense central cusp in each galaxy and follow the interaction of the nuclei late in the merger. Following the disruption of one or both nuclei by tidal shocks, we discuss the timescale for the formation of a BH binary in the merger remnant.

In Chapter 4, we instead focus on the BH accretion throughout our mergers. We track how and when the interaction between the galaxies drives gaseous inflows that lead to strong accretion. We consider the relative growth in the two BHs as well as the amount of simultaneous accretion between them. Finally, we compare our results to recent observational surveys of dual active galactic nuclei.

## CHAPTER 3

# Nuclear Coups in Unequal Mass Galaxy Mergers

### 3.1 Introduction

Observational evidence suggests that most massive galaxies contain supermassive black holes with masses in the range of  $10^6 M_\odot - 10^9 M_\odot$  (Ferrarese & Ford, 2005). If all massive galaxies contain BHs, then galaxy mergers may lead to mergers between their central BHs. BH mergers provide a complementary mechanism for BH growth to accretion, which is enhanced during galaxy mergers (Chapter 4). In lower mass BHs ( $M_{\text{BH}} \simeq 10^6 - 10^8 M_\odot$ ), accretion is the dominant mechanism for growth, but BH-BH mergers dominate in the highest mass BHs, which reside preferentially in gas poor systems (Malbon et al., 2007). BH mergers also lead to high signal to noise bursts of gravitational waves, an important source for proposed space-based laser interferometers and the ongoing Pulsar Timing Array (Hobbs et al., 2010), which will be sensitive to BH mergers.

We study here the formation and evolution of BH pairs. We define a BH pair as two BHs residing in a single galaxy on scales of tens of pc to kpc. In a pair, the BHs are not bound to each other and sink toward the center of the host galaxy under the effects of dynamical friction. Should the BHs reach smaller scales of  $\simeq 10$  pc, they become gravitationally bound to each other and a binary is formed. For a BH embedded in a singular isothermal sphere, a binary forms at a separation of  $a = GM/2\sigma^2$ , where the mass of the BHs exceeds the enclosed mass in stars, gas, and dark matter. In the merger remnants resulting from our galaxy mergers, a binary would form at separations of 3-25 pc. If a binary forms, it then continues to shrink under dynamical friction until the formation of a hard binary, when dynamical friction

becomes inefficient (Yu, 2002). In gas-poor systems, the evolution of a hard binary is dominated by three body interactions with nearby stars (Milosavljević & Merritt, 2001). In gas-rich systems, friction against the gaseous background may continue to shrink the binary (Escala et al., 2005; Mayer et al., 2007; Dotti et al., 2007). Once the binary reaches milliparsec scales, gravitational wave emission is efficient and the binary quickly coalesces. If the first step of this process is inefficient, however, then the subsequent steps do not occur, forming a bottleneck leading up to the formation of a BH binary. The merger of two galaxies does not ensure the merger of their BHs and it is vital to study the efficiency of the first step of the process: the formation of a BH pair.

Particularly in unequal mass galaxy mergers, which are the most common in the  $\Lambda$ CDM cosmology, the secondary galaxy is prone to tidal stripping and tidal shocks from the primary galaxy. These effects can completely disrupt the secondary galaxy early in a merger, stranding the secondary BH,  $BH_2$ , far from the primary BH,  $BH_1$ , at kpc separations. A dense stellar cusp is vital to the formation of a close BH pair on  $<100$  pc scales. If the secondary has a dense stellar cusp and a deep potential well, it is more resistant to tidal stripping and tidal shocks. Additionally, it implies a large bound mass, decreasing the dynamical friction timescale and leading to faster pairing and binary formation. Kazantzidis et al. (2005) and Callegari et al. (2009) consider both gas poor and gas rich minor mergers to study the efficiency of BH pairing. They conclude that gas is vital to the survival of the secondary galaxy throughout the merger. Central gas in the secondary galaxy dissipates energy from tidal shocks and forms stars, increasing the central stellar density. Gas poor mergers instead resulted in inefficient pairing, delaying the formation of a BH binary in some cases by more than a Hubble time.

We expand on their work here, considering mergers between gas rich galaxies with varying mass ratios and orientations. We focus on the mechanisms that trigger star formation during the mergers and follow the build up of central mass in both galaxies. Lastly, we follow the interaction of the stellar nuclei on  $<100$  pc scales and discuss the prospects for the formation of a BH binary. In Section 3.2, we study the physical



processes acting on the galaxies throughout each merger, leading to gaseous inflows, enhanced central star formation, and the merger of the galactic nuclei. We generalize these results to our full suite of mergers in Section 3.3. Finally, we compare our simulations and results to existing theoretical and observational work in Section 3.4.

## 3.2 Dynamical Evolution

In this section, we describe the dynamics of the galaxy mergers, focusing on the physical processes influencing the dynamics of galaxy mergers. In particular, we highlight the processes that modify the gaseous and stellar content of galaxies. The removal or addition of gas and stars affects the overall orbital decay, and in particular the evolution of the nuclei and their embedded BHs. Here the nucleus of each galaxy refers to the material within  $\simeq 100$  pc of the center of the galaxy. We focus on the nucleus because the presence of a dense envelope surrounding the BH is crucial to the dynamics and eventual formation of a BH binary (Yu, 2002).

We use the 1:4 prograde coplanar merger to illustrate the general properties and phases of the merger. In Section 3.3, we discuss the remaining simulations (outlined in chapter 2) and how they differ from the general picture presented here. In particular, we focus on the impact of the merger mass ratio and orbital parameters on triggered star formation and the outcome of the nuclear merger.

### 3.2.1 Tidal Torques

During close pericenter passages between the galaxies, gravitational torques between the galaxies lead to the formation of stellar and gaseous bars. The gaseous bar tends to lead the stellar bar, causing a torque upon the gas that removes angular momentum (Mihos & Hernquist, 1996). The angular momentum loss in the gas causes gaseous inflows from kpc-scales into the nuclear region. The bottom panel of Figure 3.1 shows the angular momentum per unit mass in the central kpc of each galaxy in the 1:4 prograde coplanar merger. We focus on the angular momentum in the central kpc rather than in the central 100 pc because large scale inflows are important for funneling gas into the central regions of each galaxy. In agreement with the findings

of Mihos & Hernquist, we find that the presence of a bulge stabilizes each galaxy against the formation of a bar instability during the first pericenter passage. Accordingly, there is no loss of angular momentum in the gas. At second pericenter and at subsequent pericenter passages, however, torques lead to strong angular momentum loss and gaseous inflows. We note that the response of the primary galaxy is considerably weaker than that of the secondary, with the primary’s disk losing little angular momentum until late in the merger. The relatively more massive primary produces a strong tidal field and it is not significantly perturbed by the secondary’s weaker tidal field.

### 3.2.2 Ram Pressure

When the gaseous disks of the galaxies collide, they do not pass through each other as the stars and dark matter do, but feel pressure from the gas in the opposing disk. Clouds of atomic and molecular gas collide and are ionized, but the resulting dense gas quickly cools (Harwit et al., 1987). The collisions dissipate the orbital energy of the gas in the galaxies, creating the gaseous bridge that links the galaxies after the second pericenter passage. We consider the effects of ram pressure from the primary’s disk on the secondary’s disk (Gunn & Gott, 1972; Mo et al., 2010):

$$P_{\text{ram}} = \rho_{\text{prim}} v^2 > 2\pi G \Sigma_*(R) \Sigma_{\text{ISM}}(R) \quad (3.1)$$

where  $\rho_{\text{prim}}$  is the gas density of the primary galaxy’s disk,  $v$  is the relative velocity between the galaxies during the collision, and  $\Sigma_*(R)$  and  $\Sigma_{\text{ISM}}(R)$  are the stellar and gaseous surface densities in the secondary galaxy at a radius  $R$ . If the ram pressure,  $P_{\text{ram}}$ , is higher at a given radius  $R$ , then the gas in the secondary’s disk at that radius will be stripped during the collision.

We note that this prescription for ram pressure is generally used to describe ram pressure from a hot, low density medium, whereas we are considering direct collisions between cold, dense gas clouds. The gaseous disks are inhomogeneous and the overall collision is short, lasting  $\simeq 50$  Myr. Nonetheless, Equation 3.1 is instructive. To

illustrate how the impact of ram pressure varies with the mass ratio of the merging galaxies, we rewrite Equation 3.1 using the surface densities in our galaxy models (see Chapter 2; Mo et al., 1998):

$$P_{\text{ram}} > \frac{Gf_g(1-f_g)M_d^2}{2\pi R_d^4} e^{-2R/R_d} \propto M_d^{2/3} e^{-2R/R_d} \quad (3.2)$$

Here  $f_g$  is the gas fraction of the secondary galaxy,  $M_d$  is the secondary disk's mass, and  $R_d$  is the scale radius of the disk. As the mass ratio of the merger decreases, the mass of the secondary's disk,  $M_d$ , is lower and a given  $P_{\text{ram}}$  strips the secondary down to a smaller radius. This is primarily because the stellar and gaseous surface densities of the secondary decrease as the mass of the galaxy decreases, leaving it less resistant to ram pressure.

In the 1:4 prograde coplanar merger, the primary galaxy's disk is relatively unaffected by ram pressure from the secondary galaxy, whereas the outskirts of the secondary are strongly stripped (see Figure 3.2 for a map of the gas density following second pericenter). Gaseous inflows increase the central surface density of the secondary by a factor of five or more, helping the central gas to survive the interaction with the primary. Immediately following second pericenter,  $\simeq 45$  percent of the gas in the central 100 pc of the secondary originated in the disk of the primary, suggesting that the secondary efficiently captures gas during the collision. While the low density gas in the outskirts of the secondary is stripped, forming a bridge between the galaxies, the dense central gas survives the encounter and captures gas as it plows through the primary. We also see evidence of compression in the central gas of the secondary due to ram pressure during and immediately following the second pericenter passage. The pressure of the nuclear gas ( $P = \frac{k}{\mu m_u} \rho T$ ) increases by three orders of magnitude, reaching a value corresponding to  $P_{\text{ram}}$  from cold, dense gas in the primary disk ( $\rho \simeq 10^3 - 10^4 \text{ amu cm}^{-3}$ ;  $v = 500 \text{ km s}^{-1}$  at second pericenter). Numerous simulations of ram pressure from a hot, low density medium have suggested that it can enhance star formation in the disk and wake of the stripped galaxy (Evrard, 1991; Vollmer et al., 2001; Kronberger et al., 2008; Kapferer et al., 2009).

We note that the effects of ram pressure will be maximized for our coplanar mergers, where both gaseous disks must pass completely through each other. The rotation of the galaxies can also increase the impact of ram pressure if the galaxies rotate into the collisional interface, increasing the velocity  $v$  in  $P_{\text{ram}} = \rho v^2$  (see our retrograde coplanar mergers in Section 3.3.2).

### 3.2.3 Star Formation Driven by Angular Momentum Loss

We follow here the star formation in each galaxy, focusing on nuclear star formation that is fueled primarily by inflowing gas from kpc scales. The strongest gaseous inflows and corresponding bursts of star formation occur during pericenter passages, when tidal torques between the galaxies are strongest. At first pericenter, however, the presence of a bulge stabilizes the galaxies and there are no inflows nor any enhancement in star formation (middle panel of Fig. 3.1). Instead, the galaxies evolve quiescently until the second pericenter passage at  $t \simeq 1.2$  Gyr. The global star formation rate decreases initially as the galaxies continue to settle from the initial conditions (see Chapter 2). Once the galaxies have settled, the star formation rate gradually falls as gas is depleted through star formation. During this initial, quiescent phase of the merger, the nuclear star formation rate in each galaxy is low, remaining at approximately two orders of magnitude less than the global star formation rate.

At second pericenter, tidal torques remove angular momentum from the gas in the secondary galaxy, driving inflows and building up a high central gas density. The gas disks collide, unlike at first pericenter where there is a fly-by encounter. As the disks collide, the collisionless stars pass through each other, but the gas is shocked and dissipates its orbital energy. Fig. 3.2 shows a snapshot of the gas densities just after second pericenter. The collision causes much of the gas in the secondary galaxy to lag behind the stellar component in the form of a gaseous bridge. This bridge contains significant cold gas and hosts moderate star formation, in agreement with observations of molecular gas in bridges resulting from disk collisions (Braine et al., 2004; Lisenfeld et al., 2008; Vollmer et al., 2012). The high density gas in the center of the secondary galaxy survives the encounter and is compressed due to ram pressure

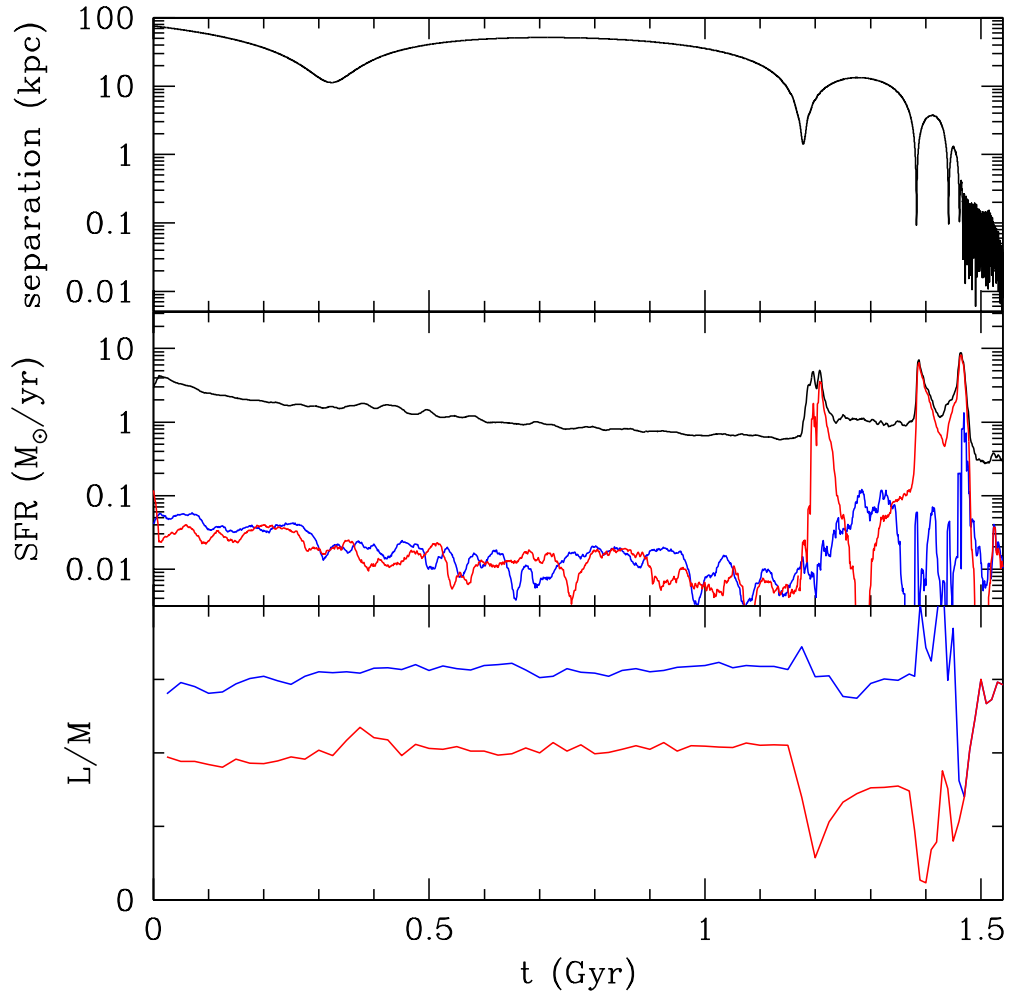


**Figure 3.1.** Results of the 1:4 coplanar simulation. Top panel: separation between the central black holes in each galaxy as a function of time. Middle panel: Star formation rates as a function of time. The global star formation rate across both galaxies is shown in black. The rates in the central 100 pc of each galaxy are shown in blue and red for the primary and secondary, respectively. Bottom panel: angular momentum per unit mass of gas in the central kpc of each galaxy in blue and red for the primary and secondary, respectively.

during the collision, forming a small (radius  $\simeq 100$  pc) clump of star forming gas.

The dense central clump of gas in the secondary galaxy hosts a burst of star formation following second pericenter, reaching a rate of  $4.4 M_{\odot} \text{ yr}^{-1}$  which is a five hundred fold increase over the quiescent central star formation rate of  $\simeq 0.01 M_{\odot} \text{ yr}^{-1}$ . At its peak, the central 100 pc of the secondary galaxy is hosting  $\simeq 80$  percent of the global star formation compared to one percent of the global rate previously, showing how effectively the close encounter has concentrated the gas there. The starburst lasts  $\simeq 25$  Myr before supernova feedback halts any further star formation. The primary galaxy, on the other hand, experiences weak inflows immediately following second pericenter and shows no significant increase in star formation.

As the galaxies separate and approach apocenter, the primary galaxy develops a weak bar instability. The bar funnels gas into the center of the galaxy, but the overall loss of angular momentum is small and the nuclear star formation is far weaker than that of the secondary at second pericenter. Meanwhile, the secondary reforms a small (radius  $\simeq 800$  pc) gaseous disk from gas in the bridge and tidal features, including a significant amount of gas that originally resided in the primary galaxy. We note that the new disk forms with the opposite angular momentum of the previous one, turning the third pericenter passage into a prograde-retrograde encounter.

At third pericenter, angular momentum loss drives further gaseous inflows in the secondary galaxy's gas. The central regions are again compressed during the collision with the more massive and extended gaseous disk of the primary galaxy. This compression increases the density of the central gas, driving another burst of star formation in the secondary. The nuclear star formation rate in the central 100 pc reaches  $7.7 M_{\odot} \text{ yr}^{-1}$ , with 92 percent of the global star formation occurring there during the burst. As at second pericenter, the response of the primary galaxy is far weaker and there is no significant gaseous inflow or star formation.

During the remainder of the merger, the secondary galaxy does not leave the disk of the primary. The remaining pericenter passages occur much more quickly than the early passages, leaving little time for the secondary galaxy to reform a dense gaseous disk. The central star formation rate in the secondary remains high at  $> 0.5$

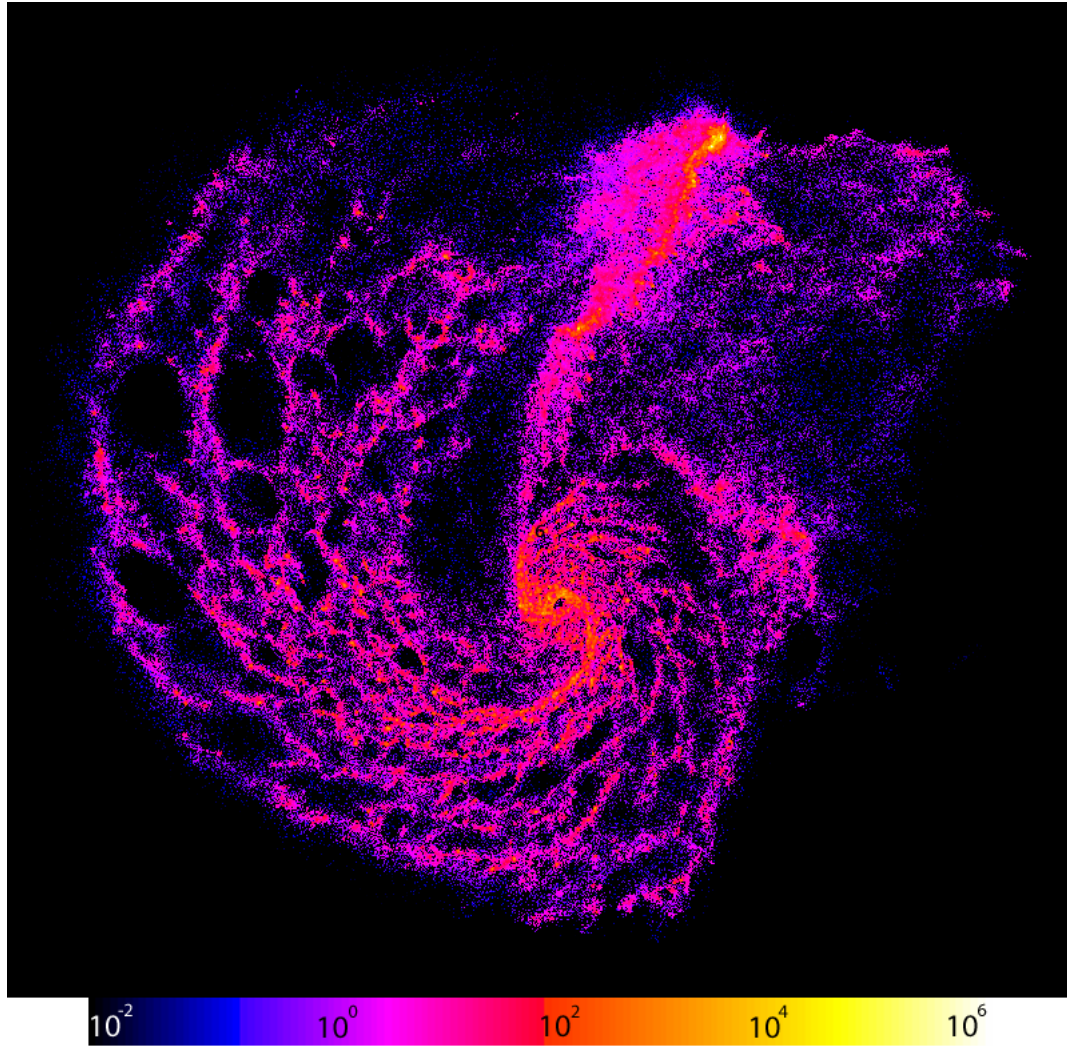


**Figure 3.2.** Gas density snapshot in the 1:4 prograde coplanar merger at  $t = 1.2$  Gyr, just following the second pericenter passage. The primary galaxy is at the bottom and the secondary galaxy is at the top. The distance between the centers of the two galaxies is 6.3 kpc. The colorbar shows the gas density scale (logarithmic) in units of  $\text{amu cm}^{-3}$ .

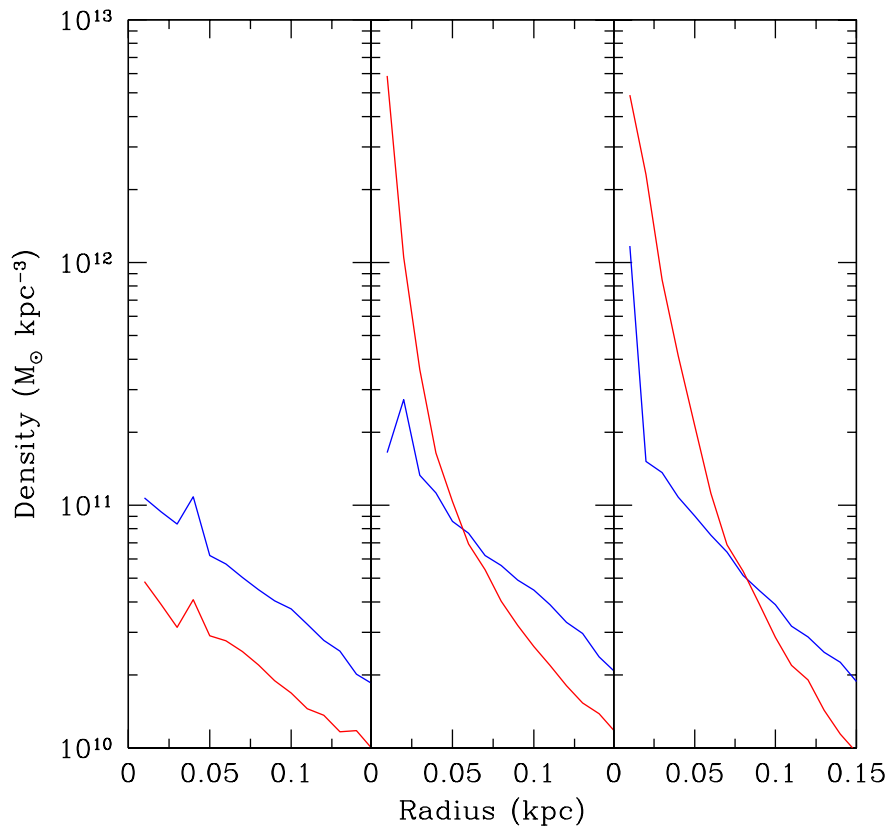


**Figure 3.3.** Total central density as a function of radius for the primary (blue) and secondary (red) galaxies in the 1:4 prograde coplanar merger. Left panel:  $t = 1$  Gyr, before second pericenter. Middle panel:  $t = 1.3$  Gyr, after second pericenter. Right panel:  $t = 1.42$  Gyr, after third pericenter. At each time,  $r = 0$  corresponds to the center of mass of the given galaxy.

$M_{\odot} \text{ yr}^{-1}$ , but there are no strong bursts at the fourth and fifth pericenter passages. The last peak of star formation occurs in the merger remnant following the sixth pericenter passage as the remaining gas in both galaxies engages in a starburst. This last starburst yields the highest star formation rates of the entire simulation, with the global rate reaching  $10.5 M_{\odot} \text{ yr}^{-1}$ , but it occurs after the stellar nuclei have merged and does not contribute to the formation of a pre-merger central cusp.

Fig. 3.3 shows the central density in each galaxy at three different times. The left panel shows  $t = 1$  Gyr, prior to the second pericenter, when neither galaxy has experienced any strong merger-driven star formation. At this time, the secondary galaxy is less dense than the primary, as was the case in the initial conditions. The



middle panel shows  $t = 1.3$  Gyr, near apocenter following the second pericenter. Both galaxies have built up a denser central cusp through new star formation, but the nuclear starburst in the secondary at second pericenter has left the secondary galaxy's nucleus significantly denser. The right panel shows the density profiles at  $t = 1.42$  Gyr, after third pericenter, when the majority of the central star formation in both galaxies is complete. After continued strong star formation following the third pericenter, the secondary galaxy remains denser on small scales,  $r \leq 75$  pc. Note that the spike in central density in the primary galaxy in the right panel is due to the massive BH sitting atop the center of mass and inflating the density in the central bin.

We note that not all star formation that contributes to the build up of the nuclear cusp is local. Even during pericenter passages, there is a significant amount of star formation outside the nuclei. The off-center gas participating in the starbursts tends to be dense and clumped, yielding clusters of new stars. Some of these clusters will sink to the center of the nuclei under the effects of dynamical friction and contribute to the nuclear stellar population.

Efficient nuclear star formation in the secondary galaxy yields a stellar cusp that is denser than that of the primary galaxy. The additional mass in new stars ensures the survival of the nucleus down to small scales in the primary galaxy, aiding in the formation of a BH pair. To understand the continued evolution of the predominantly stellar nuclei as they merge, we consider the effects of tidal stripping and tidal heating and determine whether they can account for the behavior seen in our simulations.

### 3.2.4 Tidal Stripping

In a slow encounter between the two galaxies, the static tidal field produced can remove material from each galaxy outside a limiting tidal radius  $r_t$ . Observationally, the effects of tidal stripping are commonly seen in globular clusters and dwarf galaxies (e.g. King, 1962). For a satellite system on a circular orbit, the tidal radius is given by:

$$r_t^3 = \frac{Gm(< r_t)}{\omega^2 + G\left[\frac{2M(< r)}{r^3} - 4\pi\rho(r)\right]}. \quad (3.3)$$

Here  $m$  and  $M$  are the masses of the satellite and host systems, respectively,  $\omega$  is the instantaneous angular velocity of the satellite,  $r$  is the radius of the circular orbit of the satellite, and  $\rho(r)$  is the local density of the host. We note that the galaxies in the mergers presented here are not on circular orbits, but equation 3.3 provides an approximation of the true tidal radius, which is not spherical and depends on the orbits of the stars in the satellite (Read et al., 2006; Binney & Tremaine, 2008).

The natural timescale for tidal stripping is the orbital timescale of the satellite at the tidal radius. The tidal fields of the galaxies are important on large scales for mass loss, particularly for the gaseous bridge that links the disks following second pericenter. The secondary galaxy can only reform its disk from gas that remains bound following the disk collision. On small scales, the stellar nuclei are unaffected by tidal stripping. The pericenter passages last an order of magnitude less than the relevant orbital timescales, suggesting that there is insufficient time for tidal stripping to act on the nuclei. During the late stages of the merger, we instead consider the impact of fast encounters through tidal shocks.

### 3.2.5 Tidal Heating

During a close encounter between the merging nuclei, rapidly varying gravitational fields inject energy into the systems. These gravitational shocks can lower the central density by redistributing mass to larger radii or completely unbinding material (Ostriker et al., 1972; Spitzer, 1987; Gnedin et al., 1999; Taylor & Babul, 2001). Unlike tidal stripping, which operates on the orbital timescale of the material being stripped, tidal heating can inject energy even during very fast encounters.

During a fast encounter between a perturbing system of mass  $M_p$  and a shocked system of mass  $M_s$  with relative velocity  $V$ , the total energy injected into the shocked system is given by (Binney & Tremaine, 2008):

$$\Delta E_s = \frac{4G^2 M_p^2 M_s}{3V^2 b^4} U(b/r_h) \langle r^2 \rangle, \quad (3.4)$$

where  $b$  is the impact parameter of the encounter and  $\langle r^2 \rangle$  is the mass-weighted

mean square radius of particles in the shocked system.  $U(b/r_h)$  is a function that accounts for encounters where the two systems interpenetrate and the perturber cannot be approximated by a point mass.  $r_h$  represents the half-mass radius of the perturbing system. When the impact parameter is small compared to the the half-mass radius, the total energy injected is reduced. We use the values of  $U(b/r_h)$  given in Binney & Tremaine (2008), approximating the density profiles of the systems as Hernquist profiles (Hernquist, 1990).

We compare the energy injected through tidal heating to the binding energy of the nuclei. We estimate the binding energy,  $E_{bind}$ , as the energy required to move all the material in the nucleus to the edge of the nucleus,  $r_{nuc}$ . This does not represent the energy required to completely unbind the nuclear material from the potential well of the merged galaxy. It instead approximates the energy required to smooth out the most highly bound portions of the nucleus.  $E_{bind}$  is given by:

$$E_{bind} = \int_0^{r_{nuc}} 4\pi r'^2 \rho(r') [\phi(r_{nuc}) - \phi(r')] dr', \quad (3.5)$$

where  $\phi(r)$  is the gravitational potential of the shocked system at radius  $r$ .

Due to the strong dependence of the tidal heating on the impact parameter,  $b$ , the initial pericenter passages inject little energy into the nuclei compared to the total binding energy. The energy becomes important when the nuclei pass within  $r \leq 100$  pc with typical velocities of  $V \simeq 300 - 500$  km s<sup>-1</sup>. During these encounters, the energy injected from the companion nucleus can be greater than  $E_{bind}$ , causing the nucleus to be disrupted and leaving the central BH ‘naked’, without any bound gas or stars. A dense nucleus has a large binding energy that is resistant to tidal heating. Additionally, a dense, centrally concentrated nucleus has a large mass as a perturber and small half-mass radius  $r_h$ , increasing the energy injected into the other galaxy’s nucleus.

Following the third pericenter passage in the 1:4 merger, the secondary galaxy’s nucleus is significantly denser than the primary galaxy’s nucleus (Fig. 3.3). During the fourth and fifth pericenter passages, when the nuclei pass within  $\simeq 100$  pc of

each other, tidal shocks reduce the central density of the primary galaxy. At the sixth pericenter passage, the nuclei pass within  $\leq 29$  pc of each other with a relative velocity of  $415 \text{ km s}^{-1}$  and the primary galaxy's nucleus is unbound. The relatively less dense primary injects far less energy into the secondary nucleus, which survives the encounter intact. After disrupting the primary galaxy's nucleus, the secondary galaxy's nucleus is at the center of the merger remnant and is the site of the last and strongest burst of star formation of the merger. The primary BH, now without any bound stars or gas, is left on an elliptical orbit around the merger remnant with an apocenter of 200 pc.

### 3.2.6 Dynamical Friction

The disruption of the primary significantly delays the formation of a binary black hole system, since the dynamical friction timescale for a 'naked' black hole is significantly longer than for the original nucleus. Dynamical friction exerts a drag force on the BH, removing orbital energy and causing it to spiral in toward the center of the merger remnant. Dynamical friction also drives the orbital evolution of the galaxies themselves throughout the merger, causing the apocenter and pericenter of each passage to decrease over time.

As a satellite system (a galaxy or BH, in our case) moves through a homogeneous background consisting of small particles, the particles form a wake behind the satellite. The wake exerts a gravitational force (dynamical friction) on the satellite against the direction of motion, reducing its velocity. The change in velocity over time is given by:

$$\frac{dv_M}{dt} = -16\pi^2 G^2 M m \ln\Lambda \left[ \int_0^{v_M} v_m^2 f(v_m) dv_m \right] \frac{1}{v_M^2} \quad (3.6)$$

(Chandrasekhar, 1943; Binney & Tremaine, 2008). Here  $v_M$  is the velocity of a satellite of mass  $M$  moving through a background of smaller particles, each with mass  $m$ .  $f(v_m)$  is the distribution function of the background particles.  $\ln\Lambda$  is the Coulomb logarithm, which accounts for the range in impact parameters for particles encountering the satellite.

To estimate the time for a BH binary to form, we consider the effects of dynamical

friction acting on the primary BH as it moves through the merger remnant. The dynamical friction timescale gives the time for the orbit of the BH to decay and reach the center of the merged galaxy. We use the timescale from Colpi et al. (1999), who study the decay in the orbits of satellites in N-body simulations. They find that the orbital decay time is well fit by the function:

$$\tau_{\text{DF}} = 1.2 \frac{J_{\text{cir}} r_{\text{cir}}}{\left(\frac{GM_{\text{sat}}}{e}\right) \ln\left(\frac{M_{\text{halo}}}{M_{\text{sat}}}\right)} \epsilon^{0.4}. \quad (3.7)$$

$M_{\text{sat}}$  and  $M_{\text{halo}}$  are the masses of the satellite and halo, respectively.  $J_{\text{cir}}$  and  $r_{\text{cir}}$  are the orbital angular momentum and radius of a circular orbit with the same energy as the initial orbit of the satellite.  $\epsilon$  is the ratio of the angular momentum of the initial orbit to  $J_{\text{cir}}$ . This parameter accounts for the faster decay of elliptical orbit, which pass deeper into the halo and encounter higher background densities, increasing the force of dynamical friction.  $e$  accounts for mass loss from the satellite due to tidal stripping as the orbit decays. For the decay of rigid satellites such as BHs, we ignore  $e$ .

In determining  $\tau_{\text{DF}}$ , we first calculate the energy per unit mass of the orbit of the BH using  $E/M = 1/2v^2 + \Phi$ , where  $v$  is the velocity of the BH relative to the center of mass and  $\Phi$  is the gravitational potential per unit mass of the BH. We then move outward from the center of mass of the merger remnant until we find a circular orbit with the same energy. The angular momentum and radius of this orbit determine  $J_{\text{cir}}$ ,  $r_{\text{cir}}$ , and  $\epsilon$ . We set  $M_{\text{halo}}$  equal to the total mass enclosed within this circular orbit.

In the 1:4 prograde coplanar merger, the orbit of the primary BH after disruption has an initial apocenter of 230 pc. The circular orbit with the same energy has a radius of 151 pc. The eccentricity of the orbit, accounted for by the parameter  $\epsilon$ , reduces the orbital decay timescale by a factor of two. The resulting timescale is 23 Myr. Since Equation 3.7 depends inversely on the mass of the satellite body, the loss of the surrounding material from the BH increases the dynamical friction timescale, delaying the formation of a BH binary. We use Equation 3.7 to estimate the timescale

| Simulation                 | Global SFR<br>( $M_{\odot} \text{ yr}^{-1}$ ) | Primary SFR<br>( $M_{\odot} \text{ yr}^{-1}$ ) | Secondary SFR<br>( $M_{\odot} \text{ yr}^{-1}$ ) | Primary<br>Survival | Secondary<br>Survival | Binary Timescale<br>(Myr) |
|----------------------------|---|--|--|---------------------|-----------------------|---------------------------|
| <b>Prograde Coplanar</b>   |   |  |  |                     |                       |                           |
| 1:2                        | 18.9  | 1.77   | 3.63   | No                  | Yes                   | 13.2                      |
| 1:4                        | 8.3   | 0.19   | 7.65   | No                  | Yes                   | 23                        |
| 1:6                        | 4.35  | 0.06   | 3.78   | No                  | Yes                   | 17.4                      |
| 1:10                       | 1.1   | 0.12   | 0.73   | Yes                 | No                    | 92                        |
| <b>Inclined</b>            |   |  |  |                     |                       |                           |
| 1:2                        | 9.44  | 1.82   | 8.9  | No                  | Yes                   | 18.3                      |
| 1:4                        | 1.96  | 0.28   | 0.32   | Yes                 | No                    | 660                       |
| <b>Retrograde Coplanar</b> |   |  |  |                     |                       |                           |
| 1:2 (Prim.)                | 11.4  | 3.49   | 2.34   | No                  | No                    | <8.3                      |
| 1:2 (Sec.)                 | 26.9  | 4.8  | 0.93   | Yes                 | No                    | 223                       |

**Table 3.1.** Peak star formation rates and results of the nuclear merger. Star formation rates are expressed in units of  $M_{\odot} \text{ yr}^{-1}$  and are the peak rates between the first pericenter passage and the merger of the nuclei. Peak rates for each galaxy are star formation rates within the central 100 pc. The binary timescale is estimated using Equation 3.7 from Colpi et al. (1999) from the time of disruption of the primary and/or secondary nucleus.

following disruption because the effects of dynamical friction in our simulations may be underestimated on a lone BH due to gravitational softening on small scales.

### 3.3 Results

#### 3.3.1 Impact of Mass Ratio

In this section, we compare the results of the prograde coplanar mergers (mass ratios 1:2, 1:4, 1:6, and 1:10), focusing on the merger triggered star formation, the build-up of a central cusp, and the outcome of the nuclear merger. Figures 3.4, 3.5, and 3.6 show the evolution of these mergers. We find that the secondary is able to form a dense central cusp and disrupt the primary galaxy’s nucleus in the 1:2, 1:4, and 1:6 prograde coplanar mergers, but not in our 1:10 merger. The formation of a dense cusp depends on the strength of gaseous inflows and the ability of the secondary galaxy’s gas to survive direct collisions with the primary galaxy’s disk. The strongest nuclear star formation occurs in the secondary in our 1:4 run, then becomes weaker as the mass ratio decreases and the secondary loses more gas to ram pressure stripping from the primary. In the following, we discuss the detailed findings.

**Primary Galaxy** As the mass ratio of the merger decreases, the primary galaxy experiences weaker tidal torques due to the relatively less massive secondary galaxy. The result is a more limited loss of angular momentum, down to no loss at all in the

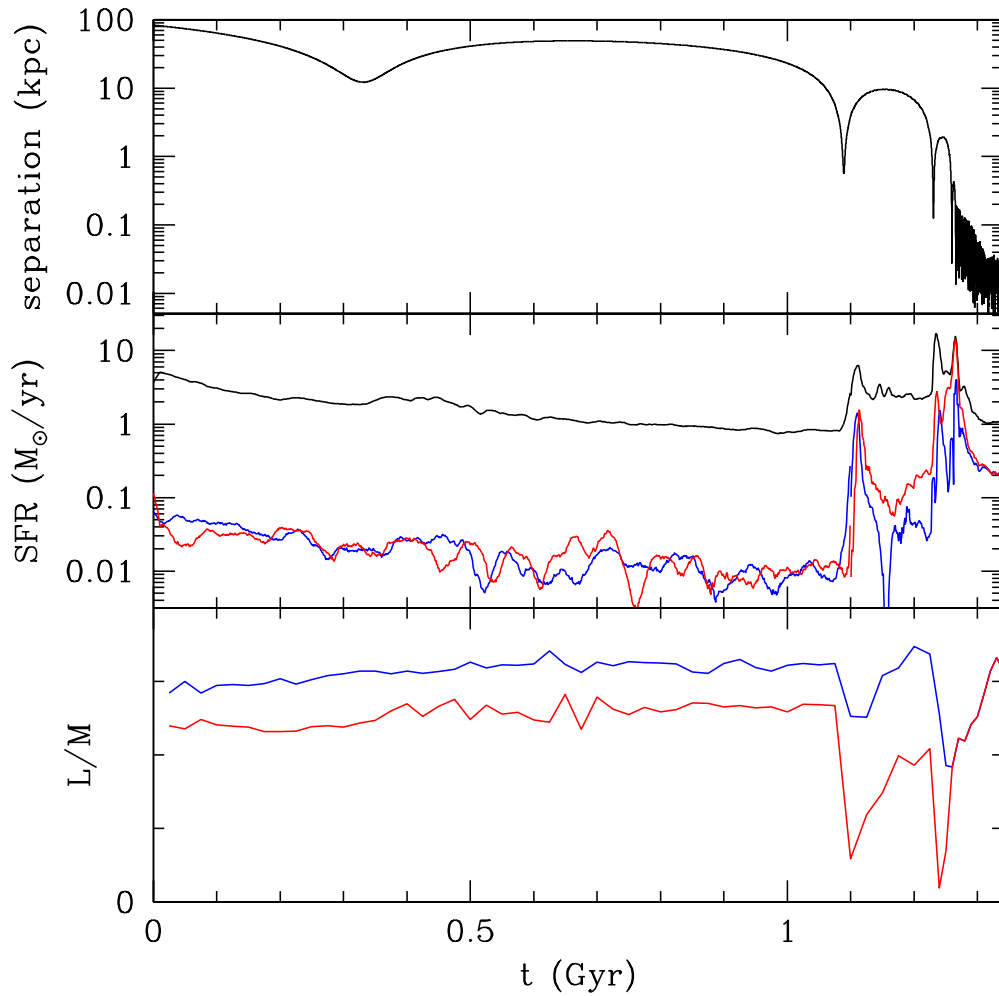


**Figure 3.4.** Results of the 1:2 coplanar simulation. Top panel: separation between the central black holes in each galaxy as a function of time. Middle panel: Star formation rates as a function of time. The global star formation rate across both galaxies is shown in black. The rates in the central 100 pc of each galaxy are shown in blue and red for the primary and secondary, respectively. Bottom panel: angular momentum per unit mass of gas in the central kpc of each galaxy in blue and red for the primary and secondary, respectively.

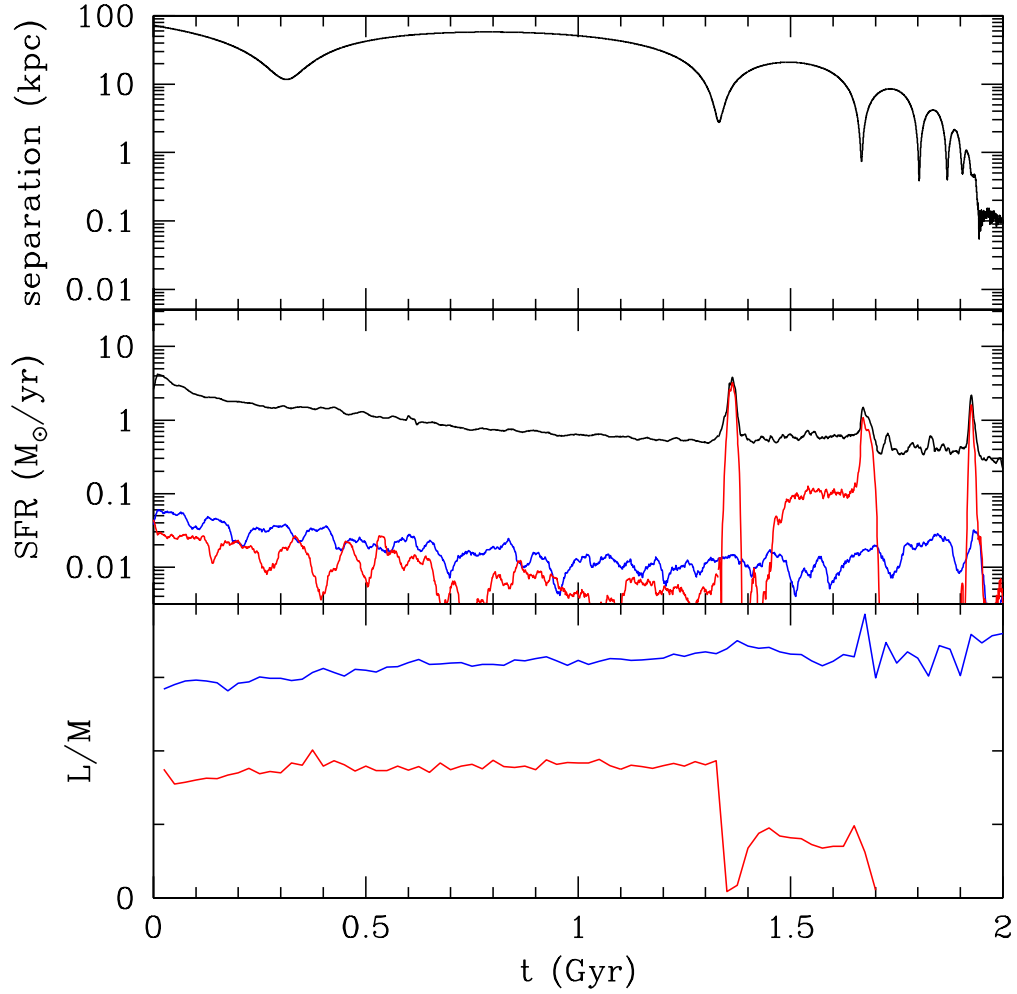


**Figure 3.5.** Results of the 1:6 coplanar simulation. Top panel: separation between the central black holes in each galaxy as a function of time. Middle panel: Star formation rates as a function of time. The global star formation rate across both galaxies is shown in black. The rates in the central 100 pc of each galaxy are shown in blue and red for the primary and secondary, respectively. Bottom panel: angular momentum per unit mass of gas in the central kpc of each galaxy in blue and red for the primary and secondary, respectively.



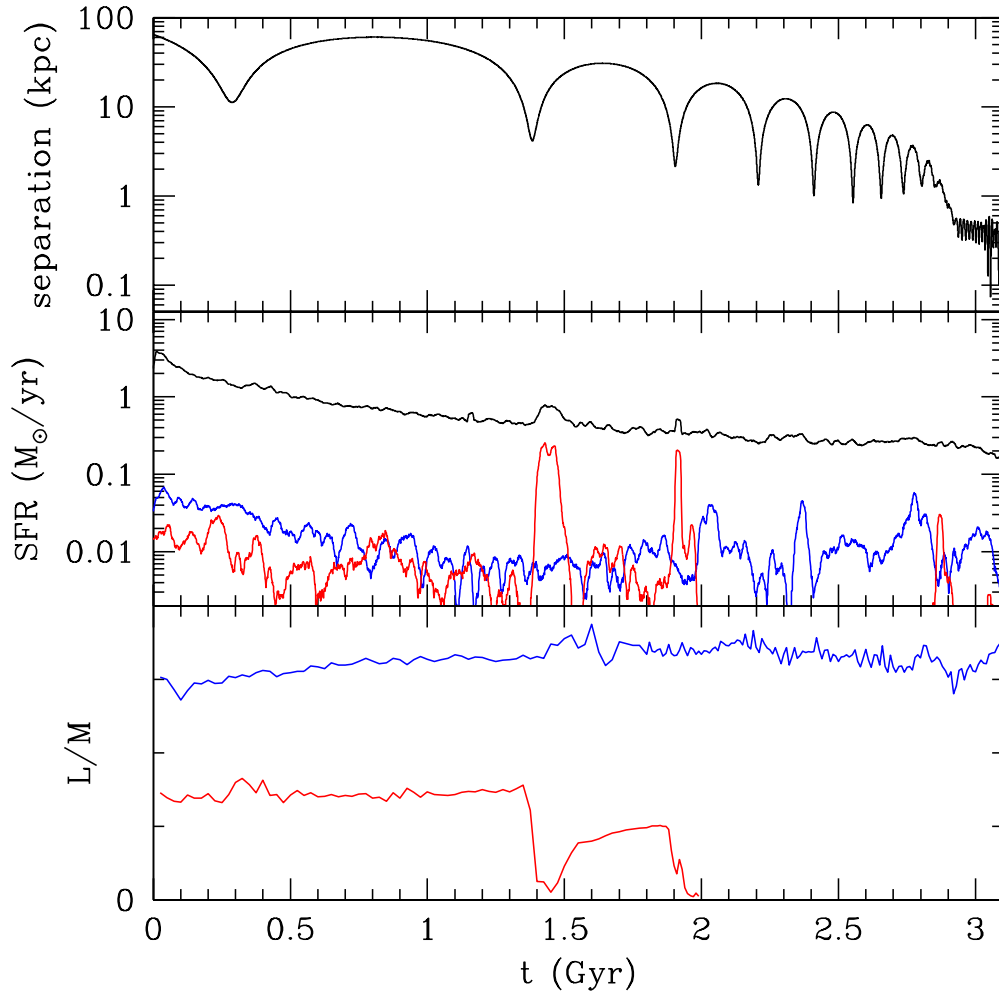


**Figure 3.6.** Results of the 1:10 coplanar simulation. Top panel: separation between the central black holes in each galaxy as a function of time. Middle panel: Star formation rates as a function of time. The global star formation rate across both galaxies is shown in black. The rates in the central 100 pc of each galaxy are shown in blue and red for the primary and secondary, respectively. Bottom panel: angular momentum per unit mass of gas in the central kpc of each galaxy in blue and red for the primary and secondary, respectively.

smallest mass ratios, and a lack of strong merger-induced star formation. The top left panel of Fig. 3.7 shows the cumulative mass in new stars formed in the central 100 pc of the primary galaxy in each prograde coplanar merger. The primary shows a strong central burst of star formation at second and third pericenter in the 1:2 merger and a weaker enhancement following second pericenter in the 1:4 merger, driven by a weak bar, but no response in the 1:6 and 1:10 runs. The peak nuclear star formation rate prior to the merger of the nuclei is shown in Table 3.1 for each run. The global peak star formation decreases with mass ratio, as does the peak response of the primary down to a minimum peak rate of 0.1-0.2  $M_{\odot}$ .

**Secondary Galaxy** The tidal response of the secondary galaxy, on the other hand, grows stronger as the mass ratio decreases and the primary galaxy becomes relatively more massive. This leads to stronger inflows, but strong nuclear star formation depends on dense central gas surviving the collision between the gaseous disks. Fig. 3.5 and 3.6 show that the strongest loss of angular momentum at second pericenter occurs in the 1:6 and 1:10 mergers. However, as the gas mass and density of the secondary disk decreases, it is more strongly affected by ram pressure from the primary's disk, and the mass of the dense star forming clump generally decreases with mass ratio. The exception is the 1:2 and 1:4 runs, where the total mass in central gas that survives the disk interaction is similar. In the 1:4 run, however, the gas is more strongly compressed during the disk collision. The gas therefore reaches higher densities and fuels a stronger burst of star formation.

**1:2 Merger** As a result of the strong burst of star formation in both the primary and secondary at second pericenter in the 1:2 merger (Fig. 3.4), the nuclei have similar central densities. Stronger angular momentum loss and inflows in the secondary at third pericenter fuel a large increase in central mass over the primary nucleus. Additionally, a dense star cluster forms  $\simeq 400$  pc away from the secondary nucleus in the gas bridge resulting from the third pericenter passage. This cluster merges with the secondary nucleus shortly before the two nuclei merge, further increasing the central density. As in the 1:4 merger, the primary galaxy's nucleus is completely disrupted due to tidal heating from the secondary nucleus during the fourth and fifth

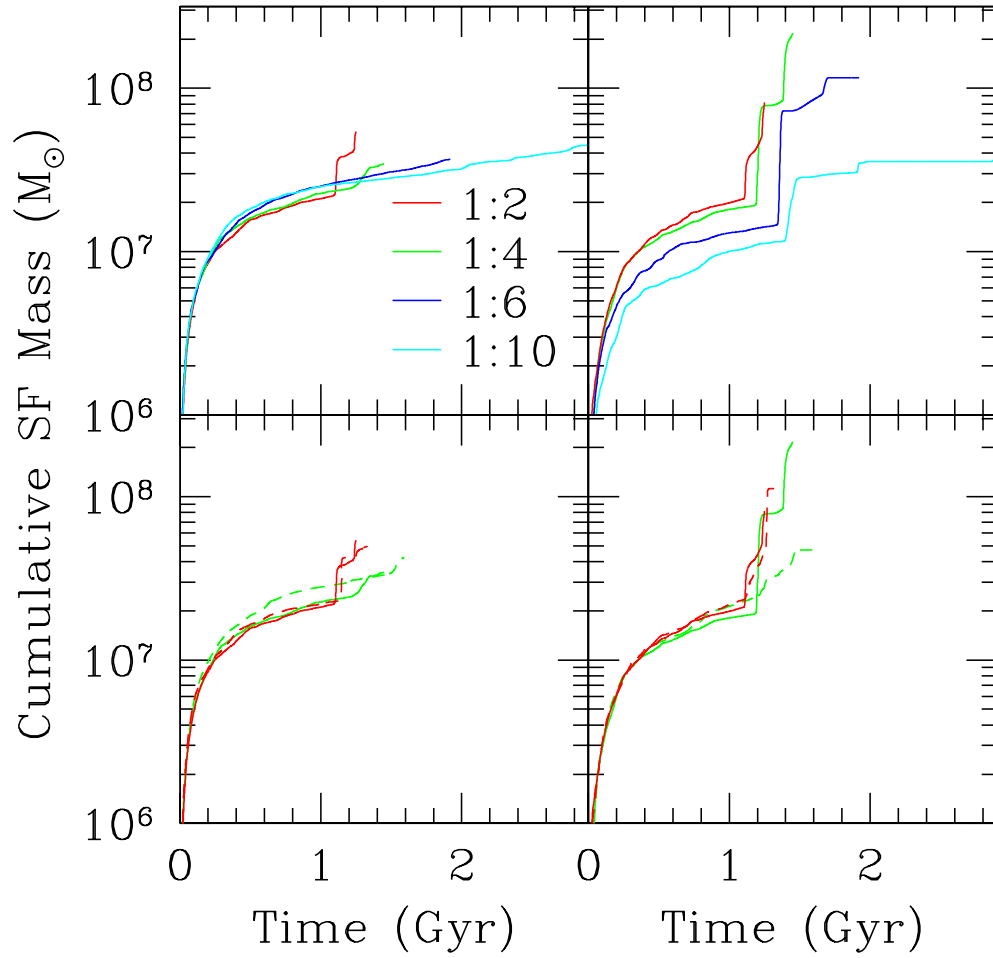


**Figure 3.7.** Cumulative mass in new star formation in the central 100 pc of each galaxy. Top panels: coplanar prograde mergers. Bottom panels: coplanar (solid) and inclined (dashed) mergers. Left panels: primary galaxy. Right panels: secondary galaxy.

pericenter passages.

**1:6 Merger** In the 1:6 merger, the secondary’s disk is strongly affected by ram pressure from the primary’s disk. This limits the amount of cold, dense gas available for star formation. At third pericenter, ram pressure removes the majority of the gas. Supernova feedback then expels the remaining gas, leaving the secondary completely gas poor. The remaining evolution is slower than in the 1:2 and 1:4 mergers, resulting in more pericenter passages before the nuclei merge. Tidal heating reduces the central mass and density of the secondary during these passages while the primary’s nucleus remains intact. Eventually, the secondary galaxy’s orbit circularizes within the disk of the primary galaxy, then plunges inward toward the primary’s nucleus. Despite the effects of tidal heating, the secondary galaxy’s nucleus remains significantly denser than the primary’s nucleus. The primary is disrupted during the plunge when the nuclei pass within  $\leq 55$  pc of each other. The primary BH is left on a circular orbit around the merger remnant with a radius of  $\simeq 100$  pc.

**1:10 Merger** The 1:10 merger proceeds similarly to the 1:6 merger. The secondary galaxy loses its gas to ram pressure following the third pericenter passage and experiences the weakest star formation of the prograde mergers. When the orbit of the secondary galaxy circularizes within the primary’s disk, the secondary galaxy is only denser than the primary on scales of  $\simeq 15 - 20$  pc. Despite the lack of significant merger induced star formation in the primary galaxy, the secondary galaxy is unable to build up enough central mass to survive the merger. During the plunge (passing within  $\simeq 400$  pc of the center of the primary), the secondary nucleus is disrupted down to its dense central cusp which has a total mass of  $10^7 M_{\odot}$ , an order of magnitude more than the mass of the secondary BH. The cusp survives the remainder of the merger on an elliptical orbit around the primary with an apocenter of  $\simeq 550$  pc. It is not dense enough, however, to survive a direct encounter with the primary nucleus. Using Equations 3.4 and 3.5, we estimate that the secondary’s cusp would be completely disrupted upon passing within  $\simeq 30$  pc of the center of the primary galaxy.

### 3.3.2 Impact of Orbital Parameters

#### Inclined Orbits

We summarize here the results of our inclined mergers (mass ratios 1:2 and 1:4), in which the disk of the primary galaxy is tilted 45 degrees with respect to the orbital plane. The secondary galaxy's disk is unchanged compared to the prograde coplanar mergers. In the inclined mergers, the secondary feels weaker tidal torques from the primary during the second pericenter passage than in coplanar mergers, resulting in only a weak enhancement in the central star formation rate. Instead of a burst, we see sustained star formation at an order of magnitude higher star formation rate than during the early quiescent phase of the merger. This enhancement is fed by low angular momentum gas, previously stripped from both galaxies during the second pericenter passage, which now reforms the disk of the secondary galaxy. The main increase in central mass in the secondary occurs during third pericenter, when the reformed disk is compressed by the ram pressure of the primary's disk. As the mass ratio of the merger decreases, the reformed disk is less massive and is strongly stripped during the third pericenter passage, preventing the secondary from efficiently forming stars and building a dense central cusp.

**1:2 Inclined Merger** Fig. 3.8 shows the evolution of the 1:2 inclined merger. The results of the simulation are very similar to the results of the prograde coplanar run. At second pericenter, the angle between the disks of the galaxies produces a weaker tidal torque on the secondary disk than in the coplanar case, leading to a smaller reduction in angular momentum and no significant burst of star formation. Instead, the secondary experiences sustained nuclear star formation at a rate of 0.1-0.2  $M_{\odot} \text{ yr}^{-1}$  until third pericenter, fed by low angular momentum gas falling back into the nucleus after being stripped during the interaction with the primary's disk. The resulting reformed disk is less massive than the reformed disk in the coplanar merger, but is smaller and denser. As a result, it is strongly compressed during the third pericenter passage and hosts a nuclear starburst reaching 8.9  $M_{\odot} \text{ yr}^{-1}$ , higher than in the coplanar merger. During the fifth and sixth pericenter passages, the primary

nucleus is disrupted by the secondary.

**1:4 Inclined Merger** As in the 1:2 inclined merger, weak angular momentum loss and gaseous inflows lead to little enhancement in star formation at second pericenter in the 1:4 inclined merger (Fig. 3.9). The secondary galaxy’s gas disk, strongly stripped during the encounter with the primary’s disk, reforms with predominantly low angular momentum material, leading to a slow reduction in the average angular momentum of gas in the central kpc (bottom panel of Fig. 3.9). This low angular momentum gas fuels nuclear star formation, but the star formation rate remains low and it does not contribute significantly to the formation of a dense central cusp. The reformed disk is significantly less massive and dense than the reformed disk in the 1:2 inclined merger. As a result, much of the disk is stripped due to ram pressure during the third apocenter. The remaining gas is compressed and efficiently forms stars, but the star formation rate remains low and there is again no significant increase in central density in the secondary. Supernova feedback removes the rest of the gas following third apocenter. During subsequent pericenter passages, the central density of the secondary decreases due energy injection from tidal shocks. At sixth pericenter, the secondary nucleus is disrupted by the primary nucleus, which survives the encounter. The secondary BH orbits the merger remnant on an elliptical orbit with an apocenter of 750 pc.

The bottom panels of Figure 3.7 show a comparison in the cumulative nuclear star formation between the coplanar and inclined mergers. The total star formation in the 1:2 mergers is very similar despite the change in inclination, although we note that the triggering of the star formation is different, as discussed above. The inclination plays a much larger role in the secondary in the 1:4 mergers (solid vs. dashed green lines, bottom right panel), where there is almost an order of magnitude difference in the cumulative star formation between the mergers. This shows why the secondary is unable to develop the dense central cusp necessary to disrupt the primary galaxy in the 1:4 inclined case.

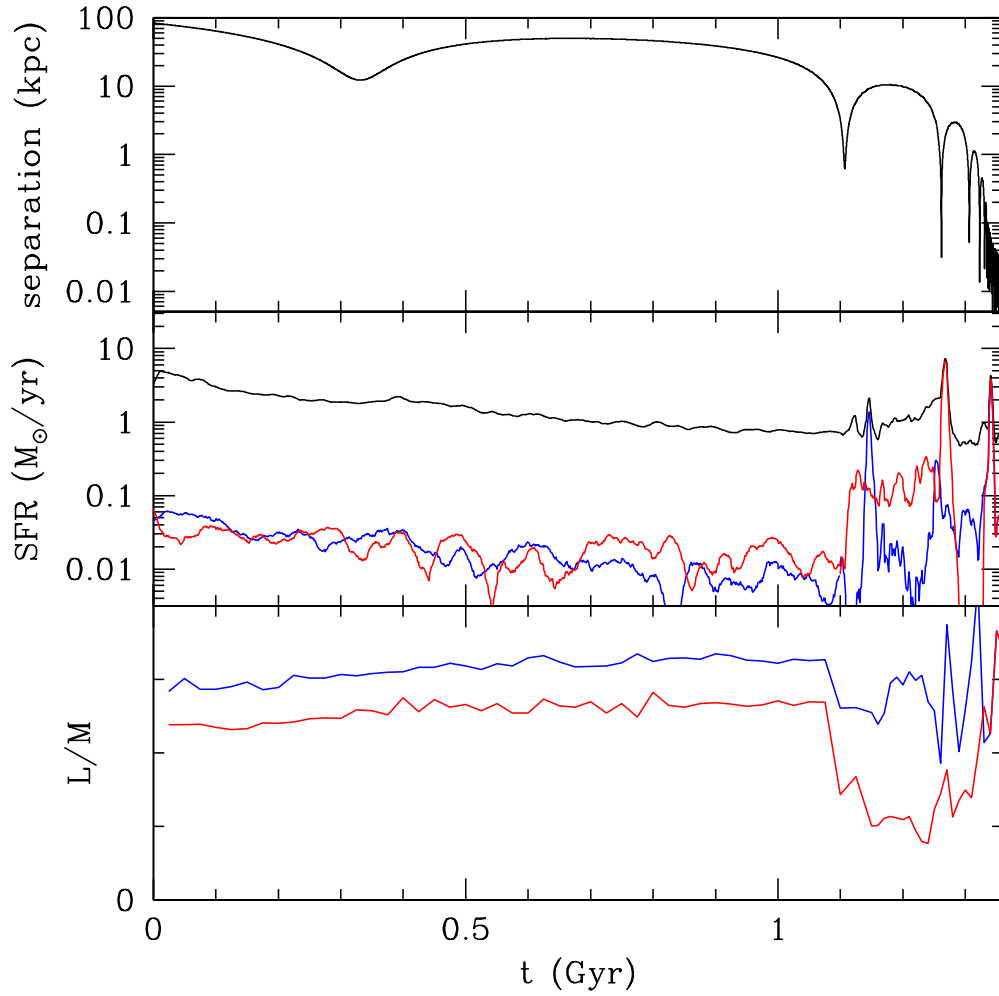


**Figure 3.8.** Results of the 1:2 inclined simulation. Top panel: separation between the central black holes in each galaxy as a function of time. Middle panel: Star formation rates as a function of time. The global star formation rate across both galaxies is shown in black. The rates in the central 100 pc of each galaxy are shown in blue and red for the primary and secondary, respectively. Bottom panel: angular momentum per unit mass of gas in the central kpc of each galaxy in blue and red for the primary and secondary, respectively.

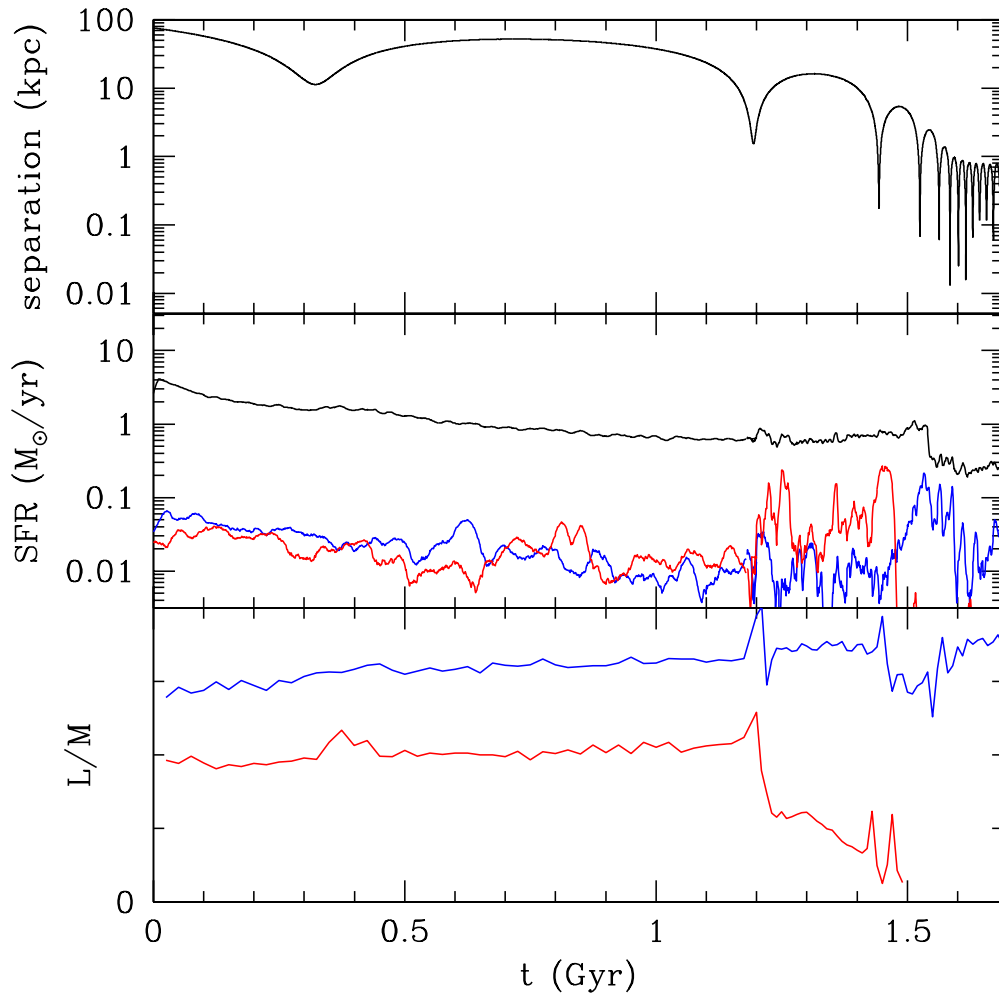


**Figure 3.9.** Results of the 1:4 inclined simulation. Top panel: separation between the central black holes in each galaxy as a function of time. Middle panel: Star formation rates as a function of time. The global star formation rate across both galaxies is shown in black. The rates in the central 100 pc of each galaxy are shown in blue and red for the primary and secondary, respectively. Bottom panel: angular momentum per unit mass of gas in the central kpc of each galaxy in blue and red for the primary and secondary, respectively.



## Retrograde Orbits

We also consider coplanar mergers that are retrograde, where the spin axes of the two galaxies have the opposite direction. Both of the mergers we consider here are 1:2. The retrograde (primary) run is similar in setup to the 1:2 prograde coplanar merger, except the spin axis of the primary galaxy has been flipped with respect to the orbital angular momentum vector of the galaxies. In the retrograde (secondary) merger, the spin axis of the secondary galaxy has been flipped. The retrograde orbits lead to stronger ram pressure in the disk interaction compared to the prograde mergers because both galaxies rotate into the collision. The stronger interaction produces high nuclear star formation rates in the primary galaxy, making it more difficult for the secondary galaxy to build a denser central cusp. In the retrograde (primary) run, the secondary sustains enough star formation to become similarly dense to the primary, causing both nuclei to be disrupted late in the merger. The formation of a massive bridge in the retrograde (secondary) merger prevents the secondary from reforming a significant gaseous disk after second pericenter. The secondary therefore remains less dense than the primary and is disrupted by tidal shocks.

**Retrograde (Primary) Merger** The secondary galaxy in the retrograde (primary) merger evolves similarly to the secondary in the 1:2 prograde merger. Strong inflows at second pericenter and compression during the disk interaction produces a high central gas density, leading to a nuclear starburst (Fig. 3.10). After the second pericenter passage, supernova feedback heats the gas, preventing further strong star formation as the secondary's gaseous disk reforms. At third pericenter, the gas is again compressed, producing another starburst that increases the central mass and density of the secondary nucleus. The primary does not experience a strong starburst following second pericenter, but forms a strong bar following the encounter, which is not present in the prograde merger. The bar funnels gas into the center of the primary, leading to a higher sustained nuclear star formation rate than in the secondary near apocenter. The result of this nuclear star formation is that both nuclei are similarly dense when they merge. During the fifth pericenter passage, when the nuclei pass within 11 pc of each other, tidal heating unbinds both nuclei. The central

BHs of both galaxies are left orbiting around the merger remnant, which is largely made up of new stars that formed in the final starburst.

**Retrograde (Secondary) Merger** The prograde-retrograde interaction between the disks in these mergers leads to a strong shock in the disk gas. The leading edge of each galaxy is rotating into the disk collision, increasing the relative velocity of the impact. This shocked gas forms a massive bridge between the galaxies as they approach apocenter following the second pericenter passage. In the retrograde (primary) merger, this shocked gas passes around the nucleus of the primary galaxy. In the retrograde (secondary) merger, however, the shocked gas passes directly through the primary nucleus, strongly compressing the central gas there. This interaction leads to the strongest global star formation rate in any of the mergers presented here, peaking at  $26.9 M_{\odot} \text{ yr}^{-1}$ . Much of this star formation occurs in the massive bridge that links the galaxies, but the central star formation in the primary is higher than in the secondary (Fig. 3.11). Fig. 3.12 shows a snapshot of the gas density following second pericenter. Compared to the gas distribution in the 1:4 prograde coplanar merger (Fig. 3.2), both disks have been more strongly disrupted by the collision and much more gas is concentrated in the bridge between the galaxies. The strong star formation in the gaseous bridge and following supernova feedback prevents the gas from reforming the secondary galaxy’s disk. The secondary’s disk therefore remains low in mass and hosts little star formation during the third pericenter passage. The primary nucleus sustains a consistently higher star formation rate than the secondary nucleus and remains denser. At fourth pericenter, the secondary is disrupted during a close encounter with the primary nucleus. The secondary BH is left on an elliptical orbit around the primary with an apocenter of  $\simeq 650 \text{ pc}$ .

### 3.4 Discussion

Our results show that the primary galaxy can be disrupted in a variety of mass ratios if the disks are coplanar and prograde. However, this orientation maximizes the tidal response of the disk and the strength of the following starburst (Mihos & Hernquist, 1996; Cox et al., 2008). Indeed, our inclined mergers produce weaker starbursts. As

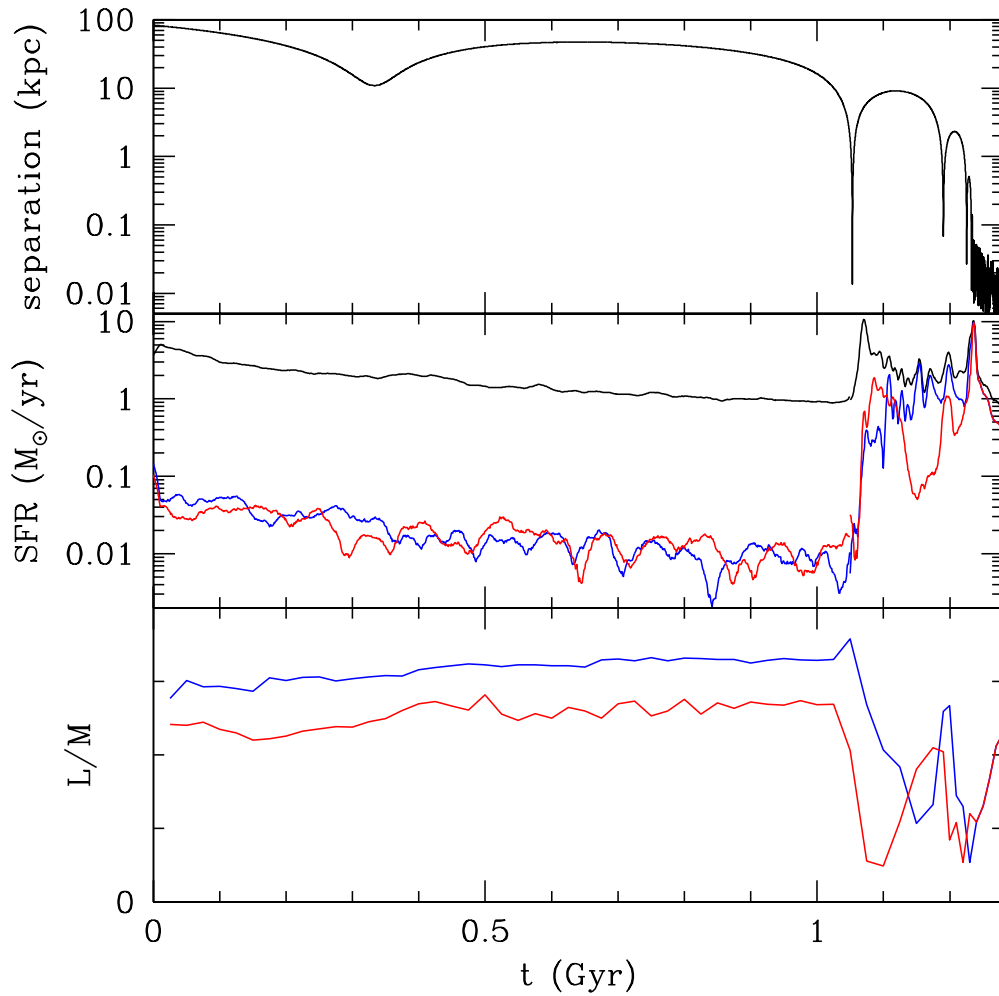


**Figure 3.10.** Results of the 1:2 retrograde (primary) simulation. Top panel: separation between the central black holes in each galaxy as a function of time. Middle panel: Star formation rates as a function of time. The global star formation rate across both galaxies is shown in black. The rates in the central 100 pc of each galaxy are shown in blue and red for the primary and secondary, respectively. Bottom panel: angular momentum per unit mass of gas in the central kpc of each galaxy in blue and red for the primary and secondary, respectively.

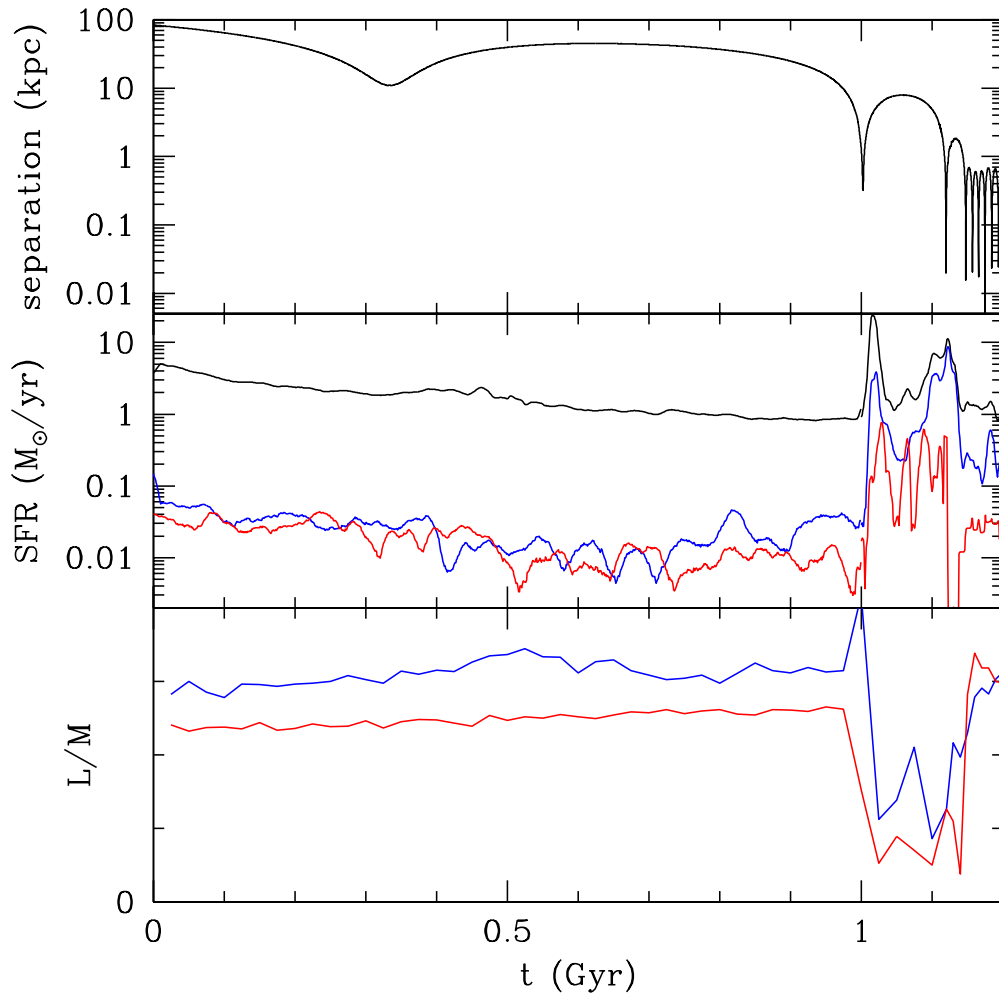


**Figure 3.11.** Results of the 1:2 retrograde (secondary) simulation. Top panel: separation between the central black holes in each galaxy as a function of time. Middle panel: Star formation rates as a function of time. The global star formation rate across both galaxies is shown in black. The rates in the central 100 pc of each galaxy are shown in blue and red for the primary and secondary, respectively. Bottom panel: angular momentum per unit mass of gas in the central kpc of each galaxy in blue and red for the primary and secondary, respectively.

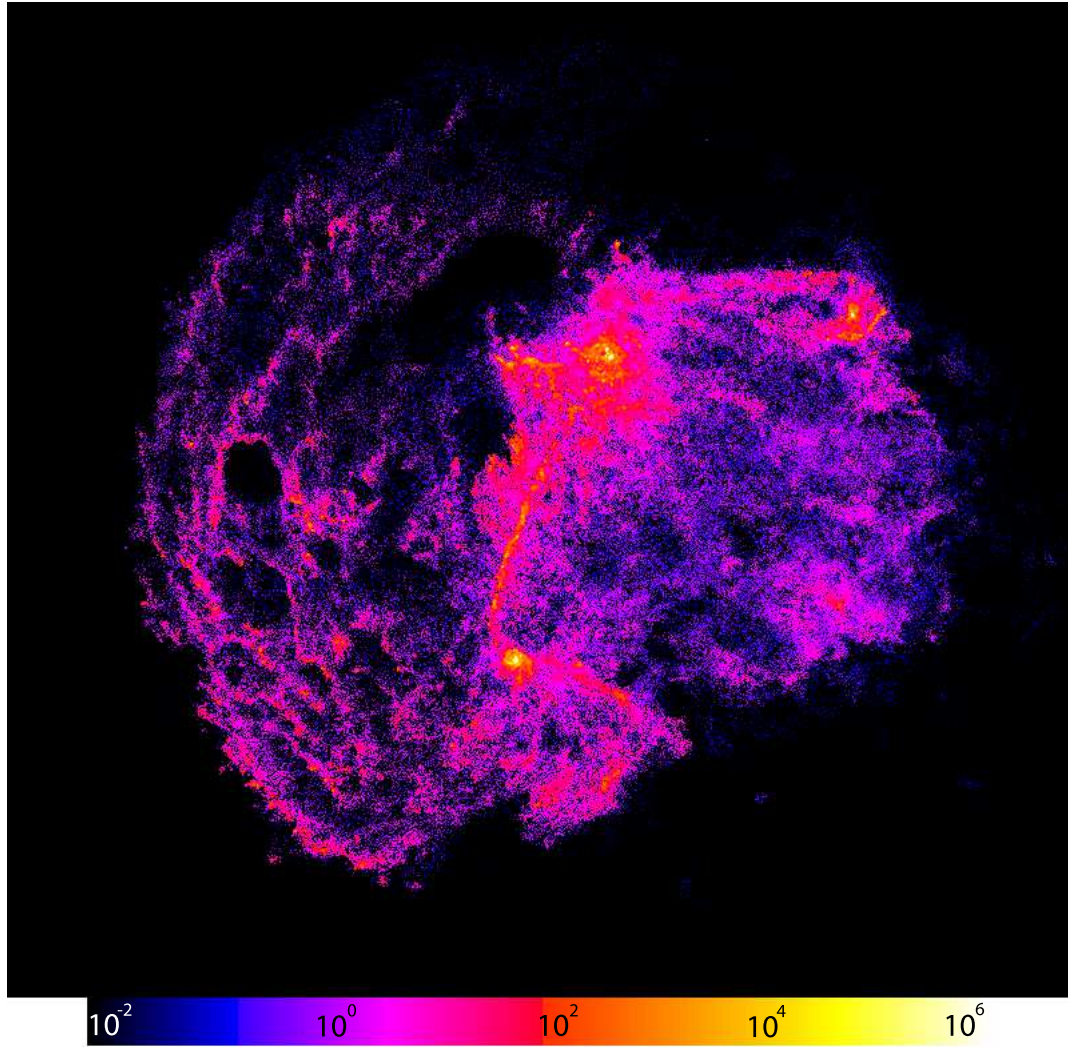


**Figure 3.12.** Gas density snapshot in the 1:2 retrograde (secondary) coplanar merger at  $t = 1.025$  Gyr, just following the second pericenter passage. The primary galaxy is at the bottom and the secondary is at the right. The dense gas at top center is gas in the tidally stripped bridge. The distance between the galaxies is 5.8 kpc. The colorbar shows the gas density scale (logarithmic) in units of  $\text{amu cm}^{-3}$ .

the mass of the two galaxies becomes more equal, the inclination seems to play less of a role in determining the strength of inflows in the disk interaction. Our 1:2 prograde coplanar and inclined mergers produce similar results (Figure 3.7), with the secondary galaxy disrupting the primary in both runs. Tilting the primary galaxy's disk in a more minor merger makes a large difference; the star formation in the secondary in the 1:4 inclined merger is far weaker than in the prograde coplanar merger and the primary is no longer disrupted. Our exploration of the possible orbital parameters is by no means exhaustive, but we have shown that the secondary nucleus can grow to be as dense as the primary for several orbits and disk orientations in a major merger (1:2).

An important aspect of each merger is the collision between the gaseous disks. Ram pressure during the second pericenter passage removes much of the gas in the secondary galaxy, leaving a massive gaseous bridge linking the galaxies. The survival of dense nuclear gas through the second pericenter and the formation of a new disk at apocenter are vital to producing a further starburst at third pericenter, at which point the nuclei have completed the majority of their star formation. We find that the gaseous disk that reforms in the secondary following second pericenter flips in angular momentum compared to the original in all our coplanar mergers except for the 1:10 case. Unfortunately, it is difficult to analytically follow the interaction between the disks and determine the cause of the spin flip. The spin direction depends on the angular momentum of the gaseous bridges and tidal arms that feed the secondary disk. It is also difficult to determine how the spin flip affects star formation during the third pericenter passage, when the secondary disk again collides with the primary and its disk takes on the spin direction of the more massive primary. The strongest burst of star formation in any of our mergers occurs in the 1:2 retrograde (secondary) run, suggesting that a prograde-retrograde encounter may be the most violent and lead to a strong starburst. This effect may enhance the star formation rate at third pericenter in our 1:2, 1:4, and 1:6 prograde coplanar mergers, where the spin flip following second pericenter has made the secondary disk now retrograde. We plan to study the influence and implications of the spin flip further in future work.

While we have focused on merger driven starbursts in our simulations, the majority of the star formation occurs during the early quiescent phase before the gas disks collide. As Cox et al. (2008) found, the starbursts do not efficiently convert a large amount of the global gas into stars in unequal mass mergers. While the global conversion of gas into stars is dominated by the initial phase, the starbursts contribute preferentially to the central region, where quiescent star formation contributes negligibly to the mass build up.

Observations of paired galaxies in the Sloan Digital Sky Survey agree with our result that the secondary galaxy in unequal mass mergers experiences stronger star formation. Woods & Geller (2007) consider 3613 galaxies in pairs and split them into minor and major pairs based on their relative magnitude. The major pairs (with a difference in  $z$  magnitude  $\Delta m_z < 2$ ) show signs of ongoing star formation in both galaxies. The minor pairs show signs of active star formation only in the less massive galaxy. Additionally, the activity in the galaxies increases at small separations. Accordingly, we find that both galaxies in our 1:2 mergers exhibit strong central star formation, whereas in our 1:6 and 1:10 mergers, only the secondary galaxy experiences significant merger induced star formation. The interacting system of NGC 7770 and NGC 7771 (stellar mass ratio 1:10) also shows an enhancement in star formation only in the less massive galaxy (Alonso-Herrero et al., 2012).

Merritt & Cruz (2001) studied minor mergers between giant elliptical galaxies and dwarf galaxies with relatively steeper central density profiles. If black holes are excluded from the galaxies, they find that the secondary galaxy’s cusp survives the merger intact, significantly increasing the central density of the merged galaxy. If black holes are included, however, tidal heating from the primary BH reduces the central density of the secondary galaxy on small scales and the central density of the merged galaxy is only increased slightly. We note that the primary BH is less massive in our mergers and is less important dynamically in the primary galaxy. It contributes negligibly to the tidal shock on the secondary nucleus during the final pericenter passages in our runs where the primary nucleus is disrupted.

### 3.4.1 BH Pairing and Binary Evolution

In agreement with the results of Kazantzidis et al. (2005) and Callegari et al. (2009), we find that gas dynamics and star formation are very important to the successful formation of a BH pair in minor mergers. In our simulations where the secondary galaxy is unable to sustain strong central star formation, the secondary BH is left at a separation of  $> 500$  pc, significantly delaying the formation of a BH binary (see binary formation timescales in Table 3.1). Without any surrounding stars and gas, the ‘naked’ BH from the secondary galaxy sinks more slowly due to dynamical friction. Additionally, the BH spends most of its orbit far from the center of the merger remnant where the ambient density is low and dynamical friction is inefficient.

When the secondary galaxy does build a dense cusp throughout the merger, the secondary’s nucleus survives the merger down to the center of the primary galaxy, efficiently forming a close BH pair. The BHs quickly reach the resolution limit of the simulation, near separations where the BHs will form a binary. When the primary nucleus is disrupted, the primary BH is left orbiting very close to the remnant. The dense central environment produces efficient friction on the BH’s orbit despite its low mass. Still, it is important to consider the interaction between the nuclei when estimating the overall timescale for BHs to coalesce. Even when both nuclei survive down to small scales in the merger, the following formation of a BH binary is not instantaneous.

Strong central star formation in the secondary preferentially leads to a dense merger remnant. In the 1:4 prograde coplanar merger, the survival of the secondary and disruption of the primary produces a steep density profile in the merged galaxy instead of the shallower initial profile of the primary (Fig. 3.3). Once the BH binary forms, it will be in a dense stellar environment. While our simulations cannot resolve the required scales, the binary shrinks through three-body interactions with nearby stars. A dense stellar environment increases the number of stars available for interaction with the binary, causing the binary to harden more quickly. The ejection of stars via three body interactions also provides a mechanism for the BH binary to disrupt the central cusp of the merger remnant (Milosavljević & Merritt, 2001).



### 3.4.2 Influence of Resolution

In order to follow the build up of central mass and the following dynamical interaction of the nuclei, numerical simulations must resolve very small scales. In the 1:4 coplanar merger, the secondary galaxy experiences much stronger nuclear star formation than the primary, but is denser only on scales of  $\leq 75$  pc when the nuclei begin to interact. Without high resolution on scales of tens of parsecs, the density contrast between the nuclei could not be studied. Additionally, tidal heating becomes strong enough to disrupt the nuclei only when they pass each other on scales  $\leq 50$  pc, scales that are unresolved in most studies of interacting galaxies.

We note that the minimum gas temperature is 10 K in the simulations presented here. During starbursts, many of the new stars form out of gas at temperatures of 10 - 100 K. At these low temperatures, however, the gas structure is not resolved. The smoothing length of the gas becomes smaller than the softening length at low temperatures, inhibiting further collapse (see discussion in Bate & Burkert, 1997), but the Jeans mass contains only a few particles. To test the impact of gas cooling on our results, we ran an additional 1:4 prograde coplanar merger with a gas temperature floor of 500 K, where the gas remains well resolved. The overall evolution of the merger is similar, although we see somewhat stronger central star formation in both galaxies than with a lower temperature floor as inflowing cold gas penetrates further into the galaxy before forming stars. The outcome of the merger is unchanged in this simulation.

## 3.5 Conclusions

We present simulations of unequal mass ratio galaxy mergers, focusing on the spatial distribution of merger triggered starbursts and the consequences for the dynamics of the central BHs. We find that the secondary galaxy generally experiences stronger nuclear star formation than the primary galaxy. In some mass ratios and orientations, the secondary galaxy becomes denser on small scales and disrupts the primary galaxy. The disruption is consistent with tidal heating due to fast collisions between the nuclei

at separations of  $\leq 50$  pc.

The survival of the secondary nucleus during the merger depends on the interaction between the gaseous disks of the galaxies. If the secondary has a high central gas mass and deep potential well to resist ram pressure, the gas will be compressed during the collision with the primary's disk, driving strong star formation. The majority of the nuclear star formation occurs following second and third pericenter. In order to sustain significant star formation during third pericenter, the secondary must recapture gas that was stripped by the primary galaxy. As the mass ratio of the merger decreases, the secondary's disk is less massive and is more strongly affected by ram pressure from the primary's disk. Ram pressure therefore removes much of the gas in the secondary galaxy, limiting the amount of central gas that is able to form stars.

If the secondary galaxy is able to form a dense central cusp, it is more resistant to heating from tidal shocks and retains a larger bound central mass, sinking further due to dynamical friction and leading more quickly to the formation of a close BH pair on scales of  $10 - 100$  pc. When the primary's nucleus is disrupted, we find that the binary formation timescale is fast, occurring in less than 100 Myr. In mergers where the secondary is instead disrupted due to insufficient central star formation, the formation of a binary is delayed (Table 3.1). We conclude that it is vital to follow star formation and the interaction between the nuclei on scales less than 100 pc in order to accurately understand the formation and evolution of BH binaries.

## CHAPTER 4

# Merger Driven Black Hole Accretion and Dual Active Galactic Nuclei

### 4.1 Introduction

Supermassive black hole pairs are a natural consequence of galaxy mergers between galaxies of similar mass (see Chapter 3). Observationally, however, there has been little evidence for their existence until recently. Galaxy mergers drive gaseous inflows which trigger both star formation (Mihos & Hernquist, 1996) and quasar activity (e.g. Di Matteo et al., 2005). If both galaxies in a merger contain central BHs, as is expected for massive galaxies (Ferrarese & Ford, 2005), then dual AGN, i.e. systems where both BHs are actively accreting and shining as AGN, should be common. The prediction of the timescale on which BH pairs can be observed as double quasars (Hennawi et al., 2006; Liu et al., 2011, and references therein) is a key diagnostic of BH merger rates and AGN triggering from mergers. Accordingly, dual AGN and quasars provide a clue in understanding how supermassive BHs grow and the relative importance of internal processes in the galaxy vs. external processes (e.g. mergers) in driving this growth.

The spatial resolution of the Hubble Space Telescope and Chandra led to the discovery of the first three cases of dual AGN in the center of the same galaxy, in LBQS 0103-2753, NGC 6240 and Arp 299 (Junkkarinen et al., 2001; Komossa et al., 2003; Ballo et al., 2004). Recently, more observations were focused on detecting spatially resolved dual AGN via various techniques (Gerke et al., 2007; Smith et al., 2010; Hudson et al., 2006; McGurk et al., 2011; Rodriguez et al., 2006; Bianchi et al., 2008; Barth et al., 2008; Comerford et al., 2009a; Liu et al., 2010; Piconcelli et al.,

2010; Comerford et al., 2009b; Green et al., 2010; Liu et al., 2011; Fu et al., 2011; Koss et al., 2010, 2011; Fabbiano et al., 2011). Studies of AGN in the Sloan Digital Sky Survey (SDSS) have found that  $\simeq 1$  percent of AGN have double peaked narrow emission lines, indicating a possible dual AGN (Comerford et al., 2009a; Smith et al., 2010). Some double peaked narrow emission line systems are, however, likely to be caused by gas kinematics rather than true dual AGN (Shen et al., 2011; Fu et al., 2012). After correcting for the spectroscopic incompleteness of SDSS, Liu et al. (2011) find that the dual fraction of candidate AGN is 3.6 percent.

Foreman et al. (2009) discuss how the relationship between the lifetime of an active SMBH,  $t_{\text{AGN}}$ , and the merging timescale,  $t_{\text{merg}}$ , plays a fundamental role in determining the observability of AGN pairs. If one assumes that most galaxies host SMBHs, that AGN/quasar activity is triggered by galaxy mergers, and that the lifetime of quasars equals the merger timescale,  $t_{\text{AGN}} \simeq t_{\text{merg}}$ , the probability of observing a dual quasar should be close to unity, if we do not consider additional factors, such as obscuration. If  $t_{\text{AGN}} \ll t_{\text{merg}}$  (Di Matteo et al., 2005; Hopkins et al., 2005), or if there is a delay in the triggering of the two quasars, then one might have ceased its activity before the other started. Foreman et al. (2009) also notice that the distribution of physical separations for luminous quasar pairs in SDSS peaks below 30 kpc, the lower limit of the physical resolution that can be resolved in the survey. The paucity of optically selected quasar pairs on galactic scales ( $\sim 0.1\%$  at  $L > 10^{45}$  erg s $^{-1}$ , Foreman et al., 2009; Hennawi et al., 2006) points toward non-simultaneous activity at large separations.

Volonteri et al. (2009) and Yu et al. (2011) also discuss models that reconcile theoretical merger rates of SMBHs and galaxies with the small fraction of binary quasars and dual AGN respectively. The lifetime of AGN, the gas content of the host galaxies and the dynamics of the merger are the main factors that explain the paucity of observed AGN pairs. Understanding the occurrence of AGN pairs therefore requires a thorough investigation and understanding of the detailed physical conditions describing the evolution of SMBHs during mergers.

We use high resolution simulations of unequal mass galaxy mergers to study

merger driven AGN in this chapter. We note that AGN activity can also be driven by secular processes, not solely by mergers. Here we investigate how and when mergers drive AGN activity. In Section 4.2, we discuss the accretion onto each BH individually and how the accretion rate is affected by the dynamics of the interacting galaxies. In Section 4.3, we consider the correlation between the accretion rates of the BHs and produce expectations for dual AGN fractions and timescales. We then compare our results to observations of dual AGN in Section 4.4. This work expands upon that of Van Wassenhove et al. (2012).

## 4.2 Merger Driven Active Galactic Nuclei

Active galactic nuclei are driven by gas accretion onto supermassive BHs on sub-parsec scales. The angular momentum of gas around the BH leads to the formation of an accretion disk, analagous to the disks that form around protostars. In an optically thick, radiatively efficient disk (Shakura & Sunyaev, 1973), viscosity transports angular momentum into the outskirts of the disk, allowing gas to sink closer to the BH. This viscosity may be supplied by tangled magnetic fields threading the accretion disk through the magnetorotational instability (Balbus & Hawley, 1998). A large fraction (0.05 - 0.42, depending on the spin of the BH) of the mass accreted onto the BH is converted into energy, making AGN very efficient and luminous engines and enabling them to outshine their host galaxies. As the luminosity of the AGN increases, the outward force of radiation pressure balances the force of gravity on gas in the accretion disk, limiting the accretion rate onto the BH to the Eddington limit,  $L_{Edd}$ , given by:

$$L_{Edd} = \frac{4\pi GM_{BH}m_p c}{\sigma_T}, \quad (4.1)$$

for spherical geometry, and assuming that all gas is hydrogen. Here  $m_p$  is the proton mass and  $\sigma_T$  is the Thomson cross section for an electron.

Supermassive BH accretion disks form on AU scales, making them impossible to resolve in numerical simulations that also include the host galaxy. The required resolution near the BH is prohibitive on the larger scales of the galaxy. Addition-

ally, general relativity and magnetic fields become important near the BH, further increasing the computational cost and complexity of simulating accretion. Therefore, simulations of supermassive BH accretion (De Villiers et al., 2003, 2005; Hawley & Krolik, 2006; Shiokawa et al., 2012; Dibi et al., 2012) generally only include the BH and the local disk on scales of  $\simeq 100$  gravitational radii.

Larger scale simulations of galaxies that include BHs, such as those presented here, must approximate accretion with sub-grid models. We use an approximation of the Bondi-Hoyle-Lyttleton formula, based on the properties of local gas particles:

$$\dot{M}_{\text{BH}} = \frac{4\pi G^2 M_{\text{BH}}^2 \rho_{\text{g}}}{(c_{\text{s}}^2 + v^2)^{3/2}}. \quad (4.2)$$

Here  $M_{\text{BH}}$  is the mass of the accreting BH,  $\rho_{\text{g}}$  and  $c_{\text{s}}$  are the density and sound speed of the surrounding gaseous medium, and  $v$  is the velocity of the BH relative to the medium. Bondi accretion assumes the spherical capture of gas due to the gravitational influence of the BH. We note that the true accretion rate is dependent on the physics of the small scale accretion disk around the BH, but the Bondi estimate may still apply if the disk itself is fed by Bondi accretion. Further details of the BH accretion model in GASOLINE can be found in Appendix A.

A key assumption in using Equation 4.2 is that the gas properties on large scales reflect the properties of unresolved gas near the BH. If gas is efficiently transported from resolved scales (in this case tens of parsecs) down to the BH, however, then the large scale gas can reasonably be used to estimate the accretion rate onto the BH. Hopkins & Quataert (2010) studied the transfer of gas from kiloparsec scales to sub-parsec scales in a series of linked numerical simulations. They found that a variety of gas features act to transport gas in, including spiral arms, bars, and clumps. For gas rich systems, gravitational instabilities were able to drive high accretion rates onto the central BH. Furthermore, the accretion rate was correlated with the star formation rate of the galaxy, with the correlation improving when the nuclear star formation rate was adopted. These results indicate a link between gas on large scales, where our simulations can resolve the gas properties, and the gas that flows down to

the BH on smaller scales. Hopkins & Quataert find variability in the gas inflow on very short timescales  $< 10^5$  yr, whereas the gas properties that control the accretion rate in our simulations vary on timescales of a few  $10^5$  yr. While we cannot resolve this short timescale variability, the link between small scale ( $< 1$  pc) inflows and star formation on 10 and 100 pc scales (and therefore gas properties on these scales) found by Hopkins & Quataert suggests that our accretion prescription gives a reasonable estimate of the true inflow rate on smaller, unresolved scales.

We include also the effects of BH feedback. A fraction  $\epsilon_f$  of the accreted energy in any timestep is added as thermal energy to the nearest gas particle to the BH. This thermal feedback allows the BH to regulate its own accretion rate on timescales of a few  $10^5$  yr.  $\epsilon_f$  is set to 0.001 to produce the expected amount of growth during our mergers to match the observed scaling relations (more details in Appendix A).

Equation 4.2 indicates that BH accretion is high in an environment with cold, dense gas, yielding a high gas density,  $\rho_g$ , and a low sound speed,  $c_s$ . The relative velocity,  $v$ , is particularly important in situations such as an evolving BH binary in a circumnuclear disk, where one BH may be moving quickly relative to the gaseous medium (Dotti et al., 2009). In our simulations, the accretion rate is highest when the BH is supplied with dense gas via gaseous inflows. The same inflows that drive gas into the central regions of the galaxies (see Section 3.2), fueling a burst of star formation, also fuel the central BH. In the early phases of each merger, before the second pericenter passage, each galaxy is growing quiescently and there are no global gaseous inflows. Accordingly, the central star formation rate remains low in each galaxy. We also find that the BH accretion rate remains relative low during this initial phase. The Eddington fraction of the BH, given by:

$$f_{\text{Edd}} = \frac{\dot{M}_{\text{BH}}}{\dot{M}_{\text{Edd}}} = \frac{\epsilon_r \dot{M}_{\text{BH}} c^2}{L_{\text{Edd}}}, \quad (4.3)$$

generally ranges from 0.001 to 0.1. Here we have converted the accretion rate of the BH into a luminosity using  $L = \epsilon_r \dot{M}_{\text{BH}} c^2$ , where  $\epsilon_r$  is the radiative efficiency, which we set to 0.1.

Occasionally, when a clump of cold gas sinks toward the BH, the accretion rate increases to  $f_{\text{Edd}} > 0.1$  for  $\simeq 1$  Myr before feedback from the BH heats the gas and stops further accretion. The short episodes of high accretion are sporadic and do not significantly increase the mass of the BHs. Generally, each BH grows by  $\simeq 20\text{--}40$  percent during the initial phase of the merger leading up to second pericenter ( $\simeq 1 - 1.5$  Gyr).

#### 4.2.1 Accretion Driven by Gaseous Inflows

Stronger accretion occurs in the later stages of the merger following second pericenter when strong gas inflows occur. For a discussion of the mechanics of these inflows, we refer the reader to Section 3.2. We discuss here how the inflows in each simulation impact the accretion rates of the central BHs. We first focus on the prograde coplanar mergers and examine how the merger driven AGN activity varies with mass ratio and between the two BHs in each merger. We then consider accretion in our inclined and retrograde mergers and how it differs from the prograde coplanar cases.

#### Impact of Mass Ratio

We first consider the prograde coplanar mergers and how the AGN activity varies with mass ratio. We focus first on the accretion rate of the secondary BH, denoted here as BH<sub>2</sub>. As discussed in Sections 3.2 and 3.3, the secondary galaxy experiences strong gas inflows during pericenter passages. The central gas resulting from the inflow is compressed by the ram pressure interaction with the primary’s disk, increasing the density of the gas and driving strong accretion. In the 1:2 and 1:4 mergers, the main growth in BH<sub>2</sub> occurs during the third pericenter passage and the final merger of the nuclei, when the nuclear star formation rate also reaches its highest values. Figure 4.1 shows the accretion during the late stages of the 1:2 merger, beginning just before second pericenter. The late pericenter passages drive consistent accretion onto BH<sub>2</sub> at  $f_{\text{Edd}} > 0.1$  for  $\simeq 40$  Myr, significantly increasing the mass of the BH relative to its initial value (bottom panel of Figure 4.1).

In the 1:6 and 1:10 mergers, the accretion onto BH<sub>2</sub> is similar to the 1:2 and 1:4 mergers, triggered by inflows following pericenter passages. However, the shallower



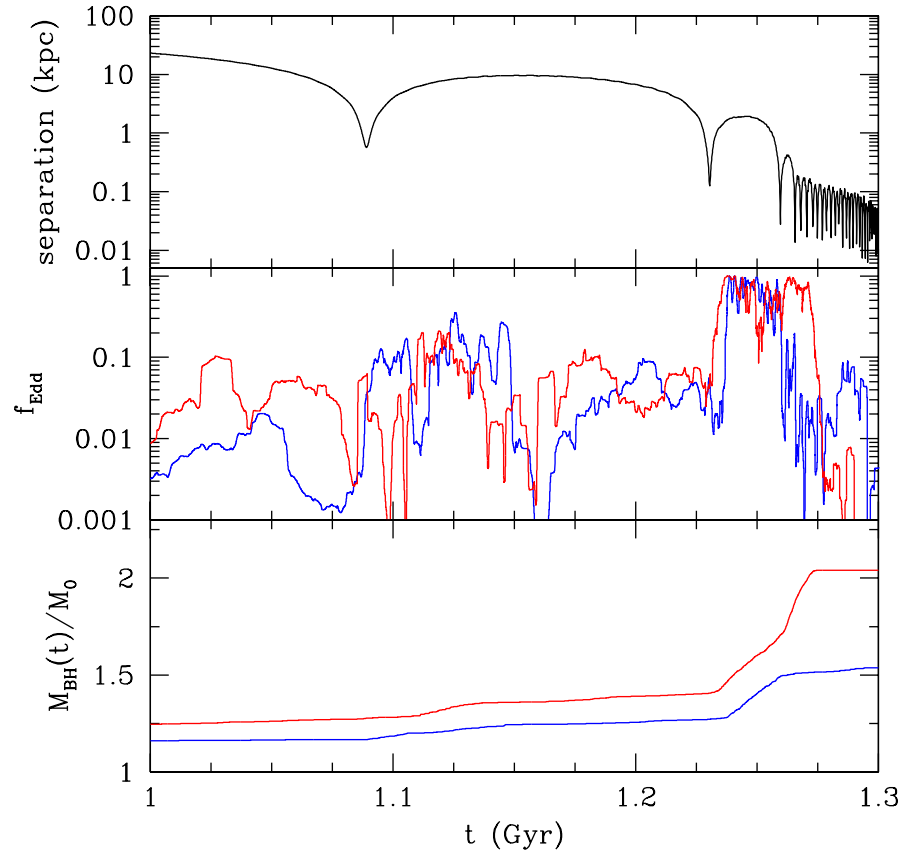


**Figure 4.1.** Accretion during the late stages of the 1:2 prograde coplanar merger. Top panel: separation between the central black holes as a function of time, beginning just before the second pericenter passage. Middle panel: Eddington fraction of each BH. Bottom panel: mass of each BH divided by its initial mass. The primary BH is shown in blue. The secondary BH is shown in red.

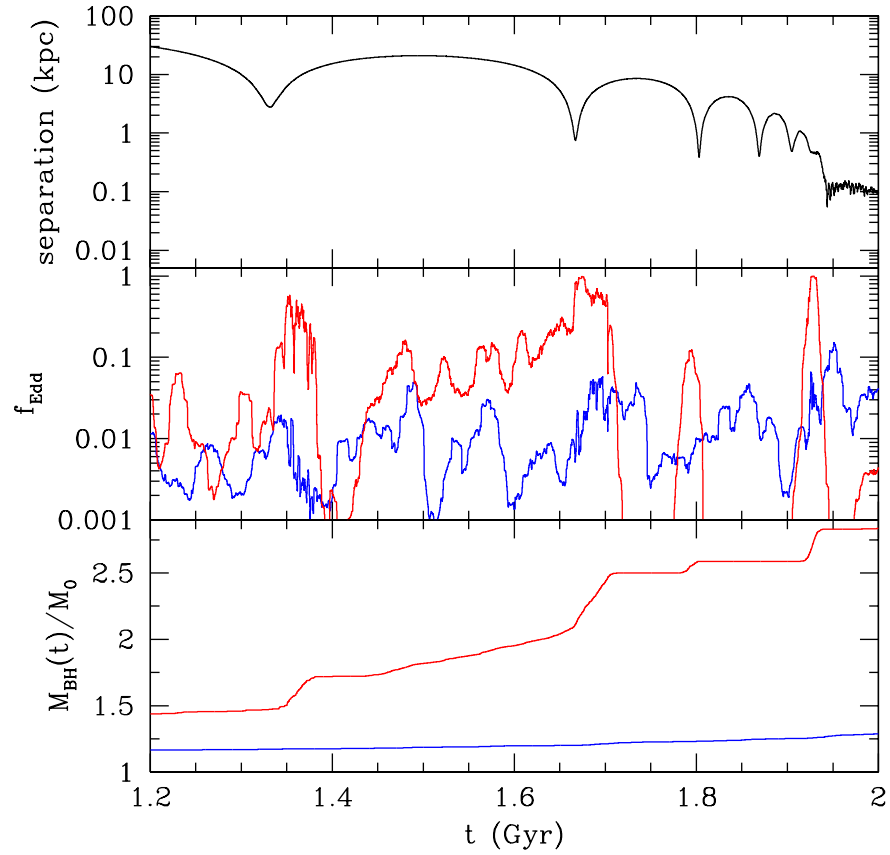


**Figure 4.2.** Accretion during the late stages of the 1:6 prograde coplanar merger. Top panel: separation between the central black holes as a function of time, beginning just before the second pericenter passage. Middle panel: Eddington fraction of each BH. Bottom panel: mass of each BH divided by its initial mass. The primary BH is shown in blue. The secondary BH is shown in red.

potential well of the secondary galaxy relative to the primary means that the disk is more strongly stripped by ram pressure from the primary’s disk. At third pericenter, the secondary loses the majority of its gas. Figure 4.2 shows the accretion during the 1:6 merger, including the sudden drop in  $f_{\text{Edd}}$  for BH<sub>2</sub> at  $t = 1.7$  Gyr. A small amount of gas remains near the BH and fuels moderate accretion at fourth pericenter, then is expelled from the galaxy due to AGN-driven outflows (AGN feedback). Later, at  $t \simeq 1.9$  Gyr, the secondary galaxy’s orbit circularizes within the disk of the primary and gas capture drives a final burst of accretion onto BH<sub>2</sub>.

BH<sub>1</sub> accretes similarly to BH<sub>2</sub> in the 1:2 merger. However, as the mass of the secondary galaxy shrinks relative to the mass of the primary in our lower mass ratio mergers, the tidal forces and gas inflows in the primary galaxy weaken. Therefore, as the mass ratio decreases, BH<sub>1</sub> grows quiescently throughout the merger, rather than accreting efficiently following pericenter passages. Since BH<sub>1</sub> grows quiescently, its increase in mass is tied mainly to the length of the merger rather than the dynamics of the interaction between the galaxies. We see, therefore, that BH<sub>1</sub> and BH<sub>2</sub> accrete in a fundamentally different manner as the mass ratio of the merger decreases.

### **Inclined Mergers**

The inclined mergers show a different mode of BH fueling than the prograde coplanar mergers. In the coplanar runs, the mass increase in BH<sub>2</sub> is dominated by short bursts of accretion following pericenter passages. In the inclined mergers, the galaxies experience weaker tidal torques and gas inflows. Instead of a burst of accretion, the BHs grow gradually following second pericenter. Following the disk interaction and the stripping of much of the secondary’s gas, the disk reforms from gas in the bridge linking the galaxies. This gas has low angular momentum and drives constant, moderate star formation and accretion. Figure 4.3 shows the evolution of BH<sub>1</sub> and BH<sub>2</sub> in the 1:2 inclined merger. BH<sub>2</sub> sustains an Eddington fraction  $f_{\text{Edd}} \geq 0.1$  for 175 Myr between second and third pericenter, but does not reach the Eddington limit as in the coplanar mergers. The result is persistent, moderate growth in the BH rather than bursts of accretion. In the 1:4 inclined merger, BH<sub>1</sub> transitions toward

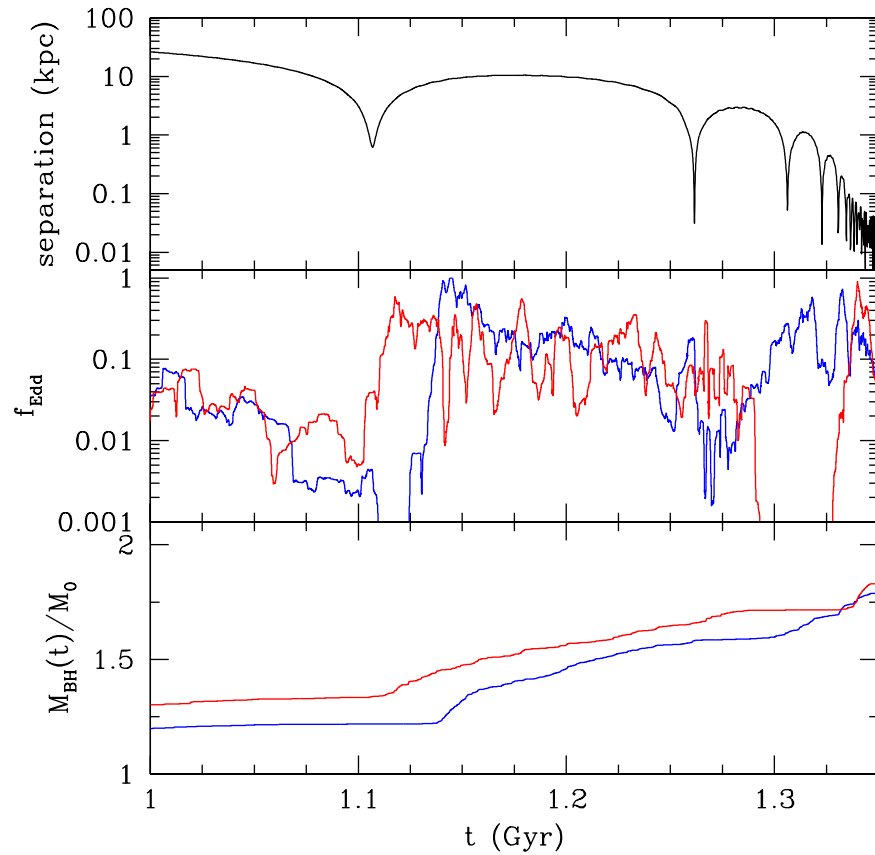


**Figure 4.3.** Accretion during the late stages of the 1:2 inclined merger. Top panel: separation between the central black holes as a function of time, beginning just before the second pericenter passage. Middle panel: Eddington fraction of each BH. Bottom panel: mass of each BH divided by its initial mass. The primary BH is shown in blue. The secondary BH is shown in red.

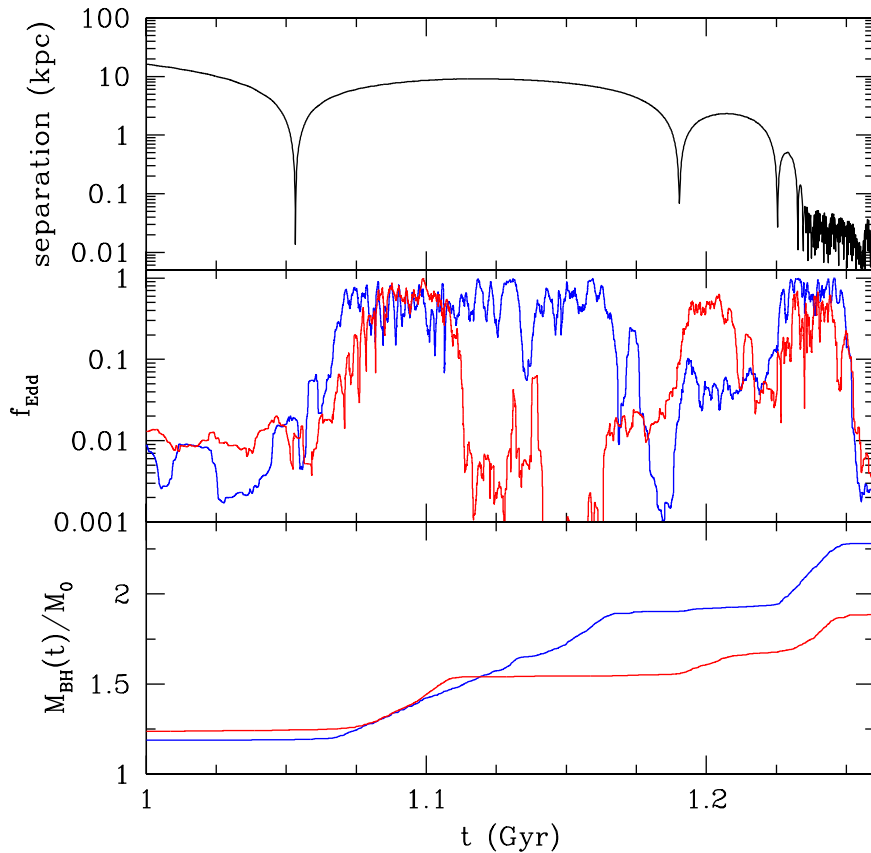


**Figure 4.4.** Accretion during the late stages of the 1:2 retrograde (primary) merger. Top panel: separation between the central black holes as a function of time, beginning just before the second pericenter passage. Middle panel: Eddington fraction of each BH. Bottom panel: mass of each BH divided by its initial mass. The primary BH is shown in blue. The secondary BH is shown in red.

quiescent growth throughout the merger, as in the coplanar case, suggesting that the mass ratio has a stronger influence on the accretion rates than the orbital parameters.

### Retrograde Mergers

In the 1:2 retrograde (primary) merger, the primary galaxy develops a strong bar after second pericenter. The bar drives gas into the center of the galaxy, driving consistent accretion onto BH<sub>1</sub> (Figure 4.4). No strong, persistent bar forms in the secondary galaxy, where the inflows are strongest during the disk collisions at pericenter passages, as in the prograde merger. The bar enables BH<sub>1</sub> to accrete at near the Eddington limit for  $\simeq 100$  Myr between second and third pericenters, whereas BH<sub>2</sub> only accretes at close to the Eddington limit during short bursts. Overall, the

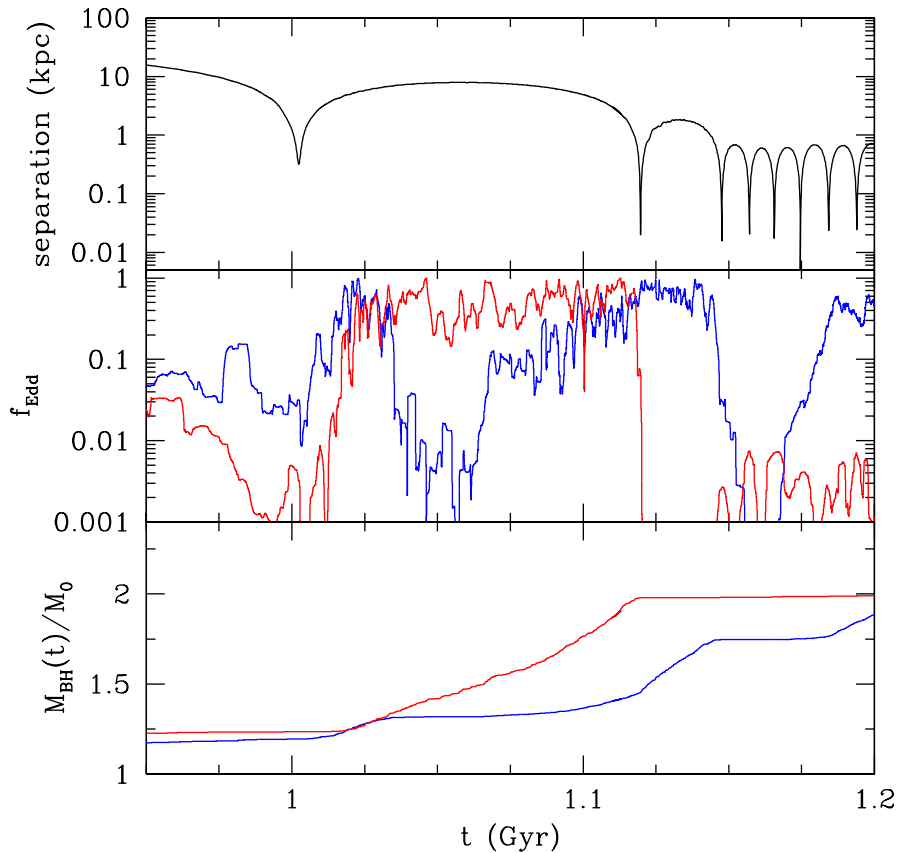


**Figure 4.5.** Accretion during the late stages of the 1:2 retrograde (secondary) merger. Top panel: separation between the central black holes as a function of time, beginning just before the second pericenter passage. Middle panel: Eddington fraction of each BH. Bottom panel: mass of each BH divided by its initial mass. The primary BH is shown in blue. The secondary BH is shown in red.

BH<sub>1</sub> grows more relative to its initial mass than BH<sub>2</sub>.

The most violent collision between the disks occurs in the 1:2 retrograde (secondary) merger. BH<sub>1</sub> grows similarly to the prograde run, during short bursts following pericenter passages. The violent collision strips much of the gas from the secondary galaxy, leading BH<sub>2</sub> to accrete from infalling low angular momentum gas as in the inclined mergers. Although we see weaker star formation in the secondary galaxy compared to the primary (see Section 3.3), BH<sub>2</sub> grows more relative to its initial mass than BH<sub>1</sub>.

Overall, we find several mechanisms that drive accretion. Strong gas inflows lead to a high central gas density that survives and is compressed by ram pressure from the

companion galaxy, driving a short (tens of Myr) burst of star formation and accretion. If inflows are instead weak, the gas is more strongly stripped and accretion is driven by the low angular momentum gas that reforms the disk, driving lower accretion rates but for a longer time period. In cases where strong bars form, they can also drive constant, strong accretion between pericenter passages (primarily between second and third). Lastly, we note that the primary galaxy is relatively unperturbed in low mass ratio mergers, leaving  $\text{BH}_1$  to accrete quiescently.

#### 4.2.2 Evolution of the Black Hole Mass Ratio

Here we briefly discuss the relative growth between the BHs in each merger. In general, the BHs in unequal mass mergers do not preserve their initial mass ratio. Callegari et al. (2011) investigated the evolution of the mass ratio of BHs in 1:10 mass ratio mergers and found significant deviations of the mass ratio from  $q = 0.1$ . In their most gas rich merger, the mass ratio grew to  $\simeq 0.5$  before the secondary nucleus was disrupted. Indeed, it is natural to expect that the BH mass ratio will increase in unequal mass mergers. The smaller galaxy experiences stronger tidal forces throughout the merger, generally driving stronger gaseous inflows than in the primary galaxy.  $\text{BH}_2$  should therefore grow more efficiently than the primary and the mass ratio should increase.

Figure 4.6 shows the evolution of the BH mass ratio in each simulation. We find that the mass ratio remains the same or increases in all cases except the 1:2 retrograde (primary) merger, where the mass ratio instead decreases. In the 1:2 retrograde (primary) merger, the strong bar that develops in the primary feeds  $\text{BH}_1$  efficiently, increasing the mass of  $\text{BH}_1$  relative to  $\text{BH}_2$  (Figure 4.4). In two simulations, the final BH mass ratio has changed little from the initial ratio: the 1:2 inclined and 1:2 retrograde (secondary) mergers. In the 1:2 inclined merger, a weak bar drives steady accretion onto  $\text{BH}_1$  while  $\text{BH}_2$  accretes from low angular momentum gas that is reforming the disk following the second pericenter passage. Both BHs grow at a similar rate and the BH mass ratio remains near the initial 0.5. In the 1:2 retrograde (secondary) merger, the mass ratio increases initially until the secondary galaxy loses

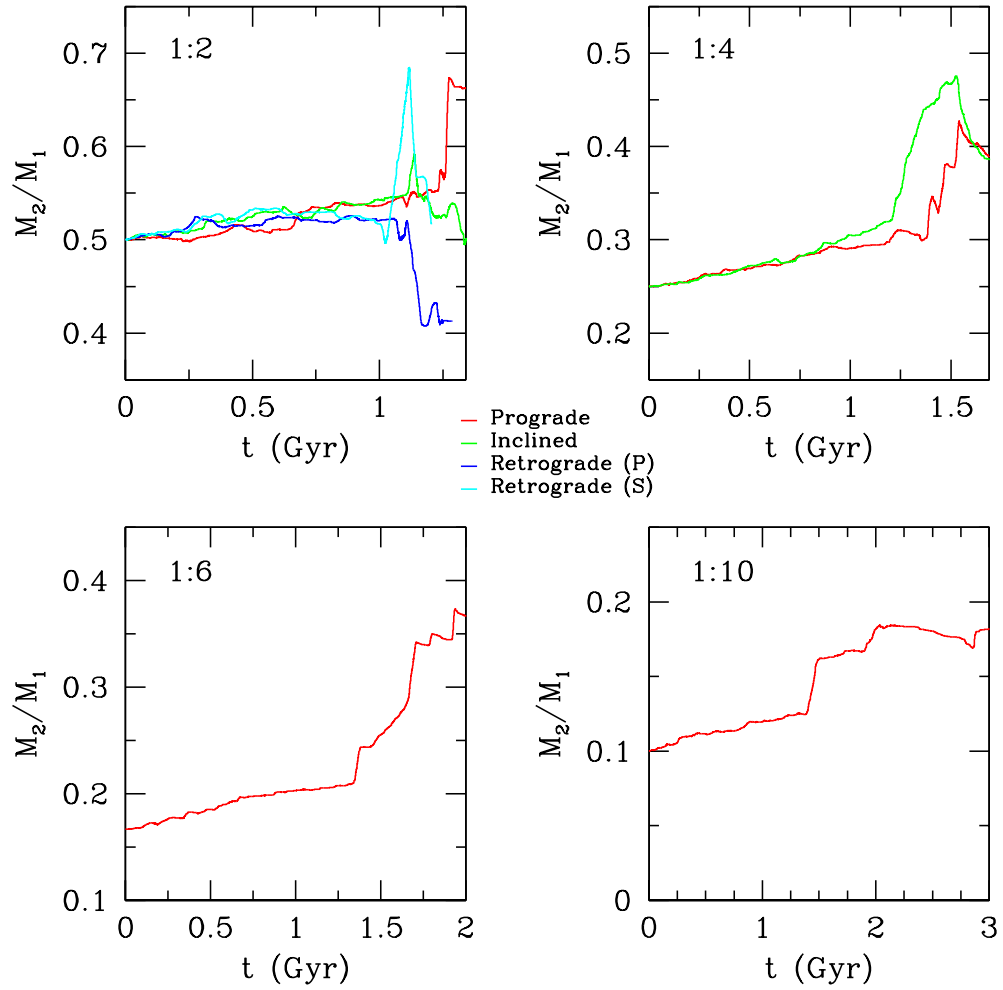


**Figure 4.6.** Evolution of the BH mass ratio. Top left: 1:2 mass ratio mergers. Top right: 1:4 mass ratio mergers. Bottom left: 1:6 mass ratio merger. Bottom right: 1:10 mass ratio merger. The prograde coplanar mergers are shown in red. Inclined mergers are shown in green. The retrograde (primary) and retrograde (secondary) mergers are shown in blue and cyan, respectively.



the majority of its gas at third pericenter, preventing further accretion. BH<sub>1</sub> grows efficiently in a burst of accretion at third pericenter, driving the mass ratio back toward 0.5. As expected, low mass ratio mergers lead to an increase in the BH mass ratio due to the relatively stronger gaseous inflows in the secondary galaxy than in the primary.

We note that we have one simulation with very similar parameters to a simulation in Callegari et al. (2011), whose fiducial run was a 1:10 merger between disk galaxies with a gas fraction of  $f_g = 0.3$ . Up until the circularization of the secondary's orbit inside the disk of the primary, our evolution of the BH mass ratio agrees well with theirs. They find a further strong increase in the mass ratio during the circularization, increasing to  $\simeq 0.3$ , whereas we find that the mass ratio remains relatively constant. Callegari et al. (2011) use initial BH masses that are one sixth as massive as our BHs, however. The gas captured from the disk of the primary drives moderate growth in our BH, but could drive stronger sustained accretion in a less massive BH, increasing the mass ratio. We find the same general result, however. In minor mergers, the BH mass ratio may increase significantly above the initial ratio.

#### 4.2.3 Correlation between Star Formation and BH Accretion

We find a strong connection between nuclear star formation and BH accretion in our mergers. The same gaseous inflows that fuel nuclear (<100 pc) star formation also fuel the BH. The correlation is strongest in our 1:2 coplanar mergers where there is a strong interaction between the disks. In the 1:2 prograde coplanar and two retrograde runs, 81-94 percent of strong BH accretion with  $f_{\text{Edd}} > 0.5$  is accompanied by nuclear star formation  $\geq 0.05 M_{\odot} \text{ yr}^{-1}$ , above the quiescent star formation rate in both galaxies. We define the quiescent star formation rate by the rate between first and second pericenter, when the galaxies evolve as if in isolation and do not strongly interact. The quiescent nuclear star formation rate in each galaxy is  $\leq 0.02 M_{\odot} \text{ yr}^{-1}$ . The strongest BH accretion is even more likely to coincide with nuclear star formation: 85 - 97 percent of accretion with  $f_{\text{Edd}} > 0.9$  is accompanied by star formation a factor of two or more above the quiescent rate.

In inclined mergers, where the gaseous inflows in the disks are weaker, 32 - 67 percent of accretion at  $f_{Edd} > 0.5$  is accompanied by star formation a factor of two or more above the quiescent rate. At higher accretion rates near Eddington ( $f_{Edd} > 0.9$ ), only 39 - 71 percent of the accretion is coincident with strong nuclear star formation. The connection between accretion and star formation is weaker here than in the coplanar mergers because both are driven by gradual accretion of low angular momentum gas into the nucleus rather than a strong, sudden inflow following pericenter passages. The gas density is therefore more variable across the nucleus and more prone to heating from stellar and BH feedback on short timescales, introducing variability between the star formation and accretion rates.

The connection is weakest when the galaxies are not interacting. During the early phase of the merger prior to second pericenter, the BHs accrete in short ( $\simeq 1$  Myr) bursts from clumps of cold gas that pass near the BH. These clumps do not contribute significantly to the nuclear star formation rate - a high BH accretion rate can be produced with much less gas than is necessary to appreciably enhance the nuclear star formation rate. Prior to second pericenter, we find that nuclear star formation and accretion are not linked. The total time with strong accretion and a temporary enhancement in nuclear star formation is consistent with the random expectation for overlap between the two. In our low mass ratio mergers, BH<sub>1</sub> accretes quiescently throughout the merger. While the secondary galaxy sustains a strong connection between accretion and star formation, the primary galaxy does not.

We note that weak inflows can appreciably increase the BH mass without increasing the stellar mass of the nuclear region through star formation. Figure 4.6 shows that the BH mass ratio in the 1:4 inclined merger grows more quickly than in the 1:4 coplanar merger. However, Section 3.3 showed that the nuclear star formation was significantly weaker in the inclined merger than in the coplanar merger. The low angular momentum gas that reforms the disk of the secondary galaxy after the second pericenter feeds BH<sub>2</sub> more efficiently than it does the nuclear star formation rate.

The connection between star formation and BH accretion is particularly impor-

tant because strong star formation may complicate detection of AGN using optical spectroscopy. The ratios between optical emission lines can be used to determine the ionization source in hot gas (Baldwin et al., 1981), distinguishing among HII regions, AGN, and shock heated gas. Strong star formation may dilute the spectral signatures of an AGN, preventing its detection using emission line diagnostics. Numerous searches for AGN in the infrared and X-rays have discovered AGN that were missed in the optical due to star formation or obscuration (Goulding & Alexander, 2009; Schawinski et al., 2010; Koss et al., 2010, 2011).

### 4.3 Dual Active Galactic Nuclei

We now consider the correlation between the accretion rates of the two BHs in each simulation. When both BHs simultaneously accrete such that two separate AGN are observable, our systems represent dual AGN. Dual AGN represent a test of BH accretion during galaxy mergers, where the theoretical expectation is that gaseous inflows should efficiently feed both BHs. We investigate the expectation for dual AGN activity in galaxy mergers spanning a variety of mass ratios and orbital parameters. We then compare our results to the findings of recent surveys in Section 4.4.

Table 4.1 shows the total dual AGN timescale in each merger given a threshold for observability of the two AGN. The observability threshold is imposed upon both BHs separately. Bolometric luminosities are calculated directly from the mass accretion rate using  $L_{\text{bol}} = \epsilon_r \dot{M}_{\text{BH}} c^2$ , assuming a radiative efficiency,  $\epsilon_r$ , of 0.1. To produce the dual AGN timescales, we consider whether both BHs meet the observational threshold at each computational timestep. Each timestep ranges from  $3 \times 10^2$  to  $10^5$  yr. The final timescale is the sum of all timesteps when both BHs meet the given threshold simultaneously. The luminosity thresholds approximate observational constraints whereas the  $f_{\text{Edd}}$  thresholds reveal information about how efficiently each BH is accreting relative to the Eddington limit,  $f_{\text{Edd}} = 1$ , regardless of its mass. For reference, the Eddington luminosity of a BH with  $M_{\text{BH}} = 3 \times 10^6 M_{\odot}$ , corresponding to the initial mass of BH<sub>1</sub> in each simulation, is  $3 \times 10^{44}$  erg s<sup>-1</sup>.

At the lowest levels of activity that we consider,  $L_{\text{bol}} > 10^{42}$  erg s<sup>-1</sup> or  $f_{\text{Edd}} >$

| Simulation          | $t_{sim}$ | $L_{bol} > L_{42}$ | $L_{bol} > L_{43}$ | $L_{bol} > L_{44}$ | $f_{Edd} > 0.005$ | $f_{Edd} > 0.05$ | $f_{Edd} > 0.5$ |
|---------------------|-----------|--------------------|--------------------|--------------------|-------------------|------------------|-----------------|
| Prograde Coplanar   |           |                    |                    |                    |                   |                  |                 |
| 1:2                 | 1.34      | 703                | 69.3               | 11.5               | 547               | 41.6             | 7.9             |
| 1:4                 | 1.55      | 643                | 50.7               | 1.9                | 618               | 35.7             | 0.71            |
| 1:6                 | 2.03      | 646                | 29.9               | 0.19               | 672               | 19.9             | 0.04            |
| 1:10                | 3.1       | 533                | 7.9                | 0                  | 778               | 16.5             | 0               |
| Inclined            |           |                    |                    |                    |                   |                  |                 |
| 1:2                 | 1.37      | 770                | 98.4               | 4.9                | 616               | 50.8             | 1.6             |
| 1:4                 | 1.69      | 699                | 41.8               | 0.4                | 634               | 25.2             | 0.1             |
| Retrograde Coplanar |           |                    |                    |                    |                   |                  |                 |
| 1:2 (Prim.)         | 1.29      | 703                | 90.1               | 16.0               | 561               | 57.0             | 9.4             |
| 1:2 (Sec.)          | 1.2       | 599                | 78.2               | 14.3               | 465               | 54.1             | 6.8             |

**Table 4.1.** Dual AGN timescales in each simulation given a limit for detection, imposed on both BHs simultaneously. All values are in units of Myr except the first column,  $t_{sim}$ , which gives the total length of each simulation in Gyr. The luminosity thresholds ( $L_{42} \equiv 10^{42}$  erg s $^{-1}$ ;  $L_{43} \equiv 10^{43}$  erg s $^{-1}$ ;  $L_{44} \equiv 10^{44}$  erg s $^{-1}$ ) are imposed on the bolometric luminosity of each BH, given by  $L_{bol} = \epsilon_r \dot{M}_{BH} c^2$ , assuming a radiative efficiency  $\epsilon_r$  of 10 percent.

0.005, both BHs are active individually for  $\simeq 50 - 80$  percent of the simulation. The activity is not triggered by the dynamics of the merger. Instead, this represents quiescent accretion onto both BHs. The total dual AGN timescale (although these nuclei would not generally be considered ‘active’ because of their faintness) is consistent with the expectation for chance simultaneous activations of both AGN, but still represents a significant fraction of the total length of each simulation ( $t_{sim}$ , given in Table 4.1).

At higher levels of accretion,  $L_{bol} > 10^{44}$  erg s $^{-1}$  or  $f_{Edd} > 0.5$ , we instead probe accretion that is triggered by the galaxy merger. The BHs only reach such high accretion rates very briefly during the quiescent phase. The majority of the strong activity occurs instead following the second pericenter passage. The total time spent at high accretion rates is  $\leq 7$  percent of the total length of the merger, allowing for a relatively short dual AGN timescale. In the 1:2 mergers, the accretion onto both BHs is strongly correlated, exceeding the expectation for random dual AGN activity by a factor of 4 - 12 and producing a total dual AGN timescale of 4.9 - 16 Myr. In the lower mass ratio mergers, the primary galaxy is less perturbed during the merger, resulting in weaker gas inflows and less merger triggered accretion onto BH $_1$ . BH $_1$  is then active for 2 percent of the total simulation or less at  $L_{bol} > 10^{44}$  erg s $^{-1}$  and accretes at  $f_{Edd} > 0.5$  a factor of 2 - 16 less than BH $_2$  does. This results in a lower dual AGN timescale and a weaker correlation between the BH accretion rates which

is consistent with the random expectation.

Several factors contribute to the shorter dual AGN timescale in our mergers with mass ratios of 1:4 and below, despite the fact that the overall simulation is longer. Since BH<sub>1</sub> accretes quiescently, it is rarely active at the highest accretion rates we consider and its activity is not well correlated with that of BH<sub>2</sub>. Additionally, the secondary galaxy is more affected by ram pressure stripping and loses all its gas in the 1:6 and 1:10 mergers. At that point, BH<sub>2</sub> stops accreting, preventing both BHs from accreting simultaneously for a significant amount of the merger ( $\simeq 150$  Myr in the 1:6 merger and  $\simeq 600$  Myr in the 1:10 merger). Also, BH<sub>2</sub> is less massive in lower mass mergers and must accrete at relatively higher  $f_{\text{Edd}}$  in order to be observable at a given  $L_{\text{bol}}$ . In fact,  $L_{\text{bol}} = 10^{44}$  erg s<sup>-1</sup> exceeds the Eddington luminosity for BH<sub>2</sub> in the 1:10 merger, so there is no detectable dual AGN activity at this luminosity.

### Impact of Orbital Parameters

The inclined mergers produce less dual activity at high accretion rates. Weaker gaseous inflows at second pericenter produce less strong, correlated accretion onto the BHs. In the 1:2 inclined case, both BHs instead accrete continuously at moderate luminosities between second and third the pericenter passages before the secondary loses most of its gas. While the dual AGN timescale is shorter than in the coplanar merger at high accretion rates, it is longer at moderate and low accretion rates. In the 1:4 inclined merger, BH<sub>1</sub> accretes largely quiescently until the secondary galaxy has lost its gas due to ram pressure stripping, resulting in a low dual AGN timescale. The retrograde mergers yield similar or longer dual AGN timescales than the 1:2 prograde merger due to the more violent collision between the gaseous disks at second pericenter. The collision drives stronger accretion following second pericenter than in the prograde merger.

#### 4.3.1 Impact of Observational Constraints

To be detected as a dual AGN, the two AGN must be detected separately. We consider potential observational constraints and how they affect the observable dual AGN timescales. We impose spatial cutoffs, representing resolution limitations in imaging

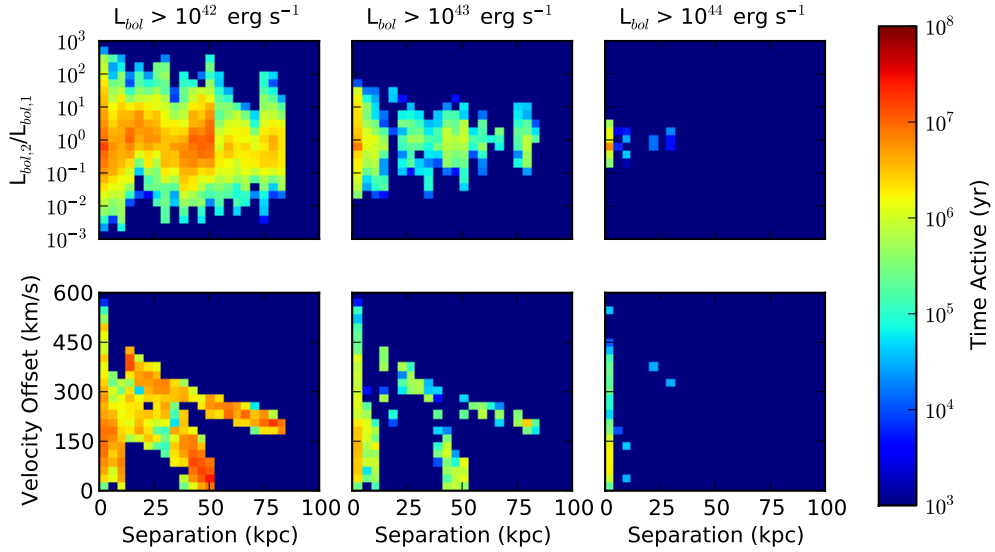


**Figure 4.7.** Dual AGN observability timescales in the 1:2 prograde coplanar merger from Van Wassenhove et al. (2012). Top panels: luminosity ratio between the two BHs as a function of BH separation when both BHs are accreting at the given luminosity. Bottom panels: velocity offset between the BHs as a function of separation when they are observable as a dual AGN. The color of each point indicates the total dual AGN timescale.

surveys, where the two AGN must be spatially resolved into separate sources. To mimic spectroscopic surveys of dual AGN (e.g. Comerford et al., 2009a), we also impose a minimum velocity separation between the AGN for detection. This reflects the need to detect separate narrow emission line features from both AGN in a single spectrum (broad lines would further complicate the separation of the lines). We note that we impose the limitations on the absolute separation or velocity difference between the AGN, not the projected quantity for different lines of sight. Our timescales and dual fractions therefore represent an upper limit to what is detectable with a given observational constraint.

Figure 4.7 shows the total time that dual AGN are observable as a function of BH separation, velocity offset, and luminosity ratio given observational constraints in the 1:2 prograde coplanar merger. If very low luminosity AGN are detectable (left panels), dual AGN are observable throughout much of the merger, preferentially at large spatial offsets and low velocity offsets. This reflects the fact that the two BHs spend most of their orbit near apocenter. At higher luminosities (right panels), the

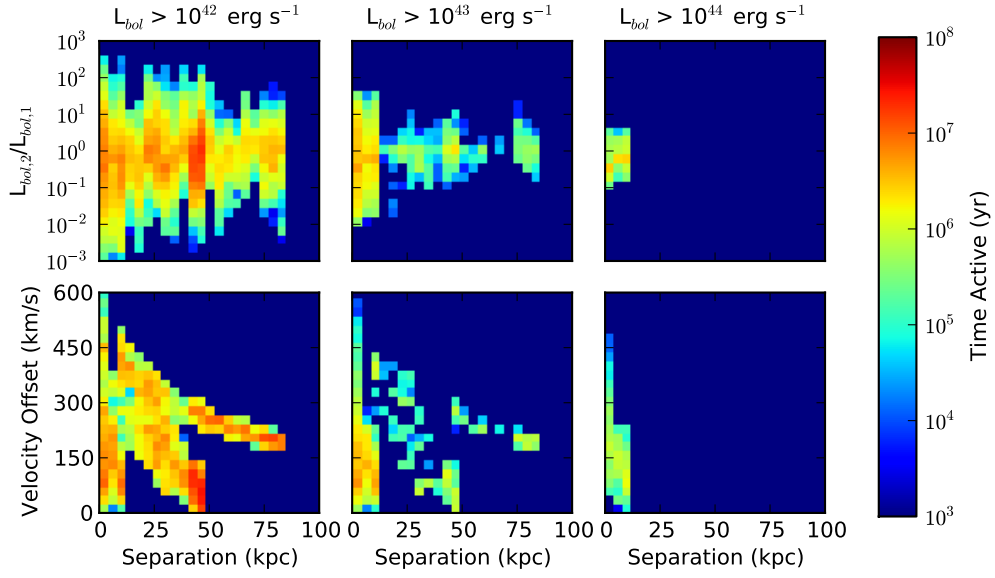


**Figure 4.8.** Dual AGN observability timescales in the 1:2 retrograde (primary) merger. Top panels: luminosity ratio between the two BHs as a function of BH separation when both BHs are accreting at the given luminosity. Bottom panels: velocity offset between the BHs as a function of separation when they are observable as a dual AGN. The color of each point indicates the total dual AGN timescale.

majority of the accretion is triggered by the dynamics of the merger. Dual AGN are observable only at low separations, reflecting AGN triggering near pericenter passages. We note that most accretion does not occur exactly at pericenter, when the velocity offset between the BHs is at its highest, but shortly after the pericenter passage, at moderate velocity offsets ( $\Delta v \leq 250 \text{ km s}^{-1}$ ).

For reference, we show also the dual AGN timescales in the 1:2 retrograde (primary) merger (Figure 4.8), where the total timescale at  $L > 10^{44} \text{ erg s}^{-1}$  is longest, and the 1:6 merger (Figure 4.9), which shows how the dual activity decreases with a smaller mass ratio. In the 1:2 retrograde (primary) merger, strong inflows following second pericenter produce dual AGN at larger spatial separations than in the 1:2 prograde coplanar merger, where the majority of dual AGN activity occurs following third pericenter. Figures for the remaining simulations are available in Appendix B.

In Table 4.2, we present the dual fractions for these three mergers as a function of the observational constraints. Here the dual fraction is defined as the dual AGN timescale divided by the total time when one or both AGN are visible with the given

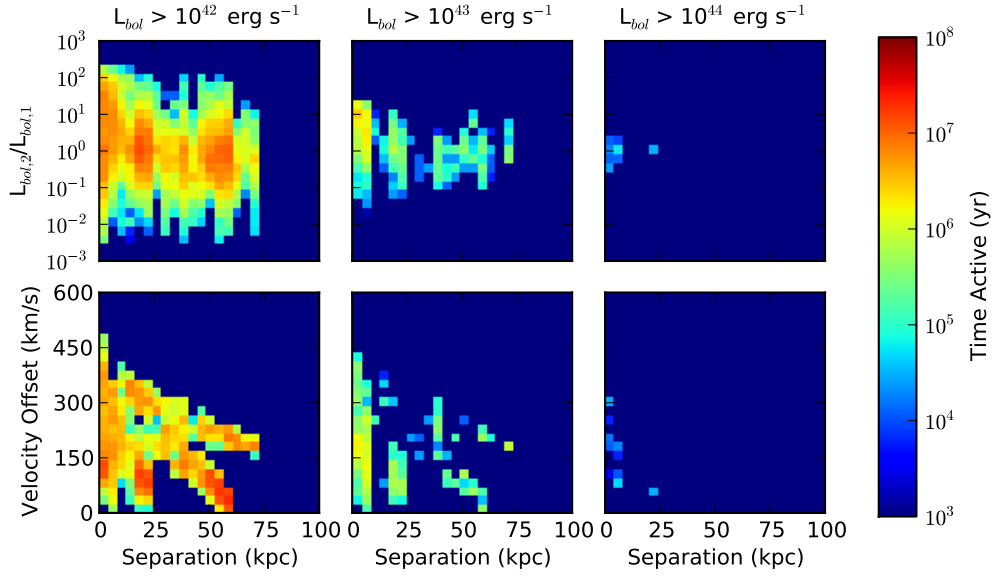


**Figure 4.9.** Dual AGN observability timescales in the 1:6 prograde coplanar merger. Top panels: luminosity ratio between the two BHs as a function of BH separation when both BHs are accreting at the given luminosity. Bottom panels: velocity offset between the BHs as a function of separation when they are observable as a dual AGN. The color of each point indicates the total dual AGN timescale.

constraints. This corresponds to the chance to observe a dual AGN in an interacting system given that one of the BHs is already active. Data for the remaining simulations are available in Appendix B. We consider three constraints on dual AGN detection to represent the limitations of surveys, requiring spatial separations above 1 kpc, spatial separations above 10 kpc, or velocity offsets above  $150 \text{ km s}^{-1}$  (for double peaked narrow emission line detections, Comerford et al., 2009a).

A substantial dual fraction (5-20 percent) remains in our major mergers even at high luminosities and accretion rates. However, survey limitations can substantially reduce the observable dual AGN fraction. We note again that the cutoffs are applied to the absolute separations and velocity offsets, so the values in Table 4.2 are upper limits. The  $d > 10 \text{ kpc}$  cutoff produces a large decrease in dual fraction because most strong accretion occurs late in the merger when the separation between the BHs is  $< 10 \text{ kpc}$ . Minor mergers, which occur more commonly than major mergers, have lower dual AGN fractions which are reduced further by the observational limitations of surveys.



| Simulation             | Threshold          | BH <sub>1</sub> | BH <sub>2</sub> | Dual Fraction | $d > 1$ kpc | $d > 10$ kpc | $\Delta v > 150$ km s <sup>-1</sup> |
|------------------------|--------------------|-----------------|-----------------|---------------|-------------|--------------|-------------------------------------|
| 1:2 Prograde Coplanar  | $L_{bol} > L_{42}$ | 77.8            | 64.9            | 57.6          | 53.4        | 43.9         | 35.7                                |
|                        | $L_{bol} > L_{43}$ | 21.2            | 15.3            | 16.3          | 13.5        | 5.61         | 8.23                                |
|                        | $L_{bol} > L_{44}$ | 2.68            | 2.61            | 19.2          | 16.5        | 0.10         | 4.76                                |
|                        | $f_{Edd} > 0.005$  | 59.9            | 63.0            | 49.3          | 45.9        | 36.8         | 31.1                                |
|                        | $f_{Edd} > 0.05$   | 11.1            | 14.2            | 13.8          | 11.8        | 3.99         | 6.51                                |
|                        | $f_{Edd} > 0.5$    | 1.47            | 2.26            | 18.5          | 17.2        | 0.07         | 3.44                                |
| 1:2 Retrograde (Prim.) | $L_{bol} > L_{42}$ | 78.3            | 68.3            | 59.3          | 56.5        | 47.1         | 33.1                                |
|                        | $L_{bol} > L_{43}$ | 29.9            | 15.4            | 18.3          | 14.3        | 4.2          | 7.4                                 |
|                        | $L_{bol} > L_{44}$ | 7.4             | 2.7             | 14.1          | 9.2         | 0            | 6.4                                 |
|                        | $f_{Edd} > 0.005$  | 64.2            | 66.1            | 50.2          | 47.7        | 39.2         | 27.7                                |
|                        | $f_{Edd} > 0.05$   | 17.8            | 14.4            | 15.9          | 11.6        | 2.2          | 6.6                                 |
|                        | $f_{Edd} > 0.5$    | 4.6             | 2.2             | 12.0          | 7.9         | 0            | 5.7                                 |
| 1:6 Prograde Coplanar  | $L_{bol} > L_{42}$ | 76.3            | 42.1            | 36.8          | 34.1        | 28.0         | 18.1                                |
|                        | $L_{bol} > L_{43}$ | 15.1            | 9.5             | 6.4           | 5.0         | 2.1          | 3.5                                 |
|                        | $L_{bol} > L_{44}$ | 0.71            | 1.7             | 0.38          | 0.3         | 0.06         | 0.18                                |
|                        | $f_{Edd} > 0.005$  | 54.6            | 60.5            | 40.4          | 37.7        | 33.1         | 20.2                                |
|                        | $f_{Edd} > 0.05$   | 6.5             | 16.9            | 4.4           | 3.9         | 2.6          | 2.5                                 |
|                        | $f_{Edd} > 0.5$    | 0.18            | 2.8             | 0.06          | 0.03        | 0            | 0.06                                |

**Table 4.2.** Dual AGN fractions for several simulations. The remaining data are in Appendix B.  $BH_1$  and  $BH_2$  represent the percentage of the entire simulation that each BH is active at the given observability threshold. The dual fraction is the total time when both AGN are active divided by the total time that one or both AGN are active, expressed as a percentage. The remaining columns give the dual fraction with additional constraints for observation.

### 4.3.2 Gas Poor Primary Galaxies

We briefly discuss mergers between gas rich secondary galaxies and gas poor primaries which resemble low redshift elliptical or Sa galaxies. We consider two 1:2 mergers, varying the gas content of the primary galaxy. We scale the mass of  $BH_1$  with the mass of the spheroid, which is the entire baryonic mass in these simulations.  $BH_1$  therefore has an initial mass of  $4 \times 10^7 M_\odot$  and is significantly more massive than the  $BH_2$ .

In our first merger, the primary galaxy does not contain any gas.  $BH_1$  is therefore unable to accrete until close to the second pericenter passage, when gas that was tidally stripped from the secondary galaxy reaches the center of the primary. The stripped gas flows directly down to the BH, driving strong accretion for much of the remaining merger. Since  $BH_1$  is an order of magnitude more massive than  $BH_2$ , it accretes at a higher luminosity once gas is available. At high luminosities, the overall dual AGN timescale and dual fraction are similar or smaller than in the mergers between spiral galaxies.

We also consider a merger where the primary galaxy begins with a hot gas halo with a similar spatial distribution to the stellar component and 5 percent of the

mass. Once scaled to  $z = 3$ , the dense gas halo quickly cools and forms a gaseous disk, leaving what resembles an Sa galaxy. The resulting disk in the primary is less dense than the secondary’s disk, but  $\text{BH}_1$  accretes with a high luminosity compared to  $\text{BH}_2$  simply due to its larger mass (recall that sub-Eddington accretion scales as  $M_{\text{BH}}^2$ , Equation 4.2). As a result of the continuous accretion onto  $\text{BH}_1$ , the dual AGN timescale is longer than in our 1:2 prograde coplanar spiral-spiral merger for  $L_{\text{bol}} > 10^{44} \text{ erg s}^{-1}$ , but the dual AGN fraction is actually lower. The dual AGN fraction is low because the continuous accretion of  $\text{BH}_1$  dilutes what dual AGN activity does occur.

In summary, we find that the accretion onto  $\text{BH}_1$  depends sensitively on the gas content and distribution in the primary galaxy. A relatively more massive central BH than in the spiral galaxies produces high luminosities once gas reaches the BH. However, the properties of gas poor galaxies at high redshift are not known, if they even exist. It is difficult, therefore, to meaningfully assess the impact of mergers containing gas poor primary galaxies that resemble low redshift elliptical galaxies. The results of these two simulations are included in Appendix B.

## 4.4 Discussion

Our results indicate that dual AGN should be preferentially found in the late stages of mergers between galaxies with similar masses. The majority of our high luminosity dual activity occurs following pericenter passages between our galaxies, suggesting that the best candidates for discoveries of dual AGN are closely separated galaxies that are strongly interacting. However, since small separations of order a few kpc are typically difficult to resolve, spectroscopy may be the most efficient technique for discovering such systems (Comerford et al., 2009a).

We note that we have not included the effects of dust obscuration, which may hinder detection of AGN in the optical, reducing the observed dual AGN fraction. Major mergers between gas rich galaxies can produce (ultra) luminous infrared galaxies, which have high levels of dust extinction (Sanders et al., 1988). We therefore expect that there will be significant obscuration in the late stages of our mergers where

the majority of the dual AGN activity occurs. Detection of obscured AGN in hard X-rays may be more favorable (Koss et al., 2011). Additionally, there is likely to be considerable variability in the AGN on unresolved timescales that would reduce the correlation in accretion between the BHs (Hopkins & Quataert, 2010; Levine et al., 2010).

Blecha et al. (2013) perform simulations of major mergers between redshift zero galaxies and model the narrow emission line regions that form as a result of BH accretion. They find that dual narrow line regions are created late in the mergers, when the BHs are at kpc scales and less. The overall dual AGN timescale in their mergers is at most several tens of Myr, in good agreement with our results for moderate and high luminosities and accretion rates. They consider 1:1, 1:2, and 1:3 mergers and note that the dual AGN phase is longer in equal mass mergers where gaseous inflows following close passages are strongest. Our results show that this trend continues in minor mergers, where the dual AGN timescale further decreases with mass ratio.

### **Observational Surveys of Dual AGN**

Liu et al. (2011) study the AGN pair fraction of AGN drawn from SDSS. They select only AGN pairs with projected separations of  $5 < r_p < 100$  kpc drawn from a sample of AGN with strong emission line detections and require spatially resolved spectroscopy of each galaxy separately, i.e. they specifically avoid the case of double narrow emission line features in a single spectrum. They do this to circumvent the biases of double emission line surveys in SDSS, which are biased against dual AGN with  $\Delta v < 150$  km s<sup>-1</sup> or projected separations above a few kpc (as both AGN must appear in the same SDSS fiber). Liu et al. are therefore biased against AGN pairs with small projected separations which would lead to double narrow emission line features. They find that the fraction of AGN pairs at the aforementioned separations is 3.6 percent once they correct for spectroscopic incompleteness. It is difficult for us to directly compare our results to this AGN pair fraction, since our dual fraction calculations only include interacting systems by definition. Instead, we suggest that the separations they probe would miss the majority of the strong dual AGN we see

in our simulations, which are triggered primarily on scales of a few kpc. Liu et al. estimate the fraction of double-peaked narrow emission line systems that are caused by mergers to be  $\simeq 10 - 40$  percent. We note that this estimate depends on their assumption that the dual AGN fraction does not evolve significantly with the separation between the galaxies. Our results show a strong dependence on the separation between the galaxies, suggesting that a higher fraction of double-peaked narrow line AGN are caused by merging systems.

We also discuss our results in comparison to those of Koss et al. (2012). Koss et al. study the dual fraction of 167 AGN detected by the Swift Burst Alert Telescope (BAT). From the sample of BAT AGN, they search for companion galaxies and, when a companion is found, signs of AGN activity in the optical and X-ray bands. They find that 81 of the BAT AGN have companion galaxies on scales less than 100 kpc. This sample of 81 galaxy pairs, in which at least one AGN has already been detected, forms a close analogue to the dual fractions that we calculate (Table 4.2). They find evidence of an AGN in 16 of companion systems, producing a dual fraction for interacting systems of 19.8 percent. We note that we cannot draw a direct comparison between our dual fractions and those of Koss et al., given the different environments we are probing (low vs. high redshift), but a dual fraction of  $\simeq 20$  percent is similar to the dual fractions we find for moderate and high luminosity AGN ( $L_{\text{bol}} > 10^{43}$  erg  $\text{s}^{-1}$ ) in our 1:2 mergers. Indeed, Koss et al. find that the mean stellar mass ratio in their interacting galaxies is 2.1.

We note good agreement with several other findings of Koss et al. (2012). They break down their sample of dual AGN into different groups by mass ratio and separation. Their smallest separation bin, holding galaxy pairs with separations of 1 – 15 kpc, has a dual fraction of 50 percent, suggesting that dual AGN are driven by closely interacting galaxies. They also find an increase in the X-ray luminosity of the AGN in close galaxy pairs. Our simulations show that the strongest, best correlated accretion between the BHs occurs when the galaxies are closely separated, just following a pericenter passage. Finally, Koss et al. note that the dual fraction of their sample increases for mass ratios near one, in agreement with our results.

## 4.5 Conclusions

We have performed numerical simulations of unequal mass galaxy mergers, focusing on the dynamics of merger triggered AGN. We find that high accretion rates are driven by gaseous inflows, bars, and the re-formation of gaseous disks from stripped gas, all occurring late in the merger when the separation between the galaxies is small. As the mass ratio of the merger decreases, the primary galaxy is less perturbed throughout the merger and BH<sub>1</sub> settles into low level, quiescent accretion. The secondary galaxy, on the other hand, experiences stronger tidal torques, but overall accretion onto BH<sub>2</sub> is limited by ram pressure stripping from the primary’s disk. Nonetheless, the strong inflows in the secondary galaxy lead BH<sub>2</sub> to grow more relative to BH<sub>1</sub>, increasing their mass ratio. Overall, our galaxy mergers lead to strong AGN triggering. In the early phases of our mergers, both BHs grow quiescently, increasing in mass by 20-40 percent over more than a Gyr of evolution. Once the dynamics of the merging galaxies drive gaseous inflows, however, the BHs accrete much more efficiently, growing by up to a factor of two over the course of several hundred Myr. We note, however, that low mass ratio mergers do not lead to strong accretion onto BH<sub>1</sub>. We find that minor mergers are only likely to increase the mass of BH<sub>1</sub> in the event of a successful BH-BH merger, as BH<sub>1</sub> otherwise accretes as if its host was evolving in isolation.

We also considered the occurrence of simultaneous accretion onto both BHs, resulting in a dual AGN. Very low luminosity dual AGN ( $L_{\text{bol}} > 10^{42}$  erg s<sup>-1</sup>) occur throughout each merger, representing random overlap between the BH accretion rates. They are found preferentially at large separations between the galaxies, near apocenter, where the galaxies spend most of their time. High accretion rates ( $L_{\text{bol}} > 10^{44}$  erg s<sup>-1</sup>) limit dual AGN activity instead to small separations between the galaxies, when their interaction drives strong, correlated accretion in both BHs, although significant non-simultaneous accretion always remains. In low mass ratio mergers, the weak response of the primary galaxy to the merger limits the dual AGN observability timescale. We therefore find that dual AGN are preferentially powered by mergers where the galaxies are similar in mass. We compare our numerical findings on dual

AGN to observations by Koss et al. (2012) and find excellent agreement.

## CHAPTER 5

# Massive Black Holes in Milky Way Satellites

### 5.1 Introduction

Observed scaling relations indicate a correlation between the masses of supermassive BHs and the properties of their hosts (Magorrian et al., 1998; Ferrarese & Merritt, 2000; Gebhardt et al., 2000; Marconi & Hunt, 2003; Häring & Rix, 2004). However, these relations are well established only for BHs with masses in the range  $10^7 - 10^9 M_\odot$  (Gültekin et al., 2009). Greene et al. (2010) present a sample of BH masses in the range  $10^6 - 10^7 M_\odot$  from megamaser detections and find increased scatter relative to the  $M_{\text{BH}} - \sigma$  relation of Gültekin et al. (2009), suggesting that the scaling relations may be less tight for lower mass systems. In particular, Greene et al. find increased scatter towards lower  $M_{\text{BH}}$  for a given velocity dispersion. This population of undermassive BHs is also seen in the models of Volonteri & Natarajan (2009). They predict a population of BHs in galaxies that have grown mostly through minor mergers that do not efficiently grow their BHs, leaving them undermassive compared to the host galaxy.

There are also significant non-detections of BHs in a few nearby galaxies from stellar-dynamical observations, most notably the Local Group Scd-type spiral galaxy M33, in which the upper limit to  $M_{\text{BH}}$  is just a few thousand solar masses (Gebhardt et al., 2001; Merritt et al., 2001). Similarly, in the Local Group dwarf elliptical galaxy NGC 205,  $M_{\text{BH}} < 3.8 \times 10^4 M_\odot$  (Valluri et al., 2005). These results suggest that the BH occupation fraction (the fraction of galaxies at a given mass that contain BHs) in low-mass galaxies might be significantly below unity, but at present it is not possible to carry out measurements of similar sensitivity for galaxies much beyond the limits of

the Local Group (Ibata et al., 2009; Lora et al., 2009; Greene & Ho, 2007; Debattista et al., 2006).

These results suggest that the presence and masses of BHs in low mass galaxies is less certain than in massive galaxies ( $\sigma > 100 \text{ km s}^{-1}$ ). In the galaxy mergers considered in Chapters 2, 3, and 4, we initialize our galaxies assuming that they contain central BHs that follow local ( $z = 0$ ) scaling relations. Our mergers include BH masses ranging down to  $3 \times 10^5 M_{\odot}$ , below the BH masses that are well studied. To understand the BH population in these low mass galaxies, however, we must consider the entire cosmological history of the galaxy, including the possible formation of ‘seed’ BHs at high redshift in the galaxy’s progenitors.

Here we consider the cosmological history of a Milky Way-sized halo, focusing on the BH population of dwarf galaxies hosted by the main halo at  $z = 0$ . We explore theoretical expectations for the probability that a dwarf galaxy hosts an BH, and if the merging and accretion history in dwarf galaxies leads to different scaling relationships of BHs with their hosts (i.e. deviations from the scaling relations for high mass galaxies). We consider three different BH seed populations, formed at high redshift, and address the question of whether the detection of the BH population of dwarf galaxies may be able to distinguish among different BH formation mechanisms. Our results were originally presented in van Wassenhove et al. (2010) and are reproduced here with permission of the MNRAS.

## 5.2 Massive black hole formation and dynamical evolution

We follow the formation and evolution of an BH population in a Milky Way-size halo in a  $\Lambda$ CDM universe (Dunkley et al., 2009). Our technique follows that of Volonteri et al. (2003), as we use Monte Carlo realizations of the merger histories of dark matter halos. We analyse here 5 different realizations of halos that reach a mass of  $M_h = 2 \times 10^{12} M_{\odot}$  at  $z = 0$ . We seed the high-redshift progenitor halos with black holes and follow them from formation to  $z = 0$ . We focus on the signatures of black hole formation efficiency in satellite galaxies surviving until today.



### 5.2.1 Massive black hole formation models

We adopt three different models to seed haloes with black holes: massive seeds and two Population III remnant seed models. These models determine which haloes are seeded with black holes at high redshifts. They also set a minimum mass for central BHs today.

#### Population III remnants

For the Population III remnant models, we follow two schemes that differ only in the efficiency of BH seed formation. We assume here that BHs form as end-product of the very first generation of stars. The main features of a scenario for the hierarchical assembly of BHs left over by the first stars in a  $\Lambda$ CDM cosmology have been discussed by Volonteri et al. (2003), Volonteri & Rees (2006) and Volonteri & Natarajan (2009). The first stars are believed to form at  $z \sim 20 - 30$  in minihalos,  $M_{\min} \approx 10^6 M_{\odot}$ , above the cosmological Jeans mass. They collapse at  $z \sim 20 - 50$  from the rarest  $\nu$ - $\sigma$  peaks of the primordial density field. In this regime, cooling is possible by means of molecular hydrogen ( $T_{\text{vir}} > 2 - 3 \times 10^3$  K, Tegmark et al., 1997; Yoshida et al., 2006), but the inefficient cooling at zero metallicity might lead to a very top-heavy initial stellar mass function. Specifically, the earliest-forming stars are likely to have been very massive (Carr et al., 1984; Bromm et al., 1999, 2001; Abel et al., 2000; Yoshida et al., 2006). If stars form above  $260 M_{\odot}$ , they rapidly collapse to massive black holes with little mass loss (Fryer et al., 2001), leaving behind seed BHs with masses  $M_{\text{BH}} \sim 10^2 - 10^3 M_{\odot}$  (Madau & Rees, 2001). We consider that BH seeds populate haloes with formation redshift  $z > 12$  which represent density peaks with  $\nu_c = 3$  ('peak3'; as a reference:  $M_{\text{h}} > 10^5 M_{\odot}$  at  $z = 20$ , and  $M_{\text{h}} > 10^8 M_{\odot}$  at  $z = 12$ ) or  $\nu_c = 3.5$  ('peak3.5'; as a reference:  $M_{\text{h}} > 10^6 M_{\odot}$  at  $z = 20$ , and  $M_{\text{h}} > 10^9 M_{\odot}$  at  $z = 12$ ), while also requiring that  $T_{\text{vir}} \gtrsim 2500$  K to ensure effective  $\text{H}_2$  cooling (implying masses above  $3 \times 10^6 M_{\odot}$ ). In this model, seeds form as  $100 M_{\odot}$  black holes.

## Massive BH seeds

The massive seed model relies instead on the collapse of supermassive objects formed directly out of dense gas (Koushiappas et al., 2004; Begelman et al., 2006; Lodato & Natarajan, 2006, and references therein), where the mass inflow is regulated by the degree of stability of the cooling gas. Here we assume that gas is accumulated in the centre of a halo via viscous instabilities. A dynamically unstable disk can develop non-axisymmetric spiral structures that effectively redistribute angular momentum, causing mass inflow. This process stops when the amount of mass transported to the centre is enough to make the disc marginally stable. We here follow Lodato & Natarajan (2006), who suggest that the mass inflow can be computed from the Toomre stability criterion and from the disc properties, determined from the dark matter halo properties (halo mass,  $M_h$ , virial temperature,  $T_{\text{vir}}$  and spin parameter,  $\lambda$ ; Mo et al., 1998). We refer the reader to Lodato & Natarajan (2006); Volonteri et al. (2008b) for a comprehensive description. We summarize here the main features of the model, and how we operationally implement it.

Consider a dark matter halo of mass  $M_h$  and virial temperature  $T_{\text{vir}}^1$ , containing a gas mass in cold gas  $M_{\text{gas}} = f_d M_h$  (we assume that the gas fraction cooling is roughly 5% implying  $f_d = 0.05$ , Mo et al. 1998). The other main parameter characterizing a dark matter halo that is relevant here is its spin parameter  $\lambda$  ( $\equiv J_h E_h^{1/2} / G M_h^{5/2}$ , where  $J_h$  is the total angular momentum and  $E_h$  is the binding energy). The distribution of spin parameters for dark matter halos measured in numerical simulations is well fit by a lognormal distribution in  $\lambda_{\text{spin}}$ , with mean  $\bar{\lambda}_{\text{spin}} = 0.05$  and standard deviation  $\sigma_\lambda = 0.5$  (e.g., Bullock et al. 2001; van den Bosch et al. 2002; Macciò et al. 2008).

If the virial temperature of the halo  $T_{\text{vir}} > T_{\text{gas}}$ , the gas collapses and forms a rotationally supported disc. For metal-free gas, the cooling function is dominated

---

<sup>1</sup>A halo at redshift  $z$  is uniquely characterized by a virial radius  $r_{\text{vir}}$ , defined as the radius of the sphere encompassing a mean mass overdensity  $\delta_{\text{vir}}$ .  $\delta_{\text{vir}} \approx 178$  in an Einstein-de Sitter Universe. Detailed calculations for different cosmologies (e.g.,  $\Lambda$ CDM) can be found in Lacey & Cole (1993) and Eke et al. (1996). From the virial theorem the virial mass,  $M_h$  can be calculated straightforwardly, along with the circular velocity,  $V_c = \sqrt{G M_h / r_{\text{vir}}}$  and virial temperature  $T_{\text{vir}} = \mu m_p V_c^2 / (2k_B)$ , where  $\mu \simeq 0.722$  is the mean molecular weight,  $m_p$  is the proton mass and  $k_B$  is the Boltzmann constant.

by hydrogen. In thermal equilibrium, if the formation of molecular hydrogen is suppressed (see the discussion in Devecchi & Volonteri 2009), these discs are expected to be nearly isothermal at a temperature of a few thousand Kelvin (here we take  $T_{\text{gas}} \approx 5000\text{K}$ , Lodato & Natarajan 2006). For low values of the spin parameter  $\lambda$ , the resulting disc can be compact and dense and is subject to gravitational instabilities. This occurs when the Toomre stability parameter  $Q$  approaches a critical value  $Q_c$  of order unity (following Volonteri et al. 2008 we adopt  $Q_c = 2$ , in order to match observational constraints on the BH and quasar population). If the destabilization of the system is not too violent, instabilities lead to mass infall instead of fragmentation into bound clumps and global star formation in the entire disc (Lodato & Natarajan, 2006). This is the case if the inflow rate is below a critical threshold  $\dot{M}_{\text{max}} = 2\alpha_c \frac{c_s^3}{G}$  that the disk is able to sustain (where  $\alpha_c \sim 0.12$  describes the viscosity, Rice et al., 2005) and molecular and metal cooling are not important.

This mass redistribution process ceases when the amount of mass transported to the center,  $M_a$ , is enough to make the disc marginally stable. This can be computed easily from the Toomre stability criterion and disc properties, determined from the dark matter halo mass and angular momentum (Mo et al., 1998):

$$M_a = \begin{cases} m_d M_h \left[ 1 - \sqrt{\frac{8\lambda}{m_d Q_c} \left(\frac{j_d}{f_d}\right) \left(\frac{T_{\text{gas}}}{T_{\text{vir}}}\right)^{1/2}} \right] & \lambda < \lambda_{\text{max}} \\ 0 & \lambda > \lambda_{\text{max}} \end{cases}$$

where

$$\lambda_{\text{max}} = f_d Q_c / 8 (f_d / j_d) (T_{\text{vir}} / T_{\text{gas}})^{1/2} \quad (5.1)$$

is the maximum halo spin parameter for which the disc is gravitationally unstable, and  $j_d$  is the fraction of the halo angular momentum retained by the collapsing gas ( $j_d = f_d$  if specific angular momentum is conserved).

For large halo masses, the internal torques needed to redistribute the excess baryonic mass become too large to be sustained by the disc, which then undergoes fragmentation. This occurs when the virial temperature exceeds a critical value  $T_{\text{max}}$ ,

given by:

$$\frac{T_{\max}}{T_{\text{gas}}} = \left( \frac{4\alpha_c}{f_d} \frac{1}{1 + M_{\text{BH}}/f_d M_h} \right)^{2/3}. \quad (5.2)$$

To summarize, every dark matter halo is characterized by its mass  $M_h$  (or virial temperature  $T_{\text{vir}}$ ) and by its spin parameter  $\lambda$ . The latter is drawn from a lognormal distribution in  $\lambda_{\text{spin}}$  with mean  $\bar{\lambda}_{\text{spin}} = 0.05$  and standard deviation  $\sigma_\lambda = 0.5$  (Macciò et al., 2007, and references therein). The gas has a temperature  $T_{\text{gas}} = 5000\text{K}$ . If  $\lambda < \lambda_{\max}$  (see Eq 5.1) and  $T_{\text{vir}} < T_{\max}$  (Eq. 5.2), then we assume that a seed BH of mass  $M_{\text{BH}} = M_a$  given by Equation 5.1 forms in the center.

The gas made available in the central compact region can then form a central massive object, for instance via the intermediate stage of a ‘supermassive’ star (Hoyle & Fowler, 1963; Baumgarte & Shapiro, 1999), or a ‘quasistar’ (an initially low-mass black hole rapidly accreting within a massive, radiation-pressure-supported envelope, see also Begelman et al., 2006, 2008). Hence, the black hole seed mass estimates based on Equation 5.1 should be considered as upper limits. We here consider that BH seeds with  $M_{\text{BH}} \simeq M_a$  can form in haloes with formation redshift  $z > 12$  that satisfy all the above criteria. The mass function of seeds peaks at  $10^5 - 10^6 M_\odot$  (see Figure 2 in Volonteri et al., 2008b).

This process is effective for halos with low angular momentum (low spin parameter,  $\lambda \lesssim 0.01$ ) and zero metallicity, where cooling is driven by atomic hydrogen cooling and the difference between gas and virial temperature is small (making the disc resilient to global fragmentation and star formation). The efficiency of the seed assembly process ceases at large halo masses ( $T_{\text{vir}} > 1.4 \times 10^4 \text{ K}$ ), where the mass-accretion rate from the halo is above the critical threshold for fragmentation and the disc undergoes global star formation instead.

### 5.2.2 Massive black hole and galaxy evolution

To study the BHs at  $z = 0$ , we follow the evolution of the black holes along with their host galaxies using models that track both black hole mergers and accretion. Several recent works point out how fragile the environment of low-mass galaxies is (Bovill & Ricotti, 2009, and references therein). The shallow potential well of these galaxies

makes it easy for gas to evaporate or escape in the presence of feedback or dynamical heating. We incorporate a simple scheme that tracks the gaseous content of galaxies and the effect of gas depletion on BH growth and dynamical evolution.

### **Halo baryon content**

We track the baryon content of haloes using a method similar to that developed by Okamoto et al. (2008). They present a simple model that reproduces the results of cosmological hydrodynamical simulations of mass loss from a UV background. In this model, haloes form at high redshifts with the cosmic mean baryon fraction,  $f_b = 0.18$  (Dunkley et al., 2009). We define the baryon fraction as the ratio between the mass in baryons and the total mass of a halo. After reionization (set at  $z = 9$  here), low mass haloes lose their baryons as a result of the increased temperature of the intergalactic medium (IGM) (Gnedin, 2000). The condition for baryon loss depends on the relation of the virial temperature of the halo,  $T_{\text{vir}}$ , to the temperature at which photoheating and radiative cooling are balanced,  $T_{\text{eq}}$ . We evaluated  $T_{\text{eq}}$  at an overdensity,  $\Delta_{\text{evp}} = 10^6$ , representing the densest, most bound region of the halo (see Okamoto et al., 2008, for a discussion of the model parameters and the allowed range). If the equilibrium gas temperature in these dense regions is greater than the virial temperature of the halo, the gas will evaporate out of the halo into the surrounding IGM. In more massive haloes, the dense gas is able to cool efficiently, preventing it from evaporating. We model  $T_{\text{eq}}$  using the UV background by Haardt & Madau (1996). Halos with  $T_{\text{vir}} < T_{\text{eq}}(\Delta_{\text{evp}})$  have a mass in baryons,  $M_b$ , which decreases with time, given by:

$$M_b(t + \delta t) = M_b(t) e^{-\frac{\delta t}{t_{\text{evp}}}}. \quad (5.3)$$

The evaporation time-scale,  $t_{\text{evp}}$ , is given by  $R_{\text{vir}}/c_s(\Delta_{\text{evp}})$ , where  $R_{\text{vir}}$  is the virial radius of the halo, and  $c_s(\Delta_{\text{evp}})$  is the sound speed at the evaporation overdensity. This timescale corresponds to the time for gas to leave the halo moving at the sound speed.

We additionally allow for accretion of baryons from the IGM onto haloes. If gas

at the outskirts of the halo is colder than the virial temperature of the halo, the halo accretes enough baryons to reach the cosmic mean. Here the temperature of the accreting gas is approximated as the equilibrium temperature of gas with density  $\rho_{\text{vir}}/3$ . This density corresponds to the density of gas at the virial radius of the halo. The requirement for accretion up to the cosmic mean baryon fraction is expressed  $T_{\text{eq}}(\rho_{\text{vir}}/3) < T_{\text{vir}}$ . When the halo is colder than the gas in the surrounding IGM, no accretion occurs. When two haloes merge in our model, the resulting halo has a mass in baryons equal to the sum of the baryonic masses of the progenitor haloes.

### Massive black hole accretion

Based on simulations of BH mergers in galaxies with different gaseous content (Callegari et al., 2009), we assume that black holes hosted by a baryon rich halo experiencing a major merger (mass ratio greater than 1:10) accrete mass from the host. We here define a halo as baryon rich when it has retained more than half of its original baryon fraction. Specifically, we choose a baryon fraction threshold  $f_b > 0.1$ . In this simple treatment, a merged black hole accretes mass according to the central velocity dispersion of the host  $M_{bh} = 10^8(\sigma/200 \text{ km s}^{-1})^4 M_{\odot}$  (e.g., Tremaine et al., 2002). We link the central velocity dispersion to the circular velocity of the halo using the empirical relationship  $\log(V_c) = 0.74 \log(\sigma) + 0.8$  (Pizzella et al., 2005). The correlation between central velocity dispersion and halo circular velocity has been studied observationally for samples of galaxies mostly in the range  $\sigma \gtrsim 70 \text{ km s}^{-1}$  (Ferrarese, 2002; Baes et al., 2003). Pizzella et al. (2005) extend the study to  $\sigma \sim 40 \text{ km s}^{-1}$ , but extending these studied to the range of dwarf galaxies is challenging, as the stars may not reach the radius where the halo has its maximum circular velocity (e.g., see Fig 5 of Peñarrubia et al., 2008). Since there is no accepted relationship between  $V_c$  and the central velocity dispersion that extends down the the dwarf galaxy sizes considered here, we use the above relationship to determine BH masses from the halo velocity dispersion. For dynamical evolution of the satellites, we use the definition  $\sigma = V_c/\sqrt{3}$ , as the velocity dispersions quoted in the literature that we need to assess our dynamical modelling are obtained from the ‘global’ velocity sample in each galaxy, not

just from some innermost sub-sample. At present the only dwarf spheroidal (dSph) satellite with maximum circular velocity constrained by data (and assuming constant velocity anisotropy) is Fornax, with global velocity dispersion  $\sigma \simeq 11 \text{ km s}^{-1}$  and  $V_c \sim 18 \text{ km s}^{-1}$  (Walker et al., 2009a), consistent with the  $\sigma = V_c/\sqrt{3}$  scaling. We note that our overall results are robust to changes in the assumed scaling between  $V_c$  and  $\sigma$ . We have run models where we also adopt the relationship  $\sigma = V_c/\sqrt{2}$  to calculate BH masses, and qualitatively all results hold.

The total mass of the black hole resulting from a completed merger is the sum of the merging black hole masses and any accreted mass. When a halo with a central black hole merges with an empty halo, the central black hole will accrete mass after the merger timescale if the halo remains baryon rich. A similar scheme has been shown to reproduce observational constraints on BH evolution (luminosity function of quasars and Soltan’s argument,  $M_{\text{BH}} - \sigma$  relationship at  $z = 0$ , mass density in BHs at  $z = 0$ ; Volonteri et al., 2008b) for the ‘peak3.5’ and ‘massive seeds’ models.

### 5.2.3 Dynamical evolution of satellites and massive black holes

As shown by several investigations (e.g., Madau et al., 2008; Tollerud et al., 2008; Macciò et al., 2010; Muñoz et al., 2009) the population of dark matter satellites found in numerical simulations exceeds by a large degree the number of known satellites of the Milky Way, creating a “missing satellite” problem. It has been advocated that the solution to this problem may lie in a combination of factors. On the one hand, cooling and star formation are inefficient in the presence of a strong photoionizing background, which prevents the development of an observable luminous component. On the other hand, tidal stripping of the satellites orbiting in the potential of the Milky Way may cause mass loss, leading to systems much less massive than they were at the time that they merged with their host halo. In this section, we first describe how we model the dynamical evolution of satellites in the Milky Way halo in order to derive the properties of the sub-population of luminous satellites that have survived until today. We then address the dynamical evolution of BH pairs formed during galaxy mergers.

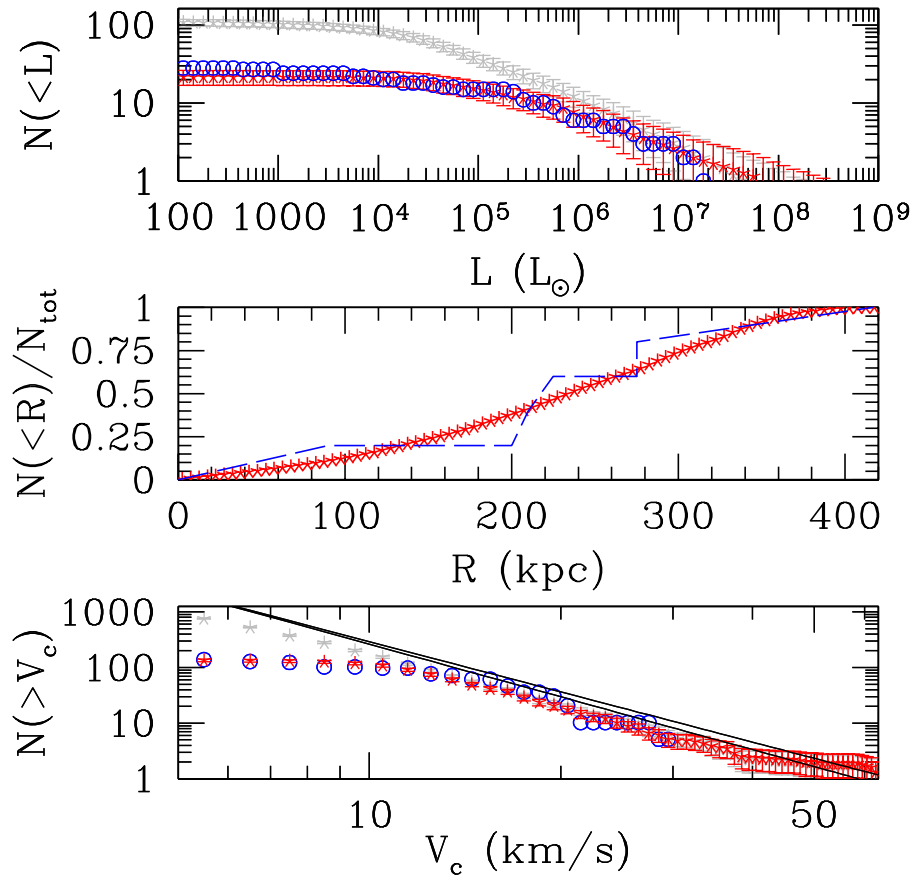


**Figure 5.1.** Top panel: luminosity function of satellite galaxies, corrected to match the SDSS DR5 selection. Upper grey curve with error-bars: full sample of simulated galaxies surviving tidal stripping. Lower red curve with error-bars: galaxies with baryon fraction  $> 7.5 \times 10^{-3}$ . Blue circles: observed luminosity function of Milky Way satellites. Middle panel: cumulative radial distribution of our simulated satellite population (dashed line: from Tollerud et al. 2008, fig. 5. ‘DR5’ distribution). Bottom panel: cumulative velocity distribution of our simulated satellite population compared to the fit derived for satellites in Via Lactea I (lower line, Diemand et al. 2007) and Aquarius (upper line, Springel et al. 2008). Circles: observed dwarf spheroidal satellites of the Milky Way. Errorbars are  $1-\sigma$  Poissonian errors.



## Dynamical evolution of satellites

After a halo merger, the smaller halo becomes a satellite of the more massive system. These satellite haloes evolve in the potential well of the host until  $z = 0$ , experiencing tidal stripping and possibly merging with the host.

We model the dynamical evolution of satellites within the host halo potential using analytical techniques (Volonteri et al., 2008a). For each satellite that merges with the main halo of the merger tree, we evolve the satellite-host system by integrating the equation of motion of the satellite in the gravitational potential of the host (assuming spherical NFW profiles; Navarro et al., 1997), including the dynamical friction term:

$$\frac{d^2\vec{r}}{dt^2} = -\frac{GM(r)}{r^2}\vec{r} - \frac{4\pi G^2 \ln \Lambda \rho M_{\text{sat}}}{v^2} f(x) \vec{v} \quad (5.4)$$

where  $f(x) \equiv [\text{erf}(x) - (2x/\sqrt{\pi})e^{-x^2}]$ ,  $x \equiv v/\sqrt{2}\sigma$ , and the velocity dispersion  $\sigma$  is derived from the Jeans' equation for the composite density profile, assuming isotropy (e.g. Binney & Tremaine 2008). Here  $M(r)$  is the total mass of the host within  $r$ ,  $\rho(r)$  is the total density profile, and the second term represents dynamical friction against the background. We include the BH keplerian potential if the galaxies host a BH. The Coulomb logarithm,  $\ln \Lambda$ , in equation (5.4) is taken equal to 2.5 (Taylor & Babul, 2001).

The mass of the satellite evolves during the integration because of tidal stripping. At every step of the integration we compare the mean density of the satellite to the mean density of the host halo at the location of the satellite. Tidal stripping occurs at the radius within which the mean density of the satellite exceeds the density of the galaxy interior to its orbital radius (Taylor & Babul, 2001). We trace the orbital evolution and the tidal stripping of all satellites from the time when the satellite enters the virial radius of the host to  $z = 0$ . Satellites that survive until the present time provide an analogue of the dwarf galaxy population around the Milky Way.

We compare the circular velocity and radial distribution of our satellite population to that of Via Lactea and Aquarius simulations (Diemand et al., 2007; Madau et al., 2008; Springel et al., 2008) and with constraints derived from the observed populations

(Tollerud et al., 2008; Kopolov et al., 2008; Walsh et al., 2009). Figure 5.1 compares our results to the literature. We find good agreement with the circular velocity distribution of satellites in the Aquarius simulation at  $z = 0$  at velocities above  $V_{max} > 10 \text{ km s}^{-1}$ .

We further derive the luminosity function of the satellites by assigning a luminosity based on their velocity dispersion. We adopt an empirical correlations derived by Kormendy & Freeman (2004) for galaxies with velocity dispersion  $\sigma > 30 \text{ km s}^{-1}$ :

$$\log(L_V/L_\odot) = 7.80 + 5 \log(\sigma/30 \text{ km s}^{-1}). \quad (5.5)$$

We perform a least square fit in  $\log(L_V)$  vs  $\log(\sigma)$  for low  $\sigma$  systems (using data from Mateo (1998), Simon & Geha (2007) and Walker et al. (2009b)) we find a very similar relationship ( $\log(L_V/L_\odot) = (7.6 \pm 0.6) + (4.3 \pm 0.9) \log(\sigma/30 \text{ km s}^{-1})$ ), albeit with a larger scatter. We therefore adopt the fit in Equation 5.5 for the whole  $\sigma$  range. To derive the luminosity function we need to set one single parameter, that is the minimum baryon fraction that allows star formation. We find the best fit to the observed luminosity function by considering as ‘luminous’ only those satellites with a baryon fraction  $> 7.5 \times 10^{-3}$  (the acceptable range is  $6.5 \times 10^{-3} < f_b < 8 \times 10^{-3}$ ). To compute the luminosity function, we follow Madau et al. (2008) in correcting our theoretical sample to match the SDSS DR5 sample of satellites. First, we correct the sample by a factor  $f_{\text{DR5}} = 0.194$  that takes into account the sky coverage. We then apply a joint distance-magnitude cut (Kopolov et al., 2008; Tollerud et al., 2008) ensuring that we count only satellites within the SDSS completeness limit:

$$r_{\text{max}} = \left( \frac{3}{4\pi f_{\text{DR5}}} \right)^{1/3} 10^{(-0.6M_V - 5.23)/3} \text{ Mpc}. \quad (5.6)$$

We use the central black holes of this population of haloes to provide observational signatures of black hole formation and growth efficiency. We note that stripping sometimes (a few per cent of the cases) leaves some ‘naked’ BHs, as the host loses most of its mass.

## Dynamical evolution of massive black holes

Along the dynamical evolution of the BH+galaxy systems, we further must determine the fate of the BHs they contain (if any). Work by Callegari et al. (2009) has shown that the efficiency of black hole pairing is a function both of the mass ratio and the baryon fraction of the merging haloes. Black holes in merging disc galaxies form a bound pair when the mass ratio of the merging galaxies is larger than 1:10 and galaxies are gas-rich (i.e., cold gas represents 10 per cent of the disc mass). We therefore define a major merger to be a merger between haloes with mass ratio greater than 1:10. In our models, minor mergers (mass ratio less than 1:10) do not lead to efficient black hole pairing and mergers. When a major merger occurs, the final fate of the BHs depends on the baryon content of the host. There is insufficient dynamical friction in gas-poor galaxies to lead to efficient BH pairing. We assume that black hole mergers stall when occurring in a baryon poor halo ( $f_b < 0.1$ ). Unless stalled, we assume that black holes merge within the merger timescale of their host galaxies. For major mergers, this timescale is well approximated by  $\tau_{\text{merge}}/\tau_{\text{dyn}} \simeq 0.4(M_{\text{host}}/M_{\text{sat}})^{1.3}/\ln(1 + M_{\text{host}}/M_{\text{sat}})$ , as shown by Boylan-Kolchin et al. (2008), where  $\tau_{\text{dyn}}$  is the dynamical time at the virial radius. This timescale represents a lower limit to the BH-BH merger time (Begelman et al., 1980), although the assumption that BHs merge within the merger timescale of their hosts is likely for BH pairs formed after gas rich galaxy mergers (Escala et al., 2005; Dotti et al., 2007). We study the time to the formation of a BH binary in more detail in Chapter 3.

### 5.3 Black hole occupation fraction and mass scaling

We study the black hole population of satellites at  $z = 0$  to find signatures of the black hole properties and seed efficiency. We show the black hole occupation fraction (BHOF) of the satellite population at  $z = 0$  in Figure 5.2. Massive satellites today were likely to have massive progenitors at high redshifts, meaning that they are more likely to host central black holes, given that a minimum mass threshold is required in all our models (mimicking the necessity of a deep potential well). The higher

the threshold mass, the more the BHOF is expected to decrease with the mass (or velocity dispersion) of today’s host. As expected, the more biased scenario ‘peak3.5’ leads to a lower overall BHOF than ‘peak3’. The ‘massive seed’ scheme produces fewer black holes than either ‘peak3’ or ‘peak3.5’. This is because of the stricter conditions needed for BH formation: seeds form only in very massive halos ( $M_h \simeq 10^8 M_\odot$ , compared to the much lower mass threshold for the Population III remnant case,  $M_h \sim 10^7 M_\odot$  at  $z = 15$  for ‘peak3’ and  $M_h \sim 7 \times 10^7 M_\odot$  for ‘peak3.5’) with low angular momentum (low spin parameter). Given that spin parameters appear to be distributed lognormally (with mean  $\bar{\lambda}_{\text{spin}} = 0.05$  and standard deviation  $\sigma_\lambda = 0.5$ ) in halos extracted from cosmological simulations, typically only  $\sim 10$  per cent of the haloes in the allowed mass range can form a central seed BH, for the parameter choices for the ‘massive seed’ model. The results shown here are largely insensitive to the efficiency of black hole merging and accretion. The merger and accretion efficiency primarily affect the mass of the central black holes, not the presence or absence of one. The present-day BHOF is therefore a sensitive probe of the efficiency of black hole formation in haloes at high redshifts. Observations of satellites at relatively high velocity dispersions might therefore distinguish between the massive seed and Population III models presented here, although this prospect depends on the ability to detect BHs where they exist (see Section 5.4).

Unlike the BHOF, the masses of BHs within galaxies are in general sensitive to the merger efficiency and accretion. However, in the environment we are investigating we expect BH growth to be largely inefficient. In our model, black holes accrete mass when the host halo experiences a major merger and remains baryon rich over the merger timescale. Gas-rich major mergers are rare for the progenitors of our satellite galaxies, so BH growth through mergers and accretion is suppressed.

In a baryon poor halo, BH-BH mergers will not complete, accretion does not occur, and the black hole mass does not change. Even before reionization, when all galaxies are gas-rich, two factors contribute to the limited growth of BHs. On the one hand, the rarity of seeds causes BHs to evolve mostly in isolation. On the other hand, BH growth through accretion at high redshifts is negligible in our model.

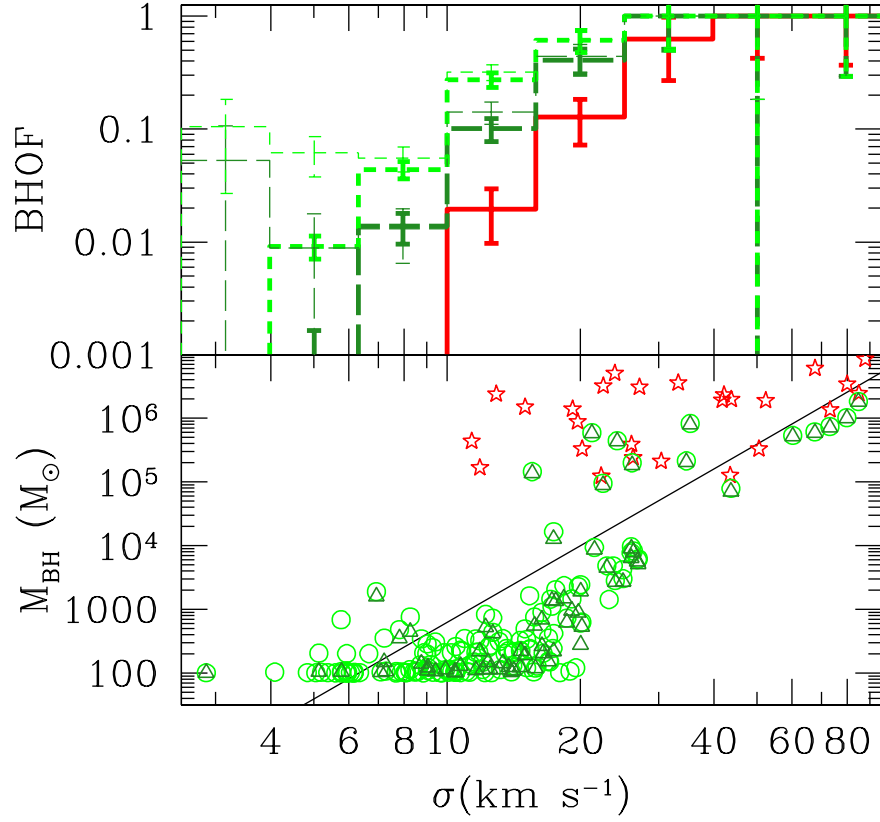


**Figure 5.2.** Top: fraction of galaxies, at a given velocity dispersion, which host a central BH (occupation fraction, BHOF). Long-dashed green histogram: ‘peak3.5’ case. Short-dashed green histogram: ‘peak3’ case. Thick lines: all satellites. Thin lines: luminous satellites. Solid red histogram: ‘massive seeds’ case. Bottom: the  $M_{\text{BH}}$ –velocity dispersion ( $\sigma$ ) relationship for BHs in satellites. We here show the results of a suite of ten realisations. Stars: ‘massive seeds’. Circles: ‘peak3.5’. Triangles: ‘peak3’.

Accreting BHs grow according to the velocity dispersion of the host halo, but the seed masses we consider exceed the BH mass expected for small haloes based on local scaling relations. For satellites with velocity dispersions similar to those of the Milky Way dwarf galaxies, Population III remnant black holes grow to no more than about an order of magnitude larger than the initial seed mass at  $z = 0$ . Massive seed masses remain effectively unchanged. This is an important result, independent of the formation scenario. BHs in dwarf galaxies indeed provide a clear indication of the initial seed properties.

This can be seen in Figure 5.2, where we show the expected relationship between BHs and their ‘dwarf’ hosts. At  $\sigma < 20 - 40 \text{ km s}^{-1}$  there is no correlation between BH masses and velocity dispersion. This is due to the very limited mass growth of BHs hosted in low-mass satellites. These satellites have a very quiescent merger history (very few satellites experience any major merger at all at  $z < 6$ ), causing their central BHs to starve and remain near the original seed mass. This leads to an asymptotic horizontal ‘plume’ (see also Volonteri & Natarajan, 2009). Additionally, a secondary role is played by mass stripping, which depends on both the mass of the host and the satellite, but also on the orbital parameters – stripping being much more effective for radial orbits where satellites plunge deep into the potential well of the host, where densities are higher. A severely stripped system has a much larger BH-to-host ratio. The final BH-to-host relationship is therefore a combination of nature (formation mechanism) and nurture (BH feeding and dynamical evolution of the host).

## 5.4 Observational Prospects

### 5.4.1 Dynamical measurements

The presence of an BH can be tested dynamically if the region where the gravitational potential of the black hole dominates the gravitational potential of the host can be resolved. This region is referred to as the sphere of influence of the black hole. We adopt here the definition of the sphere of influence as the region within which the

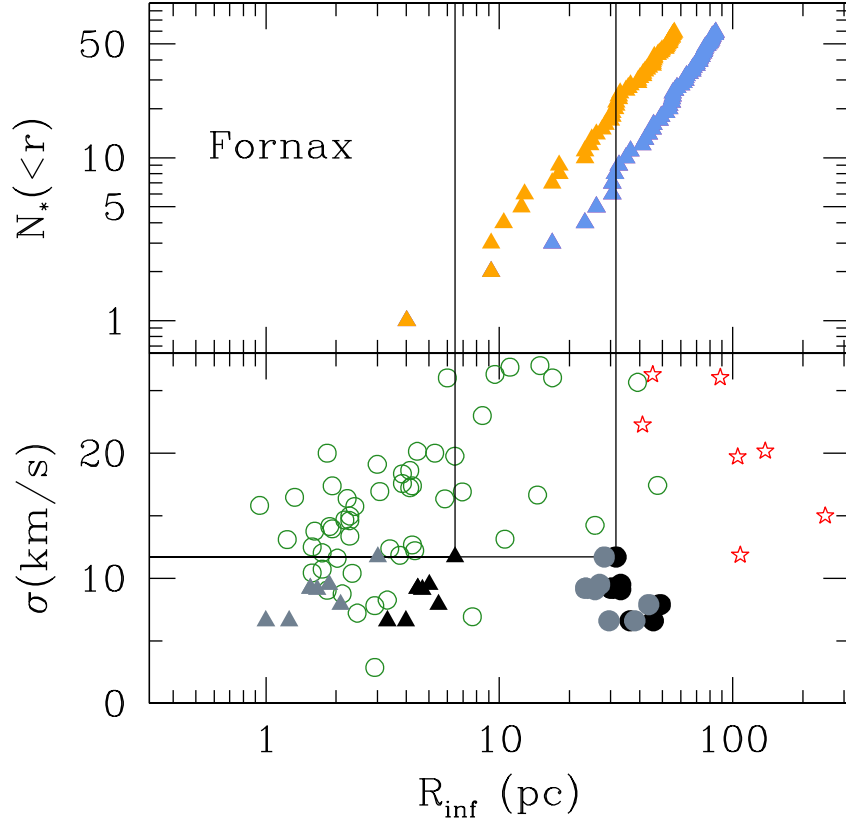


**Figure 5.3.** Top panel: number of stars within a given projected radius in Fornax. Lower curve: all Fornax member stars for which velocities are currently available in the published kinematic samples of Walker et al. (2009a). Upper curve: all Fornax target candidates, including unobserved stars, that are sufficiently bright ( $V < 21.5$ ) for velocity measurements with existing 6m – 10m telescopes. Bottom panel: relationship between velocity dispersion ( $\sigma$ ) and radius of the sphere of influence of BHs – defined as the sphere that encompasses  $2 \times M_{\text{BH}}$  – for ten halo realisations. Stars: ‘massive seeds’. Circles: ‘peak3.5’. Black triangles: Milky Way satellites: we assume that the BH sits on the  $M_{\text{BH}} - \sigma$  relationship, and the density profile is cored. Grey triangles: as above, but for an NFW profile. Black dots: we assume a fixed BH mass,  $10^5 M_{\odot}$  and a cored profile. Grey dots: as above, but for an NFW profile.

enclosed mass in stars and dark matter equals twice the BH mass. The radius of the sphere of influence is therefore defined as:  $M(r < R_{\text{inf}}) = 2 \times M_{\text{BH}}$ .

The lower panel in Figure 5.3 plots stellar velocity dispersion against  $R_{\text{inf}}$ , estimated for massive seed and Pop III cases. Overplotted are values estimated for the eight ‘classical’ dwarf spheroidal satellites of the Milky Way, for which line-of-sight velocities have been measured for up to a few thousand stars per galaxy (Walker et al., 2009a). For these objects we adopt the stellar velocity dispersion measurements of Walker et al. (2009a), and then adopt an BH mass from the mass-velocity dispersion relationship (Tremaine et al., 2002). In order to calculate the sphere of influence for the real dSphs, we consider the best-fitting cored and cusped (NFW) mass profiles with parameters listed in Table 3 of Walker et al. (2009a). If we assume the observed dSphs have NFW dark matter profiles, then according to the M-sigma relation, their BH masses correspond to spheres of influence of  $1 < R_{\text{inf}} < 2$  pc. If the dSph dark matter profiles are cored, then the spheres of influence are a few times larger,  $3 < R_{\text{inf}} < 7$  pc.

In order to evaluate prospects for detecting kinematic signatures from such BHs in real dSphs, the upper panel of Figure 5.3 indicates the number of spectroscopic target stars within a given projected radius in Fornax, the most luminous dSph satellite of the Milky Way. Curves indicate the cumulative surface brightness profiles of 1) all Fornax member stars for which velocities are currently available in the published kinematic samples of Walker et al. 2009a (see also Battaglia et al., 2006), and 2) all Fornax target candidates, including unobserved stars, that are sufficiently bright ( $V < 21.5$ ) for velocity measurements with existing 6m – 10m telescopes. The latter profile represents the largest samples that are possible at present; unfortunately, these would include fewer than 5 stars within the spheres of influence estimated for the classical dSphs. Thus even for the brightest nearby dSphs, the detection of any BH must await the next generation of 20-30m telescopes, which may increase kinematic sample sizes by more than an order of magnitude.

Finally, we consider the spheres of influence due to BH masses of  $\sim 10^5 M_{\odot}$ , a mass of order of the upper limits derived for the ‘massive seed’ scenario (we note



here that the formalism proposed by Lodato & Natarajan (2006) and adopted here gives the *total* mass available for forming an BH seed. Most likely the final seed mass is smaller, see Begelman et al., 2006). For such masses, the expected spheres of influence reach  $< 50$  pc for the observed dsphs. For Fornax, the expected value of  $R_{\text{inf}} \sim 30$  pc encloses 10 stars in the existing velocity sample, and 25 stars in the list of current target candidates. If all these stars are observed, the resulting sample may help diagnose whether Fornax has an BH of mass  $\sim 10^5 M_{\odot}$ .

Figure 5.3 suggests that BHs generated as ‘massive seeds’, having larger masses and a larger  $R_{\text{inf}}$ , would be the most favourable scenario from an observational point of view. However, their typical BHOF is lower, always below 40 percent and decreasing to less than a percent for ‘true’ dwarf galaxy sizes ( $\sigma \sim 5\text{--}15$  km s $^{-1}$ ; Walker et al., 2009a). From Figure 5.2, the typical BHOF for a massive seed BH in a dwarf galaxy like Fornax is  $\sim 2$  percent, meaning that  $\sim 50$  Fornax-like dwarfs would need to be observed to have significant probability of finding an BH. Population III remnants have instead a higher BHOF, but their masses have not grown much since formation, making their detection harder.

#### 5.4.2 Gravitational waves

The detection of gravitational waves from a BH in a dwarf galaxy undergoing a merger with another black hole is another possible probe. The Einstein Telescope, a proposed third-generation ground-based gravitational-wave (GW) detector will be able to detect GWs in a frequency range reaching down to  $\sim 1$  Hz (Freise et al., 2009). Sources with masses of hundreds or a few thousand solar masses will generate GWs in this frequency range, which is out of reach of *LISA* or the current ground-based detectors. Since dwarf galaxies have a very quiet merger history, we would not expect many BH-BH mergers involving dwarf galaxies at the present epoch. However, gravitational waves may also be generated in dwarf galaxies by mergers between the central BH and stellar remnants (stellar mass black holes) in the centre of the dwarf. It is estimated that the Einstein Telescope might detect as many as one thousand of these inspiral events in globular clusters, assuming a relatively high intermediate mass

black hole occupation fraction in the clusters (Gair et al., 2011). The same mechanism would operate in dwarfs, and the predicted rate of mergers from this channel scales with the core stellar density,  $n$ , as  $n^{4/5}$  (Gair et al., 2011). The core stellar densities in nearby dwarf galaxies are typically very low, however, e.g., the estimate for Fornax is  $\sim 10^{-1}\text{pc}^{-3}$  (Mateo, 1998) and for Sagittarius is  $\sim 10^{-3}\text{pc}^{-3}$  (Majewski et al., 2005). These densities are several orders of magnitude lower than the typical core densities in globular clusters, which are  $\sim 10^{5.5}\text{pc}^{-3}$ .

We estimate the number density of BHs in dwarfs via recent theoretical works that study the population of dwarfs as satellites of the Milky Way (Reed et al., 2005; Diemand et al., 2007; Springel et al., 2008). These simulations suggest that the number of satellites per halo has the following form:

$$N(> v_{\text{sat}}) = N_* \left( \frac{v_{\text{sat}}}{v_{\text{host}}} \right)^\alpha, \quad (5.7)$$

where  $v_{\text{sat}}$  and  $v_{\text{host}}$  are the maximum circular velocity of the satellite and the host halo, respectively. Springel et al. (2008) find  $N_* = 0.052$  and  $\alpha = -3.15$ . If we extrapolate the  $M_{\text{BH}} - \sigma$  correlation to  $10^2$ – $10^3 M_\odot$  BHs and assume an isothermal galaxy profile, then  $v_{\text{sat}} \sim 10$ – $20 \text{ km s}^{-1}$ . With this formalism we obtain the number of satellites in the interesting mass range per dark matter halo ( $N_{\text{sat}}$ ), where the mass of the halo is uniquely determined by its maximum circular velocity. The number density of dark matter halos can be easily obtained by integrating the modified Press & Schechter function (Sheth & Tormen, 1999) which provides the mass function of halos,  $dn/dM_h$ . Therefore we estimate a number density of satellites (per comoving cubic Mpc) as:

$$n_{\text{sat}} = \int \frac{dn}{dM_h} N_{\text{sat}}(M_h) dM_h \sim 1 \text{ Mpc}^{-3}, \quad (5.8)$$

adopting the normalization proposed by Springel et al. (2008). We now have to correct for the fact that not all dwarf galaxies are likely to host an BH. Based on the models presented here, a fraction  $\sim 0.01$ – $0.1$  of dwarfs host an BH with mass  $\sim 10^2$ – $10^3 M_\odot$ . Furthermore, we must account for the fact that many of these satellites do not form stars (Bovill & Ricotti, 2009, and references therein). Based on Macciò et al. (2010),

we estimate that a fraction  $f_* \sim 0.8$  of dwarfs with masses  $> 2 \times 10^7 M_\odot$  formed stars and will contain stellar mass BHs that can merge with the central BH. The final estimate for the number density of dwarfs hosting an BH that could be Einstein Telescope sources is  $\sim 0.008\text{--}0.08 \text{ Mpc}^{-3}$ . This number density is approximately an order of magnitude smaller than the  $\sim 0.3 \text{ Mpc}^{-3}$  assumed for globular clusters in Gair et al. (2011). Combining the core stellar density and the number density scalings, we conclude that the rate of GW detections from this channel is likely to be  $\ll 1$  per year. Therefore, although it is not inconceivable that third generation GW detectors will detect events originating in dwarf galaxies, any events will be serendipitous.

## 5.5 Conclusions

We study the black hole population of dwarf galaxies in a Milky Way-sized halo to probe the scaling relations between BH and host in low mass galaxies. We consider two BH formation mechanisms: a ‘massive seeds’ model where seeds form via gas-dynamical collapse and a Population III remnant model. We place BH seeds in the progenitor halos of a Milky Way-type halo and follow their evolution until  $z = 0$ . As smaller halos merge with the main halo, we follow their dynamical evolution under the effects of dynamical friction and tidal stripping. At  $z = 0$  the unmerged dwarfs produce a satellite population consistent with observed and simulated results.

Several factors lead to a low mass BH population in dwarfs that does not evolve with redshift and host velocity dispersion. Dwarf galaxies have a quiet merger history, limiting the growth in their BHs through BH-BH mergers and merger driven accretion. We find that dwarf galaxies are baryon-poor, in agreement with observations, having lost much of their gas to the ultraviolet background after the reionization of the universe beginning at  $z = 9$ . Any mergers that do occur are between gas poor galaxies, which are not expected to lead to efficient BH pairing (and subsequent BH-BH mergers) or drive significant gaseous inflows.

Our results suggest that the BH masses in galaxies with velocity dispersions  $< 50 \text{ km s}^{-1}$  may deviate significantly from the  $M_{\text{BH}}\text{--}\sigma$  relation observed locally (Tremaine et al., 2002; Gültekin et al., 2009). Since the BHs in these galaxies have not grown

much since formation, the BH mass reflects the seed formation mechanism rather than a close evolutionary link with the host galaxy. At higher velocity dispersions  $> 50 \text{ km s}^{-1}$ , we find a transition onto the  $M_{\text{BH}} - \sigma$  relation (Figure 5.2). These larger galaxies have remained gas-rich and experienced major mergers during their evolution, driving strong BH growth that overwrites the original BH seed mass and pushes the BHs onto the scaling relations. If the scaling relations are primarily established during gas-rich major mergers (Robertson et al., 2006), then low mass galaxies with quiet merger histories represent a different evolutionary history and it is not surprising that their BHs would scale differently with the host.

Evidence of increased scatter is also seen in the largest detected BHs (McConnell et al., 2011). McConnell et al. suggest that the increased scatter indicates a different evolutionary process in the largest BHs ( $M_{\text{BH}} \simeq 10^{10} M_{\odot}$ ) than in the better studied BHs that anchor the observed scaling relations ( $M_{\text{BH}} = 10^7 - 10^9 M_{\odot}$ ). Massive red elliptical galaxies may grow predominantly through dry (gas-poor) mergers that grow the mass of the galaxy more than the central velocity dispersion (e.g. Ciotti et al., 2007). If the most massive BHs hosted in these galaxies grow through BH-BH mergers rather than via accretion, as in lower mass galaxies, then dry mergers may produce BHs that lie above the  $M_{\text{BH}} - \sigma$  relation (Boylan-Kolchin et al., 2006).

Just as McConnell et al. (2011) suggest a different evolutionary process in the most massive galaxies, we suggest a different process in the least massive galaxies. Their quiet merger histories lead to little BH growth and BHs that lie off of the  $M_{\text{BH}} - \sigma$  relation. Our results support the findings of Greene et al. (2010), who suggest that there is no universal  $M_{\text{BH}} - \sigma$  relation. Rather, the scaling relations may depend on the morphology, mass, and history of the galaxy in question.

Finally, we consider the prospect of determining the BH seed formation mechanism at high redshift by measuring the mass or occupation fraction of BHs in dwarf galaxies. Since the BHs have not grown significantly since their formation, a direct mass measurement would distinguish among the models considered here, ‘massive seeds’ and Population III stellar remnants. The ‘massive seeds’ model produces rare but large seeds ( $M \simeq 10^5 M_{\odot}$ ) that should be detectable in a large classical dwarf

galaxy like Fornax (with  $\sigma \simeq 11 \text{ km s}^{-1}$ ), but occupy only a few percent of typical dwarf galaxies, inhibiting their detection. The BHs resulting from the Population III remnant models are much more abundant at low redshift, but the low mass BHs ( $M_{\text{BH}} \simeq 10^2 - 10^3 M_{\odot}$ ) cannot currently be detected. In larger galaxies, accretion has overwritten any signature of the seed formation mechanism.

## CHAPTER 6

# Conclusions

In this work, we study the coevolution of supermassive BHs and their host galaxies, motivated by recent work that has established scaling relations that link galaxy properties on kpc scales to BHs on sub-pc scales. We focus on the processes by which both BHs and galaxies grow in the  $\Lambda$ CDM cosmology. Mergers between galaxies drive strong gaseous inflows that feed both star formation, growing the galaxy, and accretion, growing the central BH. We consider scenarios ranging from high redshift mergers between gas-rich galaxies to the dynamical evolution of gas-poor dwarf galaxies in the Milky Way today, focusing always on the small scale dynamics of BHs to understand how they affect and are affected by their environment. Here we briefly summarize our work, then discuss future directions of study.

### 6.1 Summary

We first focus on the dynamics of high redshift unequal mass galaxy mergers, which are expected to be the most common in the  $\Lambda$ CDM cosmology. To study these mergers, we use high resolution ( $<20$  pc) N-body SPH simulations, including radiative gas cooling, star formation, BH accretion, and feedback from supernovae and BHs. In Chapter 2, we describe the code GASOLINE that is used to perform our simulations as well as their numerical setup. We then focus on the dynamics of the mergers and how they drive growth in their BHs through accretion and BH-BH mergers.

In Chapter 3, we describe the dynamical evolution of the galaxies, focusing on the roles of ram pressure stripping, gaseous inflows, and tidal shocks in driving central star formation in both galaxies. In unequal mass mergers, we find that the smaller

galaxy experiences stronger inflows that build up a dense central cusp. In some cases, the resulting cusp is denser than the primary galaxy’s nucleus and the primary’s nucleus is disrupted by tidal shocks. We estimate the timescale from disruption to the formation of a BH binary, an important step on the way toward a BH-BH merger. We find that strong star formation in the secondary galaxy’s nucleus, triggered by the dynamics of the merger, tends to lead to a shorter timescale for binary formation.

In Chapter 4, we instead follow BH accretion driven by the large scale gaseous inflows produced during the galaxy interaction. Merger triggered accretion is generally confined to the late stages of the merger, following the second pericenter passage, but the resulting BH growth is up to an order of magnitude higher than all previous accretion. We find that low mass ratio mergers ( $\leq 1:6$ ) lead to inefficient growth in the primary BH as the primary galaxy’s disk is no longer strongly perturbed during the merger. We discuss when and where both BHs accrete simultaneously, producing dual active galactic nuclei (AGN), an active area of study that provides a clear indicator of merger driven accretion. We find good agreement with existing observations of dual AGN and discuss the galaxy mergers that lead to the longest dual AGN timescale.

We then zoom further out, sacrificing the high resolution of our merger simulations to follow the complete cosmological evolution of a galaxy using Monte Carlo merger trees. In Chapter 5, we consider the history of BHs in the smallest known galaxies. We consider the formation of seed BHs in the high redshift progenitor haloes of a Milky Way sized galaxy. At low redshifts, we follow the dynamical evolution of small haloes in the main halo of the Milky Way, forming an analog of the local dwarf galaxy population. Our results show that these small haloes are gas poor and have evolved quietly since high redshift, leading to little growth in their BHs. We suggest the existence of a population of small BHs in dwarf galaxies that have evolved differently from the supermassive BHs that large galaxies host. Their pristine state would allow the determination of the high redshift seed formation mechanism if their existence could be observationally established, but we provide arguments for why they are, unfortunately, difficult to detect and must await future observations.

## 6.2 Improvements in Sub-Grid Models

We now discuss recent developments in sub-grid models, which drive unresolved physics in simulation codes. We argue that high resolution simulations, such as those that are presented here, are pushing the limits of current sub-grid models. As resolution improves further, it will be important to model physics accurately on smaller and smaller scales, requiring more sophisticated models and a better understanding of the underlying physical processes.

Our simulations resolve extremely dense gas, allowing us to limit star formation to gas with a density near the average density of molecular clouds,  $n > 100 \text{ amu cm}^{-3}$ . While we resolve the average densities of molecular clouds, we cannot resolve the star forming cores at even higher densities, nor can we tie star formation directly to dense molecular gas and include molecular cooling. As simulation resolutions continue to improve with the availability of computational resources, more sophisticated models of star formation and supernova feedback are required to produce realistic results.

Christensen et al. (2012) present a model for molecular hydrogen in GASOLINE which tracks the non-equilibrium molecular hydrogen abundance in galaxies. The transition from atomic to molecular gas occurs at densities of  $n = 10 - 100 \text{ amu cm}^{-3}$ , requiring a gas particle mass  $< 10^4 M_{\odot}$  in order to resolve the correct densities and produce consistent results. Molecular cooling provides more consistent cooling at low temperatures than metal cooling alone, as is used in our simulations. With the inclusion of the molecular gas model, they modified the star formation implementation from Stinson et al. (2006) (the model used in the simulations presented here) by tying star formation directly to molecular gas. They effectively removed the density requirement for star formation, instead tying the star formation efficiency to the molecular gas fraction. Additionally, they were able to lower the maximum gas temperature for star formation to 1000 K (for reference, we use 6000 K). While this model does not reflect a better understanding of the underlying physics of star formation, it does represent an improvement in modeling star formation and cooling that allows simulations to better mimic the behavior and properties of molecular



clouds. It is an important step towards improving sub-grid models in high resolution simulations.

Another area that requires further improvement is the physics of BH accretion and feedback. While large scale simulations cannot hope to resolve the formation of an accretion disk on sub-pc scales, a Bondi-Hoyle-Lyttleton accretion recipe may not produce the ‘correct’ accretion rates based on resolved gas properties. Hopkins & Quataert (2010) perform multi-scale simulations of gaseous inflows in isolated galaxies, ultimately resolving scales of  $< 0.1$  pc in small scale simulations including only the central regions of the galaxy. We note that Hopkins & Quataert use an effective equation of state in modelling their interstellar medium, averaging over the dynamics of supernovae, stellar winds, and HII regions, which differs from the implementation in GASOLINE. While the specifics of their code differ from ours, their results are instructive. On sub-pc scales, they find that the accretion rate onto the BH is highly variable on  $< 10^5$  yr timescales, whereas the gas properties on larger scales, such as those used in a typical Bondi-Hoyle-Lyttleton accretion rate estimate, vary more slowly. Indeed, we find that accretion rates in our simulations generally vary on timescales of a few  $10^5$  yr due to BH feedback or gas motions, an order of magnitude longer than the shortest variability timescales found by Hopkins & Quataert (2010).

Debuhr et al. (2010) develop an accretion model based on viscous disk accretion, mimicking the physics of an  $\alpha$  disk (Shakura & Sunyaev, 1973), albeit on much larger scales (based on gas properties within 188 pc of the BH). Their goal is to account for the angular momentum of gas near the BH, which may prevent it from reaching the BH as is assumed with the Bondi prescription. They suggest that Bondi accretion overestimates the accretion rate in their simulations, although we note that they do not resolve the Bondi radius nor the sub-pc scales where viscous disk accretion would operate. Power et al. (2011) use an alternate method to account for the angular momentum of the gas, developing an ‘accretion disk particle’. Gas that approaches the BH is removed and its mass is added to the accretion disk particle accompanying the BH. The BH then accretes from this particle on the viscous timescale,  $t_{\text{visc}}$ , which they set to 10 – 100 Myr in galaxy formation simulations. These alternative accretion

prescriptions are a work in progress and need further testing and comparison with the Bondi prescription.

We use a thermal feedback prescription for BH feedback, imparting energy into gas particles near the BH and preventing them from cooling to ensure a hydrodynamical response (see Appendix A for more details). Other feedback models have been implemented that attempt to reproduce the effects of AGN driven winds driving large scale outflows (King & Pounds, 2003; Debuhr et al., 2012). These models mimic the physics of radiation pressure on small scales, although they avoid expensive radiative transport calculations. Dubois et al. (2012) include in their cosmological simulations the effects of radio mode feedback at low accretion rates in addition to the standard quasar feedback recipes (Di Matteo et al., 2005). Their radio mode feedback acts on a cylinder near the BH, mimicing the formation of a bipolar jet and departing from the standard isotropic feedback formulations.

The underlying physics of star formation, BH accretion, and BH feedback are unfortunately not well understood and are active areas of study. As computational resources become more abundant and efficient and the resolution in simulations continues to improve, however, it is vital to include the latest results in these fields into simulations of galaxy formation to ensure that the small scale physics is as accurate as possible. With crude models, the predictive power of simulations is limited and it is difficult to take full advantage of high resolution.

### 6.3 Future Work

The simulations presented here include many mass ratios and several orbital inclinations for the merging galaxies. We have focused on the mergers most relevant to galaxy formation in a cosmological context. One parameter that we plan to explore further is the impact of the gas fraction in the galaxies. Kazantzidis et al. (2005) and Callegari et al. (2009) as well as our work here have established the importance of having a gas fraction  $f_g \simeq 0.1 - 0.3$  for efficient pairing in unequal mass mergers. Observations of high redshift actively star forming galaxies indicate instead higher gas fractions, with a cold gas fraction of 44 percent at  $z \simeq 2.3$  (Tacconi et al., 2010).

Bournaud et al. (2011) argue that the interstellar medium in high redshift galaxies is turbulent and clumpy. They simulated mergers between galaxies with disk gas fractions of 70 percent and find evidence of violent dissipative collapse of the gas in the disks. We plan to consider higher gas fractions as well to study the impact on our results (Chapters 3 and 4). A higher gas fraction may produce higher star formation rates in our galaxies in better agreement with observations of high redshift galaxies, which find star formation rates of  $>10 M_{\odot} \text{ yr}^{-1}$  in normal star forming galaxies (e.g. Erb et al., 2006). One difficulty in simulating such high star formation rates is that the initial gas in the galaxies is quickly depleted. Without a mechanism to replenish the gas content, such as cosmological cold gas flows, mergers can only be simulated for a short timescale, motivating faster, more direct mergers or a smaller initial separation between the galaxies.

We also plan to use the merger remnants resulting from our galaxy mergers to provide initial conditions for smaller scale ( $<100$  pc) simulations of BH binary evolution. Past studies have used idealized initial conditions of circumnuclear disks embedded in a stellar spheroid (Dotti et al., 2009, 2010). Dotti et al. resolved scales of  $\simeq 0.1$  pc but evolved the gas in the circumnuclear disk with a purely adiabatic equation of state (with  $\gamma = 7/5$  to represent a cold, star forming disk and  $\gamma = 5/3$  to represent a disk heated by feedback) rather than explicitly following the impact of star formation and feedback. Recent simulations by Maio et al. (2012) have modeled disks with explicit star formation, cooling, and feedback and additionally followed the spin evolution of the BHs, but still focused on an idealized gas-rich circumnuclear disk expected to result from an equal mass galaxy merger. We plan to continue these studies using better motivated initial conditions resulting from our large scale galaxy merger simulations. This fits into our overall goal of following the coevolution of BH and host on all scales, from gaseous inflows driven by the interacting galaxies on kpc scales down to the evolution of a BH binary on  $<10$  pc scales.

## APPENDIX

## APPENDIX A

# GASOLINE: Details of the N-body SPH Code

### A.1 Introduction

GASOLINE is an extension of the N-body tree code Pkdgrav, using smoothed particle hydrodynamics to implement fluid dynamics in an astrophysical context. Numerical problems in astronomy cover a vast range of length and time scales, necessitating adaptable and scalable codes. N-body codes model complex systems by breaking them up into smaller bodies, just as a galaxy is made up of individual stars. As the masses of individual bodies decrease, the resolution of the simulation improves and the results come closer to the reality of galaxies, which contain billions of stars. Simulations are limited by computational resources, however.

We summarize here the major features of GASOLINE. Additional information can be found in Stadel (2001), Wadsley et al. (2004), and Stinson et al. (2006). Monaghan (1992) provides an excellent review of smoothed particle hydrodynamics.

### A.2 Gravity

The principal force in most astronomical systems from planets to star systems to galaxies is gravity. In dynamic systems where self-gravity is important, analytic methods fail and N-body simulations are needed.

The most straight-forward method for calculating gravitational forces is direct summation, where the force on each particle is determined using the mass and position of every other particle. This method scales as  $O(N^2)$  and is impractical for large numbers of particles ( $N \simeq 10^5$ ). Since the gravitational force falls off quickly with distance, however, the exact distribution of a collection of particles is unimportant

in calculation the gravitational force on a distant particle. Tree-based algorithms for calculating gravity, such as the one GASOLINE uses, use this fact to calculate gravitational forces more efficiently, scaling instead as  $O(N \log N)$ . This improvement in scaling enables the use of simulations with orders of magnitude more particles.

Tree-based methods recursively divide particles into separate spatial domains based on their positions. In calculating the gravitational force on a given particle, large sections of the tree are bypassed and a multipole expansion of the mass distribution is substituted. For nearby particles, direct summation is used, but for remote particles, an approximation to the mass distribution is used. When walking the tree to calculate forces, an opening criterion is used to determine if the multipole expansion of the given node is acceptable. The angle that the node subtends relative to the particle in question is compared to a minimum opening angle,  $\theta_c$ . If a node is opened, the criterion is again checked on its sub-nodes in the tree structure. Otherwise, the multipole expansion for the particles contained in that node is used instead, saving the need to venture any further into the tree. The accuracy of the tree gravity calculation can easily be tuned using the minimum opening angle,  $\theta_c$ . GASOLINE uses a fourth-order hexadecapole multipole expansion.

Use of a spatial binary tree has several advantages aside from the improvement in scaling over direct summation methods. When hierarchical timesteps are used, gravitational forces can easily be calculated for the subset of particles that are active at the current timestep. This is especially helpful for simulations with a high dynamic range, where a small number of particles may have small dynamical timescales and require frequent force calculations. The tree can also be used to efficiently find the neighbors of a given particle, an important process in smoothed particle hydrodynamics.

GASOLINE uses a balanced binary K-D tree internally. Rather than dividing each node on the position of the median particle as in a traditional K-D tree, each node is instead bisected along its longest axis. This prevents the tree from containing nodes with large axis ratios which contribute to errors in the gravity calculations. Recursive splitting of each node during tree construction stops when a node contains  $n_{\text{bucket}}$  or fewer particles. This reduces the size of the tree in memory and contributes

negligibly to run-time for small  $n_{\text{bucket}}$ . Once the tree has been constructed, the center of mass and moments of the mass distribution are calculated for each node in a single pass through the tree.

When simulating collisionless bodies, it is necessary to impose a softening length in gravitational force calculations to prevent spurious interactions on scales that are not well resolved. This smooths out the force of gravity on small scales comparable to the softening length. Without a softening length, particles that move close to each other require very small timesteps to avoid gravity errors. The softening length is a measure of the resolving power of a simulation and is directly tied to the masses of individual particles and therefore the total number of particles in the simulation. Forces return to the exact Newtonian result at a distance of double the softening length.

### A.3 Smoothed Particle Hydrodynamics

GASOLINE implements gas dynamics using smoothed particle hydrodynamics, a Lagrangian method that follows individual fluid elements (particles). Lagrangian methods naturally adapt to situations with highly variable densities. Particles congregate in regions of high density and the resolution in the gas phase improves. Gaseous quantities at a given position are defined as a weighted sum of the properties of the surrounding gas particles. The weights are defined by the smoothing kernel, which gives non-zero weights to all gas particles within a smoothing length of the position. The smoothing length is a measure of the resolution of the hydrodynamic properties. Its value at a given position is the distance to the  $k$ th nearest gas particle, so the properties of a given gas particle are based on its  $k$  nearest neighbors. A separate tree from the gravitational tree allows a particle's nearest neighbors to be efficiently found. In the simulations presented here,  $k$  is set to 32.

GASOLINE includes radiative cooling with a cooling function that includes atomic hydrogen, helium, and metal lines. The cooling function ranges from 10 to  $10^9$  K. In the majority of the simulations presented here, each gas particle can cool to this lower limit of 10 K. Chapter 4 includes a run with a higher temperature floor of 500

K, which was designed to test the impact of the temperature floor on star formation.

Gas particles in GASOLINE are eligible for star formation if they satisfy several criteria. They must be below a temperature threshold,  $T_{max}$ , and above a density threshold,  $n_{min}$ . This confines star formation to cold, dense gas, as is observed. Additionally, the gas particle must be part of a locally converging flow satisfying  $\nabla \cdot v < 0$ . The star formation rate scales as:

$$\frac{d\rho_*}{dt} = \frac{c^* \rho_{gas}}{t_{dyn}}, \quad (\text{A.1})$$

where  $t_{dyn}$  is given by  $(4\pi G \rho_g)^{-1/2}$ . The overall dependence on density is  $\rho_{gas}^{3/2}$ . The parameter  $c^*$  can be tuned to match observations of star formation. Star formation proceeds in a stochastic manner among eligible particles, with higher density particles preferred. Each star particle is born with a set mass,  $m_{*,new}$ , which is subtracted from its parent gas particle. When a gas particle reaches a minimum mass,  $m_{gas,min}$ , it is removed and its mass distributed among nearby gas particles. We set  $m_{*,new}$  to half the mass of our initial gas particles.  $m_{gas,min}$  is set to 20 percent of the initial mass.

The star formation rate is tuned to match the observed Kennicutt-Schmidt star formation law (Kennicutt, 1998). Figure A.1 shows results from the 1:2 prograde coplanar merger. Each point represents the star formation surface density in the previous 100 Myr and gas surface density in a radial 500 pc bin. The red points show quiescent star formation and are well fit by the Kennicutt-Schmidt star formation law. We see the star formation surface density turn down at low gas surface densities, in agreement with the simulations of Stinson et al. (2006) and observations by Martin & Kennicutt (2001). The turn down occurs because of the density requirement for star formation, restricting most star formation to the dense regions of the galaxies. The green and blue points show strong star formation late in the merger. We see an enhancement in the star formation during starbursts above the normal law, representing more efficient conversion of gas into stars. We note that similar enhancements have been seen in observations of starbursting galaxies (Daddi et al., 2010; Genzel et al., 2010). An isolated galaxy was evolved with several different values of  $c^*$  to find the



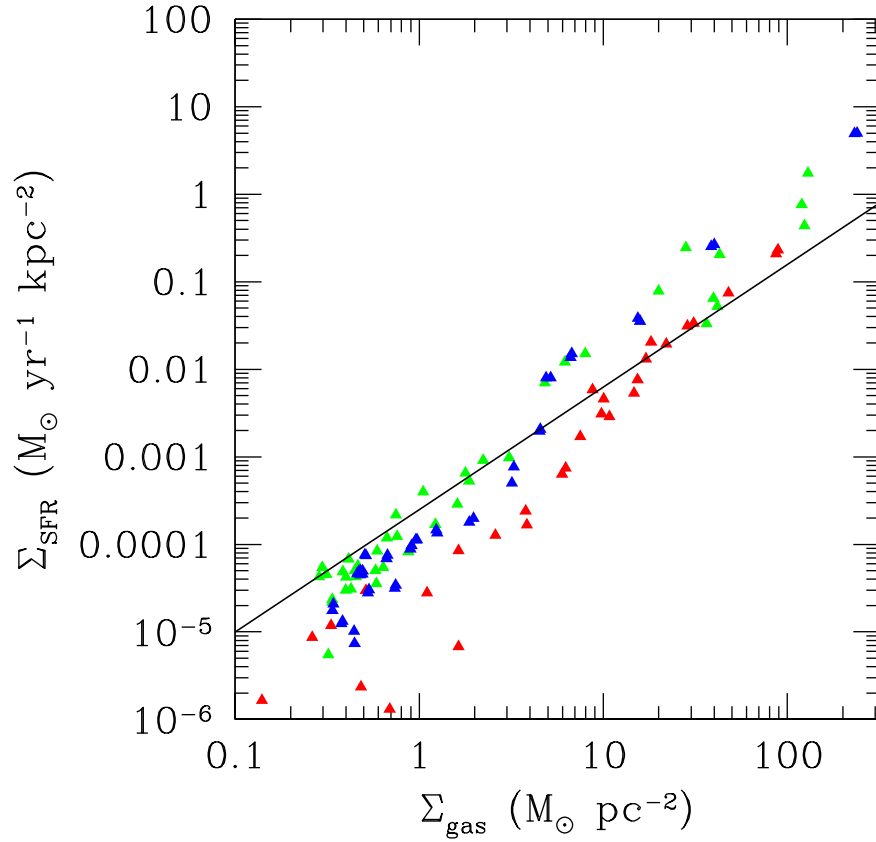


**Figure A.1.** Star formation surface density plotted against the gas surface density for the 1:2 prograde coplanar merger. Each point represents a cylindrical radial bin, 500 pc in width, from the two merging galaxies. The star formation surface density represents stars that formed in the last 100 Myr. The red points correspond to first apocenter and represent quiescent star formation. The green points trace star formation during the starburst at third pericenter. The blue points correspond to the strongest burst of star formation when the galaxies complete the merger. The solid line shows the star formation law from Kennicutt (1998).

best fit to the Kennicutt-Schmidt law. The best fit corresponds to  $c^*$  of 0.015.

GASOLINE includes supernova feedback from recently formed stars. At each timestep, the age and mass of a star particle, together with the initial mass function, are used to determine if a type II supernova has occurred. For each supernova,  $10^{51}$  ergs of thermal energy is injected into nearby gas particles, weighted by the SPH kernel and gas particle mass. In a dense environment, however, this energy will be quickly radiated away through the gas cooling function and have little impact on nearby star formation. Instead, supernovae disable the radiative cooling of nearby gas particles. This feedback model mimics the blastwave solution of McKee & Ostriker (1977). Based on this solution, cooling is disabled for the duration of the Sedov and snowplow phases, typically  $10^6 - 10^7$  years.

Also included is feedback from type Ia supernovae. Since type Ia supernovae originate in older stellar populations, they should not be clustered and should not lead to the blastwave behaviour of type II supernovae. Accordingly, type Ia supernovae do not turn off cooling in nearby gas particles, but distribute mass, energy, and metals. Lastly, Gasoline includes a model of stellar wind feedback to account for the large amount of material that intermediate mass stars return to the ISM. These winds act similarly to type Ia supernovae, but do not inject any energy into surrounding gas particles.

The parameters of the star formation model depend on the resolution of the simulation. In the high resolution simulations presented here,  $T_{\max}$  and  $n_{\min}$  are set to 6000 K and  $100 \text{ amu cm}^{-3}$ , respectively. These properties deviate from typical properties of star forming cores in giant molecular clouds, which have temperatures  $< 100$  K and densities  $> 10^4 \text{ amu cm}^{-3}$ . However, galaxy scale simulations are not able to reliably resolve such densities and molecular cooling is required to follow the evolution of such cold gas. The remaining parameters of the star formation model are the supernova feedback energy,  $10^{51}$  erg, and the star formation efficiency,  $c^*$ , which is set to 0.015.

## A.4 Timesteps

Given the large range of densities encountered in astronomical situations, dynamical timescales vary widely. GASOLINE uses adaptive timesteps such that forces can be calculated for a subset of particles. This prevents all particles from being updated on the timescale of the densest particles, saving significant computational time. With the explicit cooling scheme mentioned before, gas particles at the bottom of the cooling range tend to set the lowest timescale.

During each timestep, particle properties are updated using a Kick-Drift-Kick scheme (Quinn et al. 2007). During each kick, particle velocities and energies are updated for half a timestep. During the drift step, particle positions are updated for a whole timestep. After the drift step, forces are recalculated for active particles. The Kick-Drift-Kick integration scheme requires one force calculation per timestep and is symplectic, which is important for simulating a system over many dynamical timescales. Individual particles are placed on ‘rungs’ depending on their individual timescales, with consecutive rungs differing by a factor of two. Individual timesteps are determined based on particle accelerations and the Courant condition.

## A.5 Black Hole Physics

Black holes in Gasoline are implemented as sink particles that accrete from nearby gas particles. The accretion rate is determined using the Bondi-Hoyle-Lyttleton formula based on local gas particle properties (Bondi, 1952):

$$\dot{M}_{\text{BH}} = \frac{4\pi G^2 M_{\text{BH}}^2 \rho_{\text{g}}}{(c_{\text{s}}^2 + v^2)^{3/2}}. \quad (\text{A.2})$$

Here  $M_{\text{BH}}$  is the mass of the BH,  $\rho_{\text{g}}$  is the local gas density,  $c_{\text{s}}$  is the local sound speed, and  $v$  is the velocity of the BH relative to the surrounding gaseous medium. To account for the inhomogeneous mix of hot and cold gas around the black hole, the total accretion rate is the sum of the accretion rates due to the individual gas particles in the black hole’s kernel (the nearest  $k$  particles), rather than an accretion rate determined using an average gas density and temperature. The accretion rate is

limited by the Eddington rate, assuming spherical accretion from Hydrogen gas:

$$\dot{M}_{\text{Edd}} = \frac{L_{\text{Edd}}}{\epsilon_r c^2} = \frac{4\pi G M_{\text{BH}} m_p}{\sigma_T \epsilon_r c}. \quad (\text{A.3})$$

$\epsilon_r$  is the radiative efficiency, set to 10 percent.  $m_p$  is the proton mass and  $\sigma_T$  is the Thomson cross section for an electron.

Once the accretion rate has been determined, the accreted mass in the given timestep is removed from a nearby eligible gas particle within the BH’s kernel. The particles that contributed the most to the accretion rate are favored. To be eligible, a gas particle must be active during the current timestep. This criterion aids in momentum conservation during integration. Additionally, the gas particle must contain the black hole within its smoothing radius. This criterion is intended to prevent accretion from gas that is significantly separated from the black hole, such as in situations where the environment immediately surrounding the black hole is devoid of gas. During each timestep, a fraction  $\epsilon_f$  of the accreted energy  $\epsilon_r \dot{M}_{\text{BH}} c^2$  is added as thermal energy to the nearest gas particle. A blastwave model was considered, similar to the feedback of type II supernovae, but the blastwave radius generally contains only one gas particle, even at the high resolution of our simulations. Any particles that are affected by black hole feedback have their cooling disabled for their next timestep. This prevents the energy from being quickly radiated away, allowing the gas particle to hydrodynamically respond to the energy injection.

Unfortunately, the details of black hole feedback are not well known, so there is little guidance for the feedback parameter,  $\epsilon_f$ . We assume that the black holes in both the pre-merger galaxies and the final, merged galaxy should lie on the observed scaling relations. We performed several low resolution 1:2 merger simulations, varying  $\epsilon_f$ . After the galaxies merged, we measured the velocity dispersion of the resulting galaxy in a manner similar to observational estimates. The resulting velocity dispersion provides an estimate for how much the black holes should grow during the merger so that the resulting merged black hole lies on the observed scaling relations.  $\epsilon_f = 0.001$  provided the best fit and was used in the high resolution runs presented here.

GASOLINE allows for black hole mergers, but this feature was disabled for the simulations presented here. Our goal is to follow black hole dynamics toward the formation of a binary, near the resolution limit of the simulation. We therefore do not assume that the black holes merge efficiently at our resolution limit.

## APPENDIX B

# Supplementary Material: Dual AGN Observability Timescales

### B.1 Remaining Results from Chapter 4

This appendix contains additional material from Chapter 4. We include the dual AGN observability timescales figures for the remaining simulations (Figures B.1 - B.7). Tables B.1 and B.2 show the dual AGN fraction for the remaining simulations not displayed in Chapter 4.

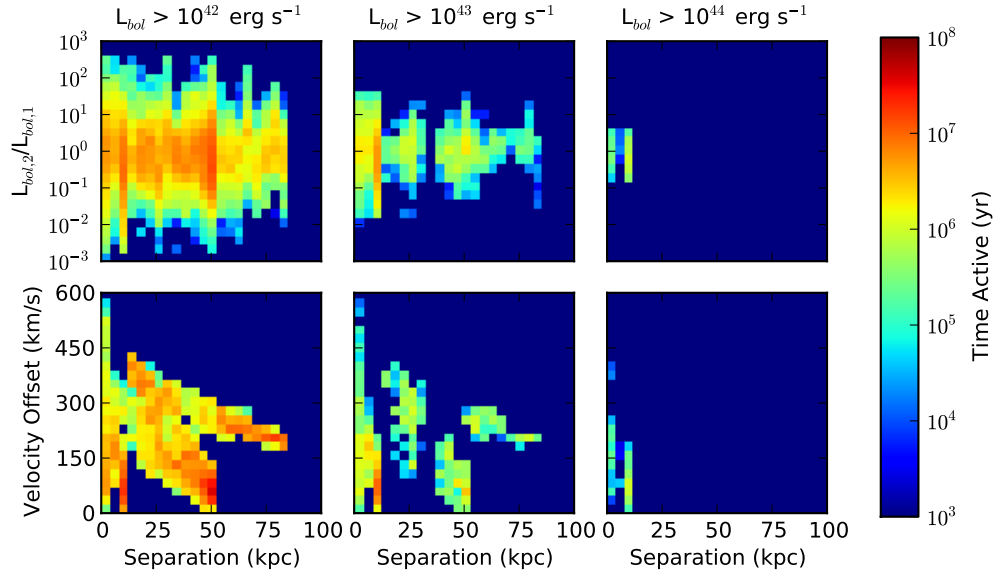


**Figure B.1.** Dual AGN observability timescales in the 1:2 inclined merger. Top panels: luminosity ratio between the two BHs as a function of BH separation when both BHs are accreting at the given luminosity. Bottom panels: velocity offset between the BHs as a function of separation when they are observable as a dual AGN. The color of each point indicates the total dual AGN timescale.

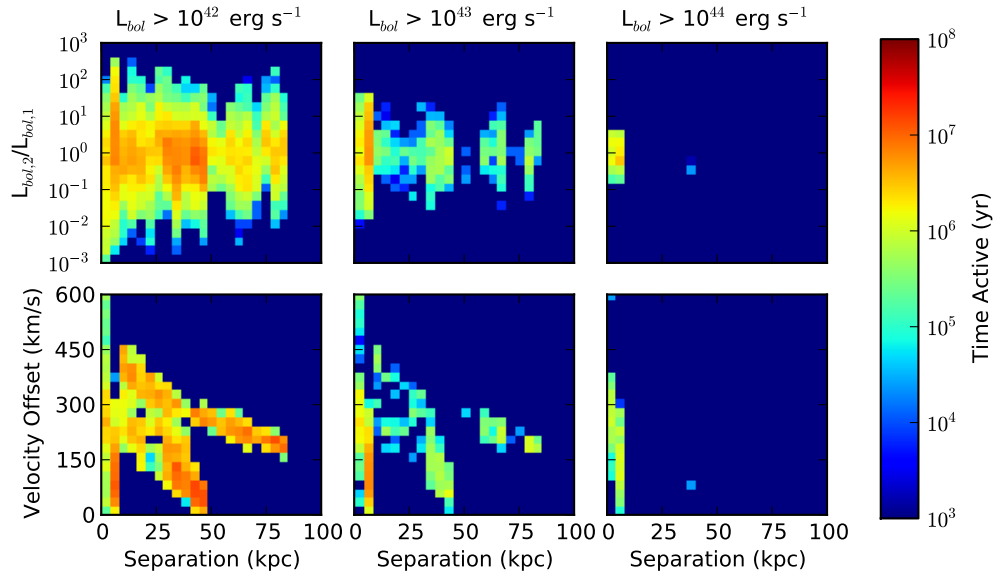


**Figure B.2.** Dual AGN observability timescales in the 1:2 retrograde (secondary) merger. Top panels: luminosity ratio between the two BHs as a function of BH separation when both BHs are accreting at the given luminosity. Bottom panels: velocity offset between the BHs as a function of separation when they are observable as a dual AGN. The color of each point indicates the total dual AGN timescale.

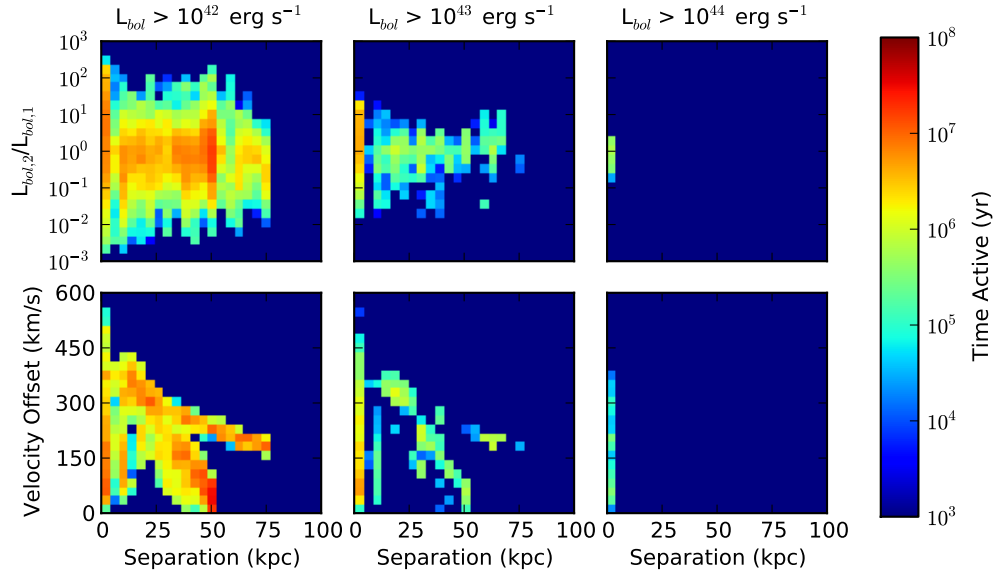


**Figure B.3.** Dual AGN observability timescales in the 1:4 prograde coplanar merger. Top panels: luminosity ratio between the two BHs as a function of BH separation when both BHs are accreting at the given luminosity. Bottom panels: velocity offset between the BHs as a function of separation when they are observable as a dual AGN. The color of each point indicates the total dual AGN timescale.

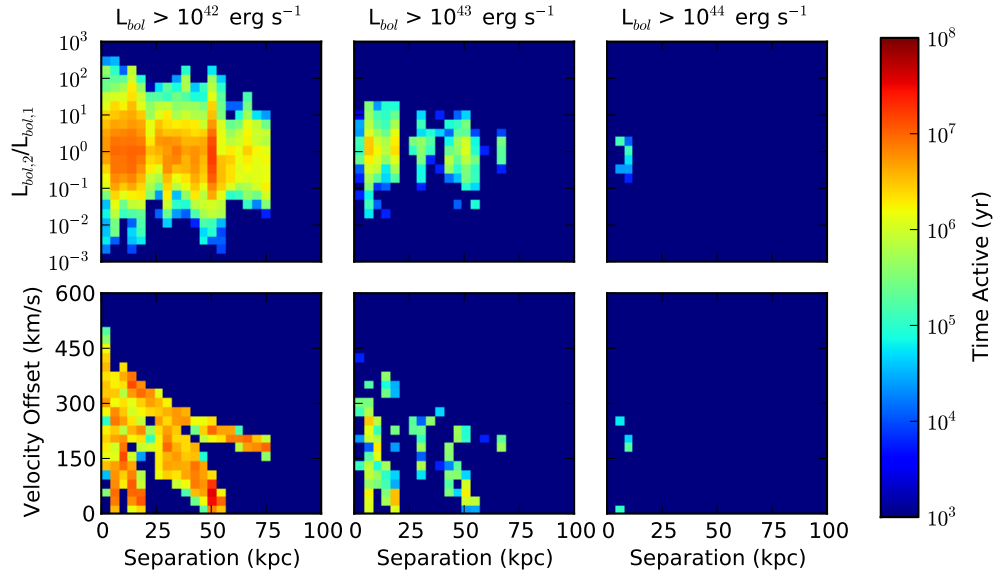


**Figure B.4.** Dual AGN observability timescales in the 1:4 inclined merger. Top panels: luminosity ratio between the two BHs as a function of BH separation when both BHs are accreting at the given luminosity. Bottom panels: velocity offset between the BHs as a function of separation when they are observable as a dual AGN. The color of each point indicates the total dual AGN timescale.



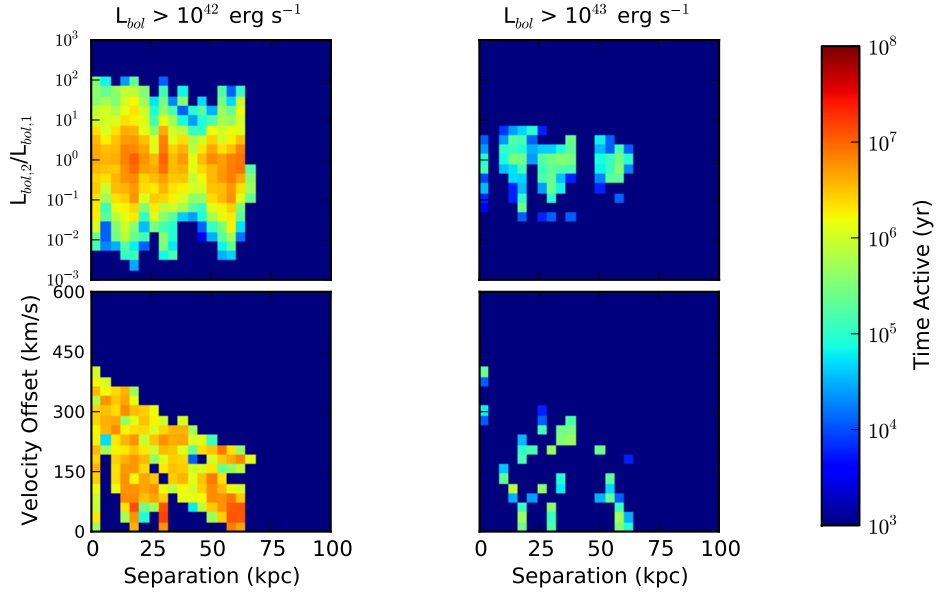


**Figure B.5.** Dual AGN observability timescales in the 1:10 prograde coplanar merger. Top panels: luminosity ratio between the two BHs as a function of BH separation when both BHs are accreting at the given luminosity. Bottom panels: velocity offset between the BHs as a function of separation when they are observable as a dual AGN. The color of each point indicates the total dual AGN timescale.

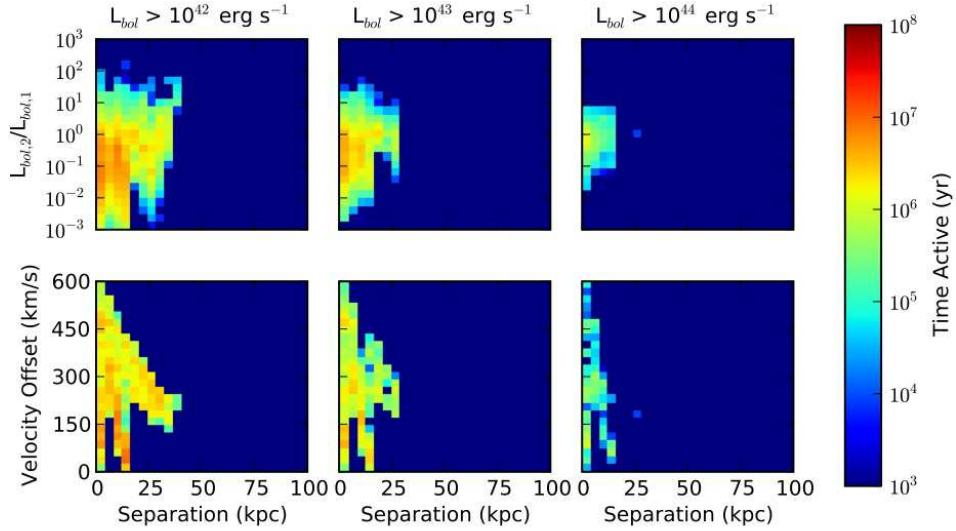


**Figure B.6.** Dual AGN observability timescales in the 1:2 elliptical-spiral merger (no gas). Top panels: luminosity ratio between the two BHs as a function of BH separation when both BHs are accreting at the given luminosity. Bottom panels: velocity offset between the BHs as a function of separation when they are observable as a dual AGN. The color of each point indicates the total dual AGN timescale.

| Simulation             | Threshold          | BH <sub>1</sub> | BH <sub>2</sub> | Dual Fraction | $d > 1$ kpc | $d > 10$ kpc | $\Delta v > 150$ km s <sup>-1</sup> |
|------------------------|--------------------|-----------------|-----------------|---------------|-------------|--------------|-------------------------------------|
| 1:2 Inclined           | $L_{bol} > L_{42}$ | 84.3            | 67.8            | 58.7          | 55.9        | 48.2         | 19.3                                |
|                        | $L_{bol} > L_{43}$ | 31.8            | 19.4            | 16.3          | 14.7        | 10.2         | 6.1                                 |
|                        | $L_{bol} > L_{44}$ | 3.9             | 2.4             | 6.0           | 4.6         | 1.7          | 1.2                                 |
|                        | $f_{Edd} > 0.005$  | 70.2            | 65.6            | 49.6          | 48.0        | 41.2         | 27.1                                |
|                        | $f_{Edd} > 0.05$   | 16.4            | 17.5            | 12.3          | 11.0        | 0.62         | 3.8                                 |
|                        | $f_{Edd} > 0.5$    | 1.9             | 1.9             | 3.3           | 2.6         | 1.0          | 0.78                                |
| 1:2 Retrograde (Sec.)  | $L_{bol} > L_{42}$ | 77.7            | 64.7            | 53.7          | 52.6        | 44.5         | 34.3                                |
|                        | $L_{bol} > L_{43}$ | 27.2            | 16.6            | 26.1          | 25.5        | 6.9          | 13.7                                |
|                        | $L_{bol} > L_{44}$ | 6.0             | 4.1             | 13.2          | 12.7        | 0.02         | 9.0                                 |
|                        | $f_{Edd} > 0.005$  | 62.4            | 62.8            | 44.6          | 43.9        | 36.0         | 29.0                                |
|                        | $f_{Edd} > 0.05$   | 17.0            | 15.9            | 15.8          | 15.5        | 3.2          | 8.9                                 |
|                        | $f_{Edd} > 0.5$    | 3.3             | 3.5             | 9.0           | 8.5         | 0            | 6.1                                 |
| 1:4 Prograde Coplanar  | $L_{bol} > L_{42}$ | 74.9            | 53.9            | 47.7          | 44.2        | 38.3         | 27.1                                |
|                        | $L_{bol} > L_{43}$ | 21.3            | 11.7            | 11.0          | 7.6         | 3.8          | 6.1                                 |
|                        | $L_{bol} > L_{44}$ | 1.8             | 2.5             | 2.9           | 1.3         | 0            | 1.4                                 |
|                        | $f_{Edd} > 0.005$  | 56.7            | 66.9            | 47.8          | 45.1        | 39.5         | 28.7                                |
|                        | $f_{Edd} > 0.05$   | 10.8            | 17.3            | 9.0           | 7.0         | 4.0          | 5.2                                 |
|                        | $f_{Edd} > 0.5$    | 0.7             | 2.9             | 1.3           | 0.67        | 0            | 0.56                                |
| 1:4 Inclined           | $L_{bol} > L_{42}$ | 75.4            | 57.3            | 44.8          | 44.6        | 36.4         | 24.2                                |
|                        | $L_{bol} > L_{43}$ | 21.5            | 13.3            | 7.6           | 7.6         | 4.5          | 3.2                                 |
|                        | $L_{bol} > L_{44}$ | 1.9             | 1.2             | 0.76          | 0.76        | 0            | 0.55                                |
|                        | $f_{Edd} > 0.005$  | 58.1            | 67.8            | 42.2          | 42.1        | 35.2         | 24.3                                |
|                        | $f_{Edd} > 0.05$   | 9.8             | 19.1            | 5.4           | 5.4         | 3.6          | 2.4                                 |
|                        | $f_{Edd} > 0.5$    | 0.78            | 1.6             | 0.24          | 0.24        | 0            | 0.24                                |
| 1:10 Prograde Coplanar | $L_{bol} > L_{42}$ | 71.8            | 24.2            | 21.8          | 20.9        | 18.9         | 10.0                                |
|                        | $L_{bol} > L_{43}$ | 16.2            | 3.2             | 1.3           | 1.3         | 1.3          | 0.53                                |
|                        | $f_{Edd} > 0.005$  | 50.0            | 49.0            | 34.0          | 32.8        | 30.8         | 16.0                                |
|                        | $f_{Edd} > 0.05$   | 6.7             | 10.4            | 3.2           | 3.2         | 3.2          | 1.5                                 |
|                        | $f_{Edd} > 0.5$    | 0.27            | 1.0             | 0             | 0           | 0            | 0                                   |

**Table B.1.** Dual AGN fractions for the remaining spiral-spiral simulations not in Table 4.2.  $BH_1$  and  $BH_2$  represent the percentage of the entire simulation that each BH is active at the given observability threshold. The dual fraction is the total time when both AGN are active divided by the total time that one or both AGN are active, also expressed as a percentage. The remaining columns give the dual fraction with additional constraints for observation.

| Simulation   | Threshold          | BH <sub>1</sub> | BH <sub>2</sub> | Dual Fraction | $d > 1$ kpc | $d > 10$ kpc | $\Delta v > 150$ km s <sup>-1</sup> |
|--------------|--------------------|-----------------|-----------------|---------------|-------------|--------------|-------------------------------------|
| 1:2 (no gas) | $L_{bol} > L_{42}$ | 30.7            | 67.0            | 31.4          | 29.3        | 16.4         | 23.3                                |
|              | $L_{bol} > L_{43}$ | 26.5            | 19.2            | 23.6          | 22.2        | 8.2          | 16.9                                |
|              | $L_{bol} > L_{44}$ | 12.1            | 1.9             | 6.3           | 5.9         | 0.60         | 3.8                                 |
|              | $f_{Edd} > 0.005$  | 21.2            | 47.9            | 23.8          | 22.1        | 9.3          | 16.0                                |
|              | $f_{Edd} > 0.05$   | 7.0             | 9.9             | 11.0          | 10.2        | 1.6          | 6.9                                 |
|              | $f_{Edd} > 0.5$    | 0.38            | 0.64            | 1.3           | 1.3         | 0.55         | 0.73                                |
| 1:2 (5% gas) | $L_{bol} > L_{42}$ | 100.0           | 77.4            | 77.4          | 76.5        | 66.8         | 54.4                                |
|              | $L_{bol} > L_{43}$ | 96.8            | 26.8            | 26.0          | 25.5        | 19.5         | 18.6                                |
|              | $L_{bol} > L_{44}$ | 52.1            | 3.5             | 4.5           | 4.2         | 2.4          | 3.0                                 |
|              | $f_{Edd} > 0.005$  | 89.1            | 62.5            | 57.4          | 56.8        | 48.4         | 40.6                                |
|              | $f_{Edd} > 0.05$   | 22.7            | 15.0            | 16.3          | 15.7        | 8.2          | 10.4                                |
|              | $f_{Edd} > 0.5$    | 3.2             | 1.3             | 2.7           | 2.5         | 2.0          | 1.3                                 |

**Table B.2.** Dual AGN fractions for the elliptical-spiral mergers.  $BH_1$  and  $BH_2$  represent the percentage of the entire simulation that each BH is active at the given observability threshold. The dual fraction is the total time when both AGN are active divided by the total time that one or both AGN are active, also expressed as a percentage. The remaining columns give the dual fraction with additional constraints for observation.

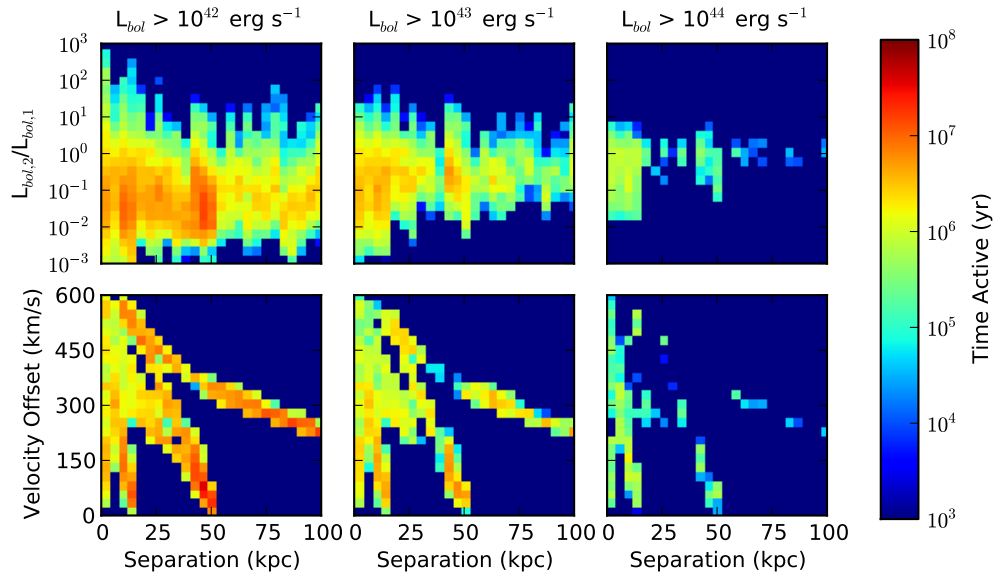


**Figure B.7.** Dual AGN observability timescales in the 1:2 elliptical-spiral merger (with gas). Top panels: luminosity ratio between the two BHs as a function of BH separation when both BHs are accreting at the given luminosity. Bottom panels: velocity offset between the BHs as a function of separation when they are observable as a dual AGN. The color of each point indicates the total dual AGN timescale.

## BIBLIOGRAPHY

- Abel, T., Bryan, G. L., & Norman, M. L. 2000, *ApJ*, 540, 39
- Alonso-Herrero, A., Rosales-Ortega, F. F., Sánchez, S. F., Kennicutt, R. C., Pereira-Santaella, M., & Díaz, Á. I. 2012, *MNRAS*, 425, L46
- Baes, M., Buyle, P., Hau, G. K. T., & Dejonghe, H. 2003, *MNRAS*, 341, L44
- Balbus, S. A. & Hawley, J. F. 1998, *Reviews of Modern Physics*, 70, 1
- Baldwin, J. A., Phillips, M. M., & Terlevich, R. 1981, *PASP*, 93, 5
- Ballo, L., Braitto, V., Della Ceca, R., Maraschi, L., Tavecchio, F., & Dadina, M. 2004, *ApJ*, 600, 634
- Barnes, J. E. & Hernquist, L. 1992, *ARA&A*, 30, 705
- Barth, A. J., Bentz, M. C., Greene, J. E., & Ho, L. C. 2008, *ApJL*, 683, L119
- Barth, A. J., Martini, P., Nelson, C. H., & Ho, L. C. 2003, *ApJL*, 594, L95
- Bate, M. R. & Burkert, A. 1997, *MNRAS*, 288, 1060
- Battaglia, G., et al. 2006, *AAP*, 459, 423
- Baumgarte, T. W. & Shapiro, S. L. 1999, *ApJ*, 526, 941
- Begelman, M. C., Blandford, R. D., & Rees, M. J. 1980, *Nature*, 287, 307
- Begelman, M. C., Rossi, E. M., & Armitage, P. J. 2008, *MNRAS*, 387, 1649
- Begelman, M. C., Volonteri, M., & Rees, M. J. 2006, *MNRAS*, 370, 289
- Bellovary, J. M., Governato, F., Quinn, T. R., Wadsley, J., Shen, S., & Volonteri, M. 2010, *ApJL*, 721, L148
- Benson, A. J. 2005, *MNRAS*, 358, 551
- Bianchi, S., Chiaberge, M., Piconcelli, E., Guainazzi, M., & Matt, G. 2008, *MNRAS*, 386, 105
- Binney, J. & Tremaine, S. 2008, *Galactic Dynamics: Second Edition* (Galactic Dynamics: Second Edition, by James Binney and Scott Tremaine. ISBN 978-0-691-13026-2 (HB). Published by Princeton University Press, Princeton, NJ USA, 2008.)

Blecha, L., Loeb, A., & Narayan, R. 2013, MNRAS, 429, 2594

Blumenthal, G. R., Faber, S. M., Primack, J. R., & Rees, M. J. 1984, Nature, 311, 517

Bondi, H. 1952, MNRAS, 112, 195

Bournaud, F., et al. 2011, ApJ, 730, 4

Bovill, M. S. & Ricotti, M. 2009, ApJ, 693, 1859

Boylan-Kolchin, M., Ma, C.-P., & Quataert, E. 2006, MNRAS, 369, 1081

Boylan-Kolchin, M., Ma, C.-P., & Quataert, E. 2008, MNRAS, 383, 93

Braine, J., Lisenfeld, U., Duc, P.-A., Brinks, E., Charmandaris, V., & Leon, S. 2004, AAP, 418, 419

Bromm, V., Coppi, P. S., & Larson, R. B. 1999, ApJL, 527, L5

Bromm, V., Ferrara, A., Coppi, P. S., & Larson, R. B. 2001, MNRAS, 328, 969

Brooks, A. M., Governato, F., Booth, C. M., Willman, B., Gardner, J. P., Wadsley, J., Stinson, G., & Quinn, T. 2007, ApJL, 655, L17

Bullock, J. S., Dekel, A., Kolatt, T. S., Kravtsov, A. V., Klypin, A. A., Porciani, C., & Primack, J. R. 2001, ApJ, 555, 240

Callegari, S., Kazantzidis, S., Mayer, L., Colpi, M., Bellovary, J. M., Quinn, T., & Wadsley, J. 2011, ApJ, 729, 85

Callegari, S., Mayer, L., Kazantzidis, S., Colpi, M., Governato, F., Quinn, T., & Wadsley, J. 2009, ApJL, 696, L89

Carr, B. J., Bond, J. R., & Arnett, W. D. 1984, ApJ, 277, 445

Chandrasekhar, S. 1943, ApJ, 97, 255

Chevalier, R. A. 1974, ApJ, 188, 501

Christensen, C., Quinn, T., Governato, F., Stilp, A., Shen, S., & Wadsley, J. 2012, MNRAS, 425, 3058

Ciotti, L., Lanzoni, B., & Volonteri, M. 2007, ApJ, 658, 65

Ciotti, L. & Ostriker, J. P. 2007, ApJ, 665, 1038

Cisternas, M., et al. 2011, ApJ, 726, 57

Colpi, M., Mayer, L., & Governato, F. 1999, ApJ, 525, 720

Comerford, J. M., et al. 2009a, ApJ, 698, 956

- Comerford, J. M., Griffith, R. L., Gerke, B. F., Cooper, M. C., Newman, J. A., Davis, M., & Stern, D. 2009b, *ApJL*, 702, L82
- Cox, T. J., Jonsson, P., Somerville, R. S., Primack, J. R., & Dekel, A. 2008, *MNRAS*, 384, 386
- Cuadra, J., Armitage, P. J., Alexander, R. D., & Begelman, M. C. 2009, *MNRAS*, 393, 1423
- Daddi, E., et al. 2010, *ApJL*, 714, L118
- De Villiers, J.-P., Hawley, J. F., & Krolik, J. H. 2003, *ApJ*, 599, 1238
- De Villiers, J.-P., Hawley, J. F., Krolik, J. H., & Hirose, S. 2005, *ApJ*, 620, 878
- Debattista, V. P., Ferreras, I., Pasquali, A., Seth, A., De Rijcke, S., & Morelli, L. 2006, *ApJL*, 651, L97
- Debuhr, J., Quataert, E., & Ma, C.-P. 2012, *MNRAS*, 420, 2221
- Debuhr, J., Quataert, E., Ma, C.-P., & Hopkins, P. 2010, *MNRAS*, 406, L55
- Devecchi, B. & Volonteri, M. 2009, *ApJ*, 694, 302
- Di Matteo, T., Springel, V., & Hernquist, L. 2005, *Nature*, 433, 604
- Dibi, S., Drappeau, S., Fragile, P. C., Markoff, S., & Dexter, J. 2012, *MNRAS*, 426, 1928
- Diemand, J., Kuhlen, M., & Madau, P. 2007, *ApJ*, 667, 859
- Dotti, M., Colpi, M., Haardt, F., & Mayer, L. 2007, *MNRAS*, 379, 956
- Dotti, M., Ruzkowski, M., Paredi, L., Colpi, M., Volonteri, M., & Haardt, F. 2009, *MNRAS*, 396, 1640
- Dotti, M., Volonteri, M., Perego, A., Colpi, M., Ruzkowski, M., & Haardt, F. 2010, *MNRAS*, 402, 682
- Dubois, Y., Devriendt, J., Slyz, A., & Teyssier, R. 2012, *MNRAS*, 420, 2662
- Dunkley, J., et al. 2009, *ApJS*, 180, 306
- Eke, V. R., Cole, S., & Frenk, C. S. 1996, *MNRAS*, 282, 263
- Ellison, S. L., Patton, D. R., Mendel, J. T., & Scudder, J. M. 2011, *MNRAS*, 418, 2043
- Erb, D. K., Steidel, C. C., Shapley, A. E., Pettini, M., Reddy, N. A., & Adelberger, K. L. 2006, *ApJ*, 647, 128

Escala, A., Larson, R. B., Coppi, P. S., & Mardones, D. 2005, *ApJ*, 630, 152  
 Evrard, A. E. 1991, *MNRAS*, 248, 8P  
 Fabbiano, G., Wang, J., Elvis, M., & Risaliti, G. 2011, *Nature*, 477, 431  
 Fabian, A. C. 1999, *MNRAS*, 308, L39  
 Farrell, S. A., Webb, N. A., Barret, D., Godet, O., & Rodrigues, J. M. 2009, *Nature*, 460, 73  
 Ferrarese, L. 2002, *ApJ*, 578, 90  
 Ferrarese, L. & Ford, H. 2005, *Space Science Reviews*, 116, 523  
 Ferrarese, L. & Merritt, D. 2000, *ApJ*, 539, L9  
 Foreman, G., Volonteri, M., & Dotti, M. 2009, *ApJ*, 693, 1554  
 Freise, A., Chelkowski, S., Hild, S., Del Pozzo, W., Perreca, A., & Vecchio, A. 2009, *Classical and Quantum Gravity*, 26, 085012  
 Fryer, C. L., Woosley, S. E., & Heger, A. 2001, *ApJ*, 550, 372  
 Fu, H., Myers, A. D., Djorgovski, S. G., & Yan, L. 2011, *ApJ*, 733, 103  
 Fu, H., Yan, L., Myers, A. D., Stockton, A., Djorgovski, S. G., Aldering, G., & Rich, J. A. 2012, *ApJ*, 745, 67  
 Gair, J. R., Mandel, I., Miller, M. C., & Volonteri, M. 2011, *General Relativity and Gravitation*, 43, 485  
 Gebhardt, K., et al. 2000, *ApJ*, 539, L13  
 Gebhardt, K., et al. 2001, *ApJ*, 122, 2469  
 Genzel, R., et al. 2010, *MNRAS*, 407, 2091  
 Gerke, B. F., et al. 2007, *ApJL*, 660, L23  
 Ghez, A. M., et al. 2008, *ApJ*, 689, 1044  
 Gillessen, S., Eisenhauer, F., Trippe, S., Alexander, T., Genzel, R., Martins, F., & Ott, T. 2009, *ApJ*, 692, 1075  
 Gnedin, N. Y. 2000, *ApJ*, 542, 535  
 Gnedin, O. Y., Lee, H. M., & Ostriker, J. P. 1999, *ApJ*, 522, 935  
 Goulding, A. D. & Alexander, D. M. 2009, *MNRAS*, 398, 1165  
 Governato, F., et al. 2010, *Nature*, 463, 203

- Governato, F., et al. 2009, MNRAS, 398, 312
- Green, P. J., Myers, A. D., Barkhouse, W. A., Mulchaey, J. S., Bennert, V. N., Cox, T. J., & Aldcroft, T. L. 2010, ApJ, 710, 1578
- Greene, J. E. & Ho, L. C. 2007, ApJ, 667, 131
- Greene, J. E., et al. 2010, ApJ, 721, 26
- Gültekin, K., et al. 2009, ApJ, 698, 198
- Gunn, J. E. & Gott, J. R. 1972, ApJ, 176, 1
- Haardt, F. & Madau, P. 1996, ApJ, 461, 20
- Haehnelt, M. G. 1994, MNRAS, 269, 199
- Häring, N. & Rix, H.-W. 2004, ApJL, 604, L89
- Harwit, M., Houck, J. R., Soifer, B. T., & Palumbo, G. G. C. 1987, ApJ, 315, 28
- Hawley, J. F. & Krolik, J. H. 2006, ApJ, 641, 103
- Hennawi, J. F., et al. 2006, AJ, 131, 1
- Hernquist, L. 1990, ApJ, 356, 359
- Hobbs, G., et al. 2010, Classical and Quantum Gravity, 27, 084013
- Hopkins, P. F., Hernquist, L., Cox, T. J., Di Matteo, T., Robertson, B., & Springel, V. 2006, ApJS, 163, 1
- Hopkins, P. F., Hernquist, L., Martini, P., Cox, T. J., Robertson, B., Di Matteo, T., & Springel, V. 2005, ApJ, 625, L71
- Hopkins, P. F. & Quataert, E. 2010, MNRAS, 407, 1529
- Hopkins, P. F., Richards, G. T., & Hernquist, L. 2007, ApJ, 654, 731
- Hoyle, F. & Fowler, W. A. 1963, MNRAS, 125, 169
- Hudson, D. S., Reiprich, T. H., Clarke, T. E., & Sarazin, C. L. 2006, AAP, 453, 433
- Ibata, R., et al. 2009, ApJL, 699, L169
- Johansson, P. H., Burkert, A., & Naab, T. 2009, ApJL, 707, L184
- Junkkarinen, V., Shields, G. A., Beaver, E. A., Burbidge, E. M., Cohen, R. D., Hamann, F., & Lyons, R. W. 2001, ApJL, 549, L155
- Kapferer, W., Sluka, C., Schindler, S., Ferrari, C., & Ziegler, B. 2009, AAP, 499, 87



- Katz, N. 1992, *ApJ*, 391, 502
- Katz, N., Weinberg, D. H., & Hernquist, L. 1996, *ApJS*, 105, 19
- Kazantzidis, S., Mayer, L., Colpi, M., Madau, P., Debattista, V. P., Wadsley, J., Stadel, J., Quinn, T., & Moore, B. 2005, *ApJL*, 623, L67
- Kennicutt, R. C. 1998, *ApJ*, 498, 541
- Khochfar, S. & Burkert, A. 2006, *AAP*, 445, 403
- King, A. R. & Pounds, K. A. 2003, *MNRAS*, 345, 657
- King, I. 1962, *ApJ*, 67, 471
- Komossa, S., Burwitz, V., Hasinger, G., Predehl, P., Kaastra, J. S., & Ikebe, Y. 2003, *ApJL*, 582, L15
- Koposov, S., et al. 2008, *ApJ*, 686, 279
- Kormendy, J. & Freeman, K. C. 2004, in *IAU Symposium*, Vol. 220, *Dark Matter in Galaxies*, ed. S. Ryder, D. Pisano, M. Walker, & K. Freeman, 377–+
- Kormendy, J. & Richstone, D. 1995, *ARAA*, 33, 581
- Koss, M., Mushotzky, R., Treister, E., Veilleux, S., Vasudevan, R., Miller, N., Sanders, D. B., Schawinski, K., & Trippe, M. 2011, *ApJL*, 735, L42+
- Koss, M., Mushotzky, R., Treister, E., Veilleux, S., Vasudevan, R., & Trippe, M. 2012, *ApJL*, 746, L22
- Koss, M., Mushotzky, R., Veilleux, S., & Winter, L. 2010, *ApJL*, 716, L125
- Koushiappas, S. M., Bullock, J. S., & Dekel, A. 2004, *MNRAS*, 354, 292
- Kronberger, T., Kapferer, W., Ferrari, C., Unterguggenberger, S., & Schindler, S. 2008, *AAP*, 481, 337
- Lacey, C. & Cole, S. 1993, *MNRAS*, 262, 627
- Levine, R., Gnedin, N. Y., & Hamilton, A. J. S. 2010, *ApJ*, 716, 1386
- Lisenfeld, U., Mundell, C. G., Schinnerer, E., Appleton, P. N., & Allsopp, J. 2008, *ApJ*, 685, 181
- Liu, X., Greene, J. E., Shen, Y., & Strauss, M. A. 2010, *ApJL*, 715, L30
- Liu, X., Shen, Y., Strauss, M. A., & Hao, L. 2011, *ApJ*, 737, 101
- Lodato, G. & Natarajan, P. 2006, *MNRAS*, 371, 1813
- Lora, V., Sánchez-Salcedo, F. J., Raga, A. C., & Esquivel, A. 2009, *ApJL*, 699, L113

- Lynden-Bell, D. 1969, *Nature*, 223, 690
- Macciò, A. V., Dutton, A. A., & van den Bosch, F. C. 2008, *MNRAS*, 391, 1940
- Macciò, A. V., Dutton, A. A., van den Bosch, F. C., Moore, B., Potter, D., & Stadel, J. 2007, *MNRAS*, 378, 55
- Macciò, A. V., Kang, X., Fontanot, F., Somerville, R. S., Kopecký, S., & Monaco, P. 2010, *MNRAS*, 402, 1995
- Madau, P., Diemand, J., & Kuhlen, M. 2008, *ApJ*, 679, 1260
- Madau, P. & Rees, M. J. 2001, *ApJL*, 551, L27
- Magorrian, J., et al. 1998, *AJ*, 115, 2285
- Maiorana, U., Dotti, M., Petkova, M., Perego, A., & Volonteri, M. 2012, *ArXiv e-prints*
- Majewski, S. R., Frinchaboy, P. M., Kunkel, W. E., Link, R., Muñoz, R. R., Ostriker, J. C., Palma, C., Patterson, R. J., & Geisler, D. 2005, *ApJ*, 130, 2677
- Malbon, R. K., Baugh, C. M., Frenk, C. S., & Lacey, C. G. 2007, *MNRAS*, 382, 1394
- Marconi, A. & Hunt, L. K. 2003, *ApJL*, 589, L21
- Marconi, A., Risaliti, G., Gilli, R., Hunt, L. K., Maiolino, R., & Salvati, M. 2004, *MNRAS*, 351, 169
- Martin, C. L. & Kennicutt, R. C. 2001, *ApJ*, 555, 301
- Mateo, M. 1998, *Annu. Rev. Astron. Astrophys.*, 36, 435
- Mayer, L., Kazantzidis, S., Madau, P., Colpi, M., Quinn, T., & Wadsley, J. 2007, *Science*, 316, 1874
- McConnell, N. J. & Ma, C.-P. 2013, *ApJ*, 764, 184
- McConnell, N. J., Ma, C.-P., Gebhardt, K., Wright, S. A., Murphy, J. D., Lauer, T. R., Graham, J. R., & Richstone, D. O. 2011, *Nature*, 480, 215
- McGurk, R. C., Max, C. E., Rosario, D. J., Shields, G. A., Smith, K. L., & Wright, S. A. 2011, *ApJL*, 738, L2+
- McKee, C. F. & Ostriker, J. P. 1977, *ApJ*, 218, 148
- Merloni, A., Rudnick, G., & Di Matteo, T. 2004, *MNRAS*, 354, L37
- Merritt, D. & Cruz, F. 2001, *ApJL*, 551, L41
- Merritt, D., Ferrarese, L., & Joseph, C. L. 2001, *Science*, 293, 1116
- Mihos, J. C. & Hernquist, L. 1996, *ApJ*, 464, 641

- Milosavljević, M. & Merritt, D. 2001, *ApJ*, 563, 34
- Mo, H., van den Bosch, F. C., & White, S. 2010, *Galaxy Formation and Evolution*
- Mo, H. J., Mao, S., & White, S. D. M. 1998, *MNRAS*, 295, 319
- Monaghan, J. J. 1992, *ARAA*, 30, 543
- Moran, J. M., Greenhill, L. J., & Herrnstein, J. R. 1999, *Journal of Astrophysics and Astronomy*, 20, 165
- Muñoz, J. A., Madau, P., Loeb, A., & Diemand, J. 2009, *MNRAS*, 400, 1593
- Nakai, N., Inoue, M., & Miyoshi, M. 1993, *Nature*, 361, 45
- Navarro, J. F., Frenk, C. S., & White, S. D. M. 1996, *ApJ*, 462, 563
- Navarro, J. F., Frenk, C. S., & White, S. D. M. 1997, *ApJ*, 490, 493
- Okamoto, T., Gao, L., & Theuns, T. 2008, *MNRAS*, 390, 920
- Ostriker, J. P., Spitzer, L., & Chevalier, R. A. 1972, *ApJL*, 176, L51
- Peñarrubia, J., McConnachie, A. W., & Navarro, J. F. 2008, *ApJ*, 672, 904
- Peterson, B. M., et al. 2005, *ApJ*, 632, 799
- Peterson, B. M., et al. 2004, *ApJ*, 613, 682
- Piconcelli, E., Vignali, C., Bianchi, S., Mathur, S., Fiore, F., Guainazzi, M., Lanzuisi, G., Maiolino, R., & Nicastro, F. 2010, *ApJL*, 722, L147
- Pizzella, A., Corsini, E. M., Dalla Bontà, E., Sarzi, M., Coccato, L., & Bertola, F. 2005, *ApJ*, 631, 785
- Power, C., Nayakshin, S., & King, A. 2011, *MNRAS*, 412, 269
- Read, J. I., Wilkinson, M. I., Evans, N. W., Gilmore, G., & Kley, J. T. 2006, *MNRAS*, 367, 387
- Reed, D., Governato, F., Quinn, T., Gardner, J., Stadel, J., & Lake, G. 2005, *MNRAS*, 359, 1537
- Rees, M. J. 1984, *ARAA*, 22, 471
- Rice, W. K. M., Lodato, G., & Armitage, P. J. 2005, *MNRAS*, 364, L56
- Richstone, D., et al. 1998, *Nature*, 395, A14+
- Robertson, B., Hernquist, L., Cox, T. J., Di Matteo, T., Hopkins, P. F., Martini, P., & Springel, V. 2006, *ApJ*, 641, 90

- Rodriguez, C., Taylor, G. B., Zavala, R. T., Peck, A. B., Pollack, L. K., & Romani, R. W. 2006, *ApJ*, 646, 49
- Salpeter, E. E. 1964, *ApJ*, 140, 796
- Sanders, D. B., Soifer, B. T., Elias, J. H., Madore, B. F., Matthews, K., Neugebauer, G., & Scoville, N. Z. 1988, *ApJ*, 325, 74
- Sargent, W. L. W., Young, P. J., Lynds, C. R., Boksenberg, A., Shortridge, K., & Hartwick, F. D. A. 1978, *ApJ*, 221, 731
- Schawinski, K., et al. 2010, *ApJ*, 711, 284
- Shakura, N. I. & Sunyaev, R. A. 1973, *AAP*, 24, 337
- Shankar, F., Salucci, P., Granato, G. L., De Zotti, G., & Danese, L. 2004, *MNRAS*, 354, 1020
- Shen, S., Mo, H. J., White, S. D. M., Blanton, M. R., Kauffmann, G., Voges, W., Brinkmann, J., & Csabai, I. 2003, *MNRAS*, 343, 978
- Shen, Y., Liu, X., Greene, J. E., & Strauss, M. A. 2011, *ApJ*, 735, 48
- Sheth, R. K. & Tormen, G. 1999, *MNRAS*, 308, 119
- Shiokawa, H., Dolence, J. C., Gammie, C. F., & Noble, S. C. 2012, *ApJ*, 744, 187
- Shlosman, I., Begelman, M. C., & Frank, J. 1990, *Nature*, 345, 679
- Silk, J. & Rees, M. J. 1998, *A&A*, 331, L1
- Simon, J. D. & Geha, M. 2007, *ApJ*, 670, 313
- Smith, K. L., Shields, G. A., Bonning, E. W., McMullen, C. C., Rosario, D. J., & Salviander, S. 2010, *ApJ*, 716, 866
- Soltan, A. 1982, *MNRAS*, 200, 115
- Spitzer, L. 1987, *Dynamical evolution of globular clusters*, ed. L. Spitzer
- Springel, V., Di Matteo, T., & Hernquist, L. 2005, *MNRAS*, 361, 776
- Springel, V., Wang, J., Vogelsberger, M., Ludlow, A., Jenkins, A., Helmi, A., Navarro, J. F., Frenk, C. S., & White, S. D. M. 2008, *MNRAS*, 391, 1685
- Stadel, J. G. 2001, PhD thesis, AA(UNIVERSITY OF WASHINGTON)
- Stinson, G., Seth, A., Katz, N., Wadsley, J., Governato, F., & Quinn, T. 2006, *MNRAS*, 373, 1074
- Strohmayer, T. E. & Mushotzky, R. F. 2003, *ApJ*, 586, L61

Tacconi, L. J., et al. 2010, *Nature*, 463, 781

Taffoni, G., Mayer, L., Colpi, M., & Governato, F. 2003, *MNRAS*, 341, 434

Taylor, J. E. & Babul, A. 2001, *ApJ*, 559, 716

Tegmark, M., Silk, J., Rees, M. J., Blanchard, A., Abel, T., & Palla, F. 1997, *ApJ*, 474, 1

Tollerud, E. J., Bullock, J. S., Strigari, L. E., & Willman, B. 2008, *ApJ*, 688, 277

Toomre, A. 1977, in *Evolution of Galaxies and Stellar Populations*, ed. B. M. Tinsley & R. B. G. Larson, D. Campbell, 401

Toomre, A. & Toomre, J. 1972, *ApJ*, 178, 623

Tremaine, S., et al. 2002, *ApJ*, 574, 740

Valluri, M., Ferrarese, L., Merritt, D., & Joseph, C. L. 2005, *ApJ*, 628, 137

van den Bosch, F. C., Abel, T., Croft, R. A. C., Hernquist, L., & White, S. D. M. 2002, *ApJ*, 576, 21

van den Bosch, R. C. E., Gebhardt, K., Gültekin, K., van de Ven, G., van der Wel, A., & Walsh, J. L. 2012, *Nature*, 491, 729

Van Wassenhove, S., Volonteri, M., Mayer, L., Dotti, M., Bellovary, J., & Callegari, S. 2012, *ApJL*, 748, L7

van Wassenhove, S., Volonteri, M., Walker, M. G., & Gair, J. R. 2010, *MNRAS*, 408, 1139

Vollmer, B., Braine, J., & Soida, M. 2012, *AA*, 547, A39

Vollmer, B., Cayatte, V., Balkowski, C., & Duschl, W. J. 2001, *ApJ*, 561, 708

Volonteri, M., Haardt, F., & Gültekin, K. 2008a, *MNRAS*, 384, 1387

Volonteri, M., Haardt, F., & Madau, P. 2003, *ApJ*, 582, 559

Volonteri, M., Lodato, G., & Natarajan, P. 2008b, *MNRAS*, 383, 1079

Volonteri, M., Miller, J. M., & Dotti, M. 2009, *ApJL*, 703, L86

Volonteri, M. & Natarajan, P. 2009, *MNRAS*, 400, 1911

Volonteri, M. & Rees, M. J. 2006, *ApJ*, 650, 669

Wadsley, J. W., Stadel, J., & Quinn, T. 2004, *New Astronomy*, 9, 137

Walker, M. G., Mateo, M., & Olszewski, E. W. 2009a, *ApJ*, 137, 3100

- Walker, M. G., Mateo, M., Olszewski, E. W., Peñarrubia, J., Wyn Evans, N., & Gilmore, G. 2009b, *ApJ*, 704, 1274
- Walsh, S. M., Willman, B., & Jerjen, H. 2009, *ApJ*, 137, 450
- White, S. D. M. & Rees, M. J. 1978, *MNRAS*, 183, 341
- Willott, C. J., Delfosse, X., Forveille, T., Delorme, P., & Gwyn, S. D. J. 2005, *ApJ*, 633, 630
- Willott, C. J., McLure, R. J., & Jarvis, M. J. 2003, *ApJL*, 587, L15
- Woods, D. F. & Geller, M. J. 2007, *AJ*, 134, 527
- Wyithe, J. S. B. & Loeb, A. 2003, *ApJ*, 595, 614
- Yoshida, N., Omukai, K., Hernquist, L., & Abel, T. 2006, *ApJ*, 652, 6
- Younger, J. D., Hopkins, P. F., Cox, T. J., & Hernquist, L. 2008, *ApJ*, 686, 815
- Yu, Q. 2002, *MNRAS*, 331, 935
- Yu, Q., Lu, Y., Mohayaee, R., & Colin, J. 2011, *ApJ*, 738, 92
- Yu, Q. & Tremaine, S. 2002, *MNRAS*, 335, 965
- Zhang, Q., Fall, S. M., & Whitmore, B. C. 2001, *ApJ*, 561, 727